

Southern Methodist University

SMU Scholar

Earth Sciences Theses and Dissertations

Earth Sciences

Spring 2023

Quantifying Oil and Gas Industry Related Geohazard Using Radar Interferometry and Hydro-geomechanical Modeling

Weiyu Zheng

Southern Methodist University, weiyuz@smu.edu

Follow this and additional works at: https://scholar.smu.edu/hum_sci_earthsciences_etds



Part of the [Geophysics and Seismology Commons](#), and the [Hydrology Commons](#)

Recommended Citation

Zheng, Weiyu, "Quantifying Oil and Gas Industry Related Geohazard Using Radar Interferometry and Hydro-geomechanical Modeling" (2023). *Earth Sciences Theses and Dissertations*. 30.

https://scholar.smu.edu/hum_sci_earthsciences_etds/30

This Dissertation is brought to you for free and open access by the Earth Sciences at SMU Scholar. It has been accepted for inclusion in Earth Sciences Theses and Dissertations by an authorized administrator of SMU Scholar. For more information, please visit <http://digitalrepository.smu.edu>.

QUANTIFYING OIL AND GAS INDUSTRY RELATED GEOHAZARDS
USING RADAR INTERFEROMETRY AND HYDRO-GEOMECHANICAL MODELING

Approved by:

Prof. Zhong Lu
Professor of Geophysics

Prof. Robert Gregory
Professor of Geology

Prof. Matt Hornbach
Professor of Geophysics

Dr. Jinwoo Kim
Research Scientist of Geophysics

Dr. Roger Denlinger
Research Geophysicist (USGS)

Dr. Zhen Liu
Scientist (JPL)

QUANTIFYING OIL AND GAS INDUSTRY RELATED GEOHAZARDS
USING RADAR INTERFEROMETRY AND HYDRO-GEOMECHANICAL MODELING

A Dissertation Presented to the Graduate Faculty of the

Dedman College

Southern Methodist University

in

Partial Fulfillment of the Requirements

for the degree of

Doctor of Philosophy

with a

Major in Geophysics

by

Weiyu Zheng

B.S., Geophysics, University of Science and Technology of China

May 13, 2023

Copyright (2023)

Weiyu Zheng

All Rights Reserved

ACKNOWLEDGMENTS

This work could not have been accomplished without the wisdom and generous support of my wonderful advisor, Prof. Zhong Lu. I am grateful for his guidance, encouragement, patience, academic training and help throughout my pursuit of the PhD degree. Beyond the research, he provides sincere concerns about our mental and physical conditions, especially during the pandemic. Thanks to Dr. Jinwoo Kim for his tremendous support and help with InSAR processing. I want to thank Dr. Roger Denlinger, for his supervision of the theory of poroelasticity, patient and scrupulous edits of my manuscripts, and the insightful discussions and comments. I also want to express my gratitude to other members of my dissertation committee, Dr. Robert Gregory, for the valuable feedback and constructive criticisms; Dr. Matt Hornbach, for his enlightening guidance of hydrogeology; Dr. Zhen Liu, for the helpful discussions and kind words. I also want to thank Dr. Syed Tabrez Ali for his training and help on Defmod.

Thanks to all the faculty and staff at SMU, especially Stephanie Schwob, for the help with all the tedious paperwork and relaxing chats outside of research; Dr. Heather Deshon, for providing a friendly environment within the department. I also benefited a lot from the discussions with all past and current SMU Radar Lab members. I am also grateful for the wonderful friendship from all my friends at the Earth Science department at SMU.

Thanks to my parents for their consistent and selfless love, support, and encouragement during my whole life, especially during my PhD journey. Special thanks to my fiancé Siyuan Sui, for his mood and food :)

This study was funded by NASA Earth Surface and Interior Program (NNX16AL10G and 80NSSC21K1474), NASA-ISRO SAR (NISAR) Science Team (80NSSC19K1491), and SMU Moody Dissertation Fellowship.

Quantifying Oil and Gas Industry Related Geohazard
Using Radar Interferometry and Hydro-geomechanical Modeling

Advisor: Professor Zhong Lu
Doctor of Philosophy conferred May 13, 2023
Dissertation completed May 5, 2023

The Permian Basin, containing a large amount of oil and gas, has been intensively developed for hydrocarbon production. However, the hazards related to the oil and gas industry including surface deformation and the underlying mechanisms in this region have not been well known. My PhD study aims to monitor the geohazards in the Permian Basin and better comprehend the subsurface mechanisms with the aid of high-resolution and high-accuracy Interferometric Synthetic Aperture Radar (InSAR) images. Generally, as the pore pressure is influenced by wastewater injection/hydrocarbon production, the pressure changes can propagate to other surrounding underground and overlying rock/soil layers, resulting in surface deformation. The distribution and temporal development of the surface deformation can be obtained from InSAR processing and analysis. To reveal the underground geo-mechanical process responsible for the development of the surface deformation, numerical modeling based on poroelasticity is then applied to estimate the effective parameters (i.e., parameters inferred from the simulation) including depth and volume. This method is applied to three cases in West Texas. At a site in Reeves county, InSAR detects surface uplift up to 17 cm near a wastewater disposal well from 2007 to 2011. Results from both elastic and poroelastic models indicate that the effective injection depth is much shallower than reported. The most reasonable explanation is that the well was experiencing leakage due to casing failures and/or sealing problem(s). At a site

in Winkler county, surface uplift and the follow-on recovery detected by InSAR from 2015 to 2020 can be attributed to nearby wastewater disposal. Bayesian inversion with the poroelastic models provides estimates of the local hydro-geomechanical parameters. The posterior distribution of subsurface effective volumes reveals under-reported volumes in the well near the deformation center. We also investigate a case of aseismic slip related to oil and gas activities. The combination of InSAR observation and poroelastic finite element models in three cases shows the capability to investigate the ongoing geohazards related to fluid injection and hydrocarbon production in the Permian Basin. This kind of study will be helpful to the decision-making of federal/local authorities to avoid future geohazards related to oil and gas activities.

TABLE OF CONTENTS

LIST OF FIGURES	xi
LIST OF TABLES	xiv
CHAPTER 1 Introduction.....	1
1.1 Problem definition	1
1.2 Thesis roadmap	2
CHAPTER 2 InSAR background	5
2.1 SAR imaging.....	5
2.2 InSAR	9
2.3 InSAR time-series processing.....	12
2.4 InSAR applications in geohazards related to oil and gas industry.....	14
Reference	17
CHAPTER 3 Modeling work.....	19
3.1 Poroelasticity.....	19
3.2 Method of solution.....	20
3.3 Inverse method for geohazards related to oil and gas industry.....	23
Reference	27
CHAPTER 4 Permian Basin background	28
4.1 Permian Basin geology	28

4.2 Hydrocarbon production	30
4.3 Human impacts	34
Reference	37
CHAPTER 5 Effective depth detection: a case study of wastewater leakage	40
5.1 Introduction.....	40
5.2 Method.....	46
5.3 Results.....	49
5.4 Discussion.....	56
5.5 Conclusion	66
Reference	67
CHAPTER 6 Effective volume detection: a case study of under-reported volume	70
6.1 Introduction.....	70
6.2 Method.....	73
6.3 Results.....	81
6.4 Discussion.....	90
6.5 Conclusion	99
Reference	100
CHAPTER 7 A case study of aseismic slip induced by fluid injection.....	103
7.1 Introduction.....	103
7.2 Method.....	104

7.3 Results.....	108
Reference	115
CHAPTER 8 Conclusion	117

LIST OF FIGURES

Figure 2.1	Illustration of the imaging geometry of a space-borne SAR system.....	6
Figure 2.2	Summary of Azimuth and range compression	9
Figure 2.3	Illustration of the imaging geometry of an InSAR system. (modified from Lu and Dzurisin, 2014)	11
Figure 2.4	Timeline of past, present and future SAR missions between 1991 and 2025, and their main features. (Macchiarulo et al., 2022)	15
Figure 4.1	Major structural and tectonic features in the region of the Permian Basin. Image Source: U.S. Energy Information Administration based on DrillingInfo Inc., U.S. Geological Survey.	29
Figure 4.2	East–west cross section along the southern margin of the Permian Basin. (Scanlon et al., 2017)	30
Figure 4.3	Permian Basin production wells (from Texas RRC).....	31
Figure 4.4	Simplified diagrams of oil-field operations.....	33
Figure 4.5	Illustration of InSAR detection of ground deformation induced by Wastewater injection and enhanced recovery wells.	35
Figure 4.6	The whole process of fault slip induced by fluid injection in industrial production (He et al., 2020).	36
Figure 5.1	Study area of the case in Reeves county.	42

Figure 5.2 Time series cumulative vertical deformation maps from 2007/01/18 to 2011/03/16 over the study area.	50
Figure 5.3 Comparison of the cumulative wastewater injection volume (gray bars) and time-series cumulative vertical deformation at the deformation center (black line).	52
Figure 5.4 Mogi model of cumulative vertical deformation from 2007/01/18 to 2011/03/16. ...	53
Figure 5.5 Final displacement fields and surface profiles of the forward poroelastic models. ...	55
Figure 5.6 Three-layer poroelastic model with a confined aquifer.....	58
Figure 5.7 Stratigraphy, well completion, and possible pathways for upward migration of wastewater.	59
Figure 5.8 Three-layer poroelastic model with a fracture.....	63
Figure 5.9 Comparison of the cumulative wastewater injection volume (gray bars) and the dissolved sodium in the Pecos Valley Aquifer (black line).....	65
Figure 6.1 Background information in the research area.....	74
Figure 6.2 Mesh of the Three-layer finite element model.	79
Figure 6.3 Convergence of Monte Carlo.	80
Figure 6.4 Results from the Bayesian Monte Carlo approach.	82
Figure 6.5 Observation, simulation and residuals.....	84
Figure 6.6 Marginal posterior probability distributions.....	89
Figure 6.7 Best-fit results based on fixed reported volume.	93
Figure 6.8 Production.....	95

Figure 6.9 Comparison of the methods using constraints as the whole spatio-temporal constraints, one cumulative spatial deformation map (spatial constraints), and temporal evolution of the deformation center (temporal constraints).	96
Figure 6.10 Marginal distributions	97
Figure 7.1 Research Area. The base map is the LOS deformation from 2020/01/01 to 2020/01/25.	105
Figure 7.2 Hydrocarbon industry wells and the injection formation contour.....	107
Figure 7.3 Monthly injection volumes of well #21935700.....	107
Figure 7.4 Cumulative ground deformation before and after the aseismic slip.....	109
Figure 7.5 Bayesian inversion of the aseismic slip for descending track. Top: InSAR observation, simulation and the residual. Bottom: Posterior distribution of the strike and dip angle.....	110
Figure 7.6 Bayesian inversion of the aseismic slip for ascending track. Top: InSAR observation, simulation and the residual. Bottom: Posterior distribution of the strike and dip angle.....	111
Figure 7.7 Simulation of deformation before the aseismic slip and the corresponding pore pressure distribution on the inferred fault plane.	113
Figure 7.8 Conceptual illustrations of the possible mechanism (pore pressure increases and solid matrix stress changes).....	114

LIST OF TABLES

Table 5.1 Stratigraphy of the study area.	43
Table 6.1 Geologic stratigraphy.....	75
Table 6.2 7 wastewater disposal wells.	76
Table 6.3 Parameters used in the poroelastic model.....	81
Table 7.1 Geologic Stratigraphy.....	106
Table 7.2 Inferred fault parameters.....	111

To my family

CHAPTER 1

Introduction

1.1 Problem definition

The Permian Basin, containing a large amount of oil and gas, has been intensively developed for hydrocarbon production. However, the hazards related to the oil and gas industry (e.g., surface deformation, induced seismicity, and sinkhole formation) and the underlying mechanisms in this region have not been well known. Those hazards have caused ground instability and threatened humanity, infrastructures, and oil facilities, resulting in financial loss and potential life loss. Besides, subsurface hazards including unexpected wastewater leakage and fluid migration can pose health risks and contamination in the environment. To minimize potential geohazards associated with oil and gas activities, we need to identify and quantify existing geohazards, understand the mechanisms behind the geohazards, and learn more detailed subsurface properties (such as geologic stratigraphy, mechanical parameters, and hydrogeologic components).

To monitor the geohazards over the Delaware Basin and better comprehend the subsurface mechanisms, the high-resolution and high-accuracy Interferometric Synthetic Aperture Radar (InSAR) imagery has proved the capacity in measuring ground deformation. The distribution and temporal development of the surface deformation can be obtained from InSAR observation. The spatio-temporal correlation between the surface deformation and the oil and gas

records (or other possible causes like groundwater withdrawal) can be investigated to explore the causes of the geohazards.

The finite element method has been utilized widely in practice because it allows material heterogeneity, irregular boundaries, distributed mechanical loads and fluid sources. It can be utilized to construct numerical models with fewer or weak assumptions and is believed to be closer to reality compared to analytical methods. Deformation observed by Interferometric Synthetic Aperture Radar (InSAR) and the injection/production information will be jointly inverted to solve for precise mechanical and hydrogeologic parameters using a Bayesian approach. The Markov Chain Monte Carlo (MCMC) method can be employed as the optimization method. The inversion results can provide bounds on the injection/production information and the local stratigraphy, and thus will be used to refine the poroelastic models. The refined poroelastic models along with the best solution of the mechanical and hydrogeologic parameters can then be used to predict the future evolution of the geohazards and provide a scientific basis for the decision-making of fluid injection and hydrocarbon production. This type of analysis can be widely applicable to almost all the ongoing geohazards related to fluid injection and hydrocarbon production detected by InSAR.

1.2 Thesis roadmap

In Chapter 2, we review the principles of Interferometric Synthetic Aperture Radar (InSAR).

In Chapter 3, we give a brief introduction to the related modeling work including poroelasticity, finite element method, and Bayesian inversion.

In Chapter 4, we introduce the research area Permian Basin. We start from the geology and the formation of the basin, then introduce the current state of the hydrocarbon production, and also discuss how human activities impact the Earth.

In Chapter 5, we present a case study with shallow effective depth. At a site in the Ken Regan field, West Texas, we detected surface uplift near a wastewater disposal well from 2007 to 2011. A high correlation between the observed deformation and the injection volume suggests that the uplift was caused by wastewater disposal in the well. Inverse elastic models were first used to calculate the injection depth and volume. Given the initial estimates of wastewater injection, forward poroelastic finite element models were applied to simulate stress/strain and displacement fields and to estimate the effective injection volume and depth, so as to ultimately understand the subsurface geomechanical processes and provide insight into the local hydrologic properties of the strata in the well location. Results from both elastic and poroelastic models indicate that the effective injection depth suggested by the simulation is much shallower than reported. The most reasonable explanation is that the well was experiencing leakage due to casing failures and/or sealing problem(s). The Rustler Aquifer, within the zone of the effective injection depth, has been used for irrigation and livestock; wastewater leaked into this aquifer may possibly contaminate the freshwater sources. Our analysis that exploits remote sensing data and numerical models provides a clue to understanding the subsurface hydrogeological process responding to the oil and gas activities and an indirect leakage monitoring method to supplement current infrequent leakage detection.

In Chapter 6, we present a case study with excess effective volume. At a site in Winkler County, we detected surface uplift and the follow-on recovery due to wastewater injection. We have inverted spatio-temporal deformation measured by InSAR and injection information using a

Bayesian Monte Carlo approach with a poroelastic finite element model. The distribution of local hydro-geomechanical parameters, especially Young's modulus and hydraulic conductivity, play an essential role in these geohazards. Sentinel-1A/B imagery from 2014 to 2020 is processed to track the spatio-temporal deformation in Winkler county, west Texas, USA. The posterior distribution of subsurface effective volumes reveals under-reported volumes in the well near the deformation center. In addition, the inversion results provide better constraints for the parameters than those solely obtained based on the cumulative spatial deformation or temporal development of the deformation center.

In Chapter 7, We introduce a case study of aseismic slip induced by wastewater injection. We use SAR images from August 2018 to January 2020 acquired from ascending track P78 and descending track P85 of Sentinel 1A/B to measure the surface deformation. Ground uplifts are detected from August 2018 to January 2020, then the deformation patterns change to paired lobes of uplift and subsidence from January 2020 to March 2020. The time series processing is implemented by Multidimensional Small Baseline Subset (MSBAS) to retrieve two-dimensional deformation. We use the Okada dislocation model to simulate the aseismic slip detected by InSAR. To solve for the fault parameters, we use Bayesian inversion via Geodetic Bayesian Inversion Software (GBIS). With the monthly injection volume of the dominant well and the local stratigraphy, we apply poroelastic finite element models to simulate the ground uplift before the aseismic slip and calculate the pore pressure distribution on the fault plane via Defmod.

We finally conclude in Chapter 8.

CHAPTER 2

InSAR background

2.1 SAR imaging

Synthetic Aperture Radar (SAR) is a signal processing technique that produces images of the Earth surface using radar from a moving space-borne or air-borne platform. The radar system transmits electromagnetic waves and receives the backscattered echoes in a sequential way. As the transmitted electromagnetic waves interact with the Earth surface, the backscattered echoes can reflect properties (including geometry, roughness, permittivity, etc.) of the imaged object. Compared to optical data, SAR can provide two-dimensional images with high resolution from day to night, avoiding influence from cloud coverage and weather conditions (Curlander and McDonough, 1991). SAR has been widely applied in remote sensing in recent years for its capability of continuously monitoring dynamic processes on the Earth surface on a global scale. Based on SAR, many useful techniques including polarimetric SAR and interferometric SAR have been established.

2.1.1 Geometry

Fig. 3.1 illustrates the typical imaging geometry of a space-borne SAR system. When the satellite moves in the azimuth direction (along-track direction), the radar on the platform points a radar beam toward the Earth roughly perpendicular to the flight direction, which illuminates a swath on the ground. This direction, parallel to the radar beam and perpendicular to the flight direction, is defined as range direction. The transmitted radar waves are phase encoded and

interact with ground targets in the illuminated swath, the backscattered echoes are recorded by the receiving antenna at a later time. The time delay between the transmitted and received signals is recorded by phase, which is modulated by 2π . It is proportional to the back-and-forth distance from the satellite to the scatterers. The intensity of the received radar waves depends on the imaging geometry including satellite height and incidence angle (the angle between the radar beam and the normal of the ground surface, which is slightly different from the look angle) and the radar reflectivity of scatterers on the ground including roughness and permittivity.

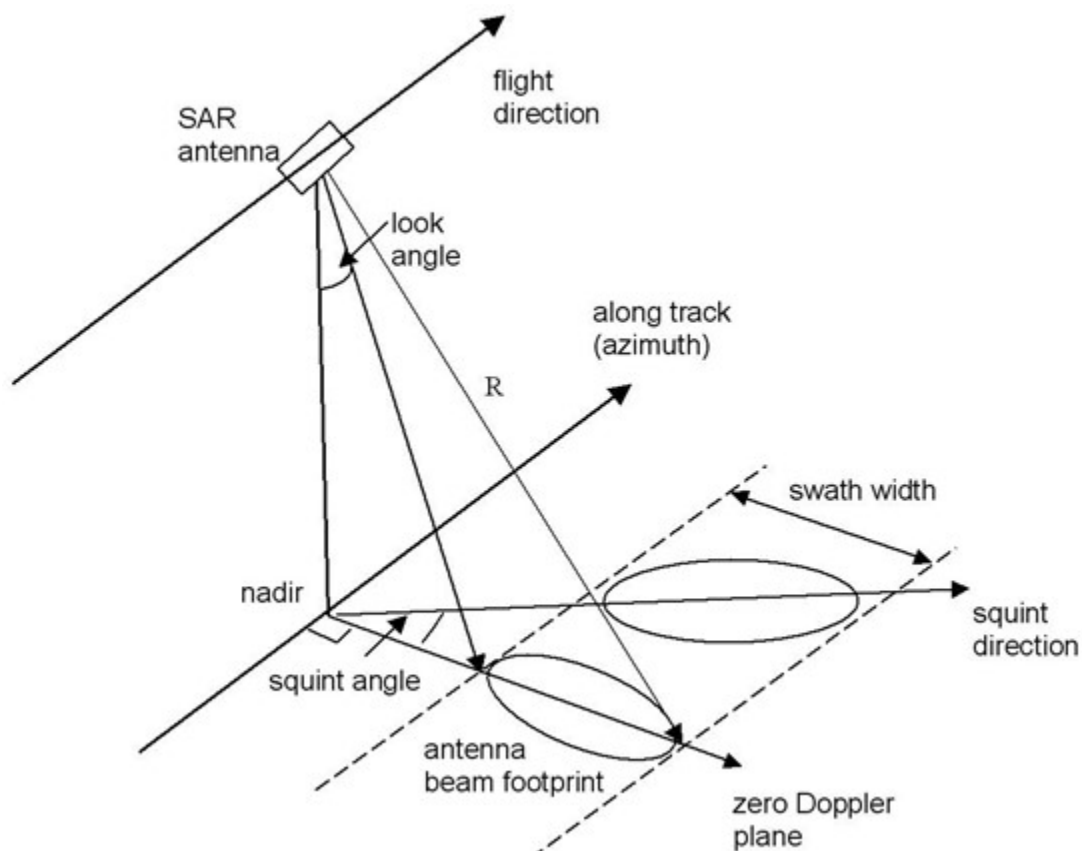


Figure 2.1 Illustration of the imaging geometry of a space-borne SAR system. (Image source: European Space Agency (ESA))

2.1.2 Range and Azimuth Compression

SAR systems commonly transmit pulsed waveforms called *chirp* signals. During the pulse time τ , the frequency f is changing over time as

$$f(t) = k_r \cdot t, -\frac{\tau}{2} < t < \frac{\tau}{2} \quad (2.1)$$

where k_r is the chirp rate. The chirp bandwidth can be written as

$$B_r = k_r \cdot \tau \quad (2.2)$$

The range resolution is then given by

$$\delta_r = \frac{c}{2B_r} \quad (2.3)$$

where c is the speed of light.

The illumination time of a ground scatterer is approximated as

$$\tau_i \approx \frac{\lambda r_0}{vl} \quad (2.4)$$

where λ is the wavelength of the radar sensor, r_0 is the distance from the radar sensor to the ground scatterer, v is the moving speed of the satellite, l is the length of the antenna. The bandwidth in the azimuth direction can be written as

$$B_a = \frac{2v}{l} \quad (2.5)$$

The range resolution is then given by

$$\delta_a = \frac{l}{2} \quad (2.6)$$

The received signals are recorded with complex numbers: the real and imaginary components can be used to represent the phase and amplitude values. The raw SAR data does not contain direct ground features, the signals should be processed to retrieve useful information (Fig. 3.2). The first step is to compress the transmitted chirp into a short pulse signal in the range

direction. Range compression is implemented in the frequency domain using Fast Fourier Transformation (FFT) (Hassen, 2001). Each range line is multiplied by the complex conjugate of the spectrum of the transmitted chirp in the frequency domain. After the deconvolution of the chirp, the relative distance between the radar and any point on the ground can be recovered. The satellite moves along the azimuth direction, therefore, each point on the ground can interact with multiple pulses. The echoes from multiple illuminations create the second chirp function in the azimuth direction. The received signals have the same waveform but are shifted in frequency due to the relative movement between the radar and the scatterer, which is in analogy with the well-known “Doppler effect” in physics. Azimuth compression follows a similar principle as range compression by multiplication with the complex conjugate of the response from a scatterer on the ground. The range reference function is dependent only on the transmitted chirp waveform, while the azimuth reference function depends on the geometry and is adapted to the range (Moreira et al., 2013).

To make sure that each image pixel in the SAR image represents the reflectivity of the corresponding point on the ground, two more steps after the completion of the range and azimuth compressions should be applied: image calibration and geocoding. The calibration ensures that the intensity value actually represents the sigma zero value of the reflectivity, i.e., the radar cross section normalized to area. The geocoding ensures that the location of any pixel in the SAR image is directly associated with the position on the ground. As radar only measures in the radar coordinates (range and azimuth directions), SAR images are geometrically distorted. Therefore, geocoding is required to reproject the SAR image in a map coordinate.

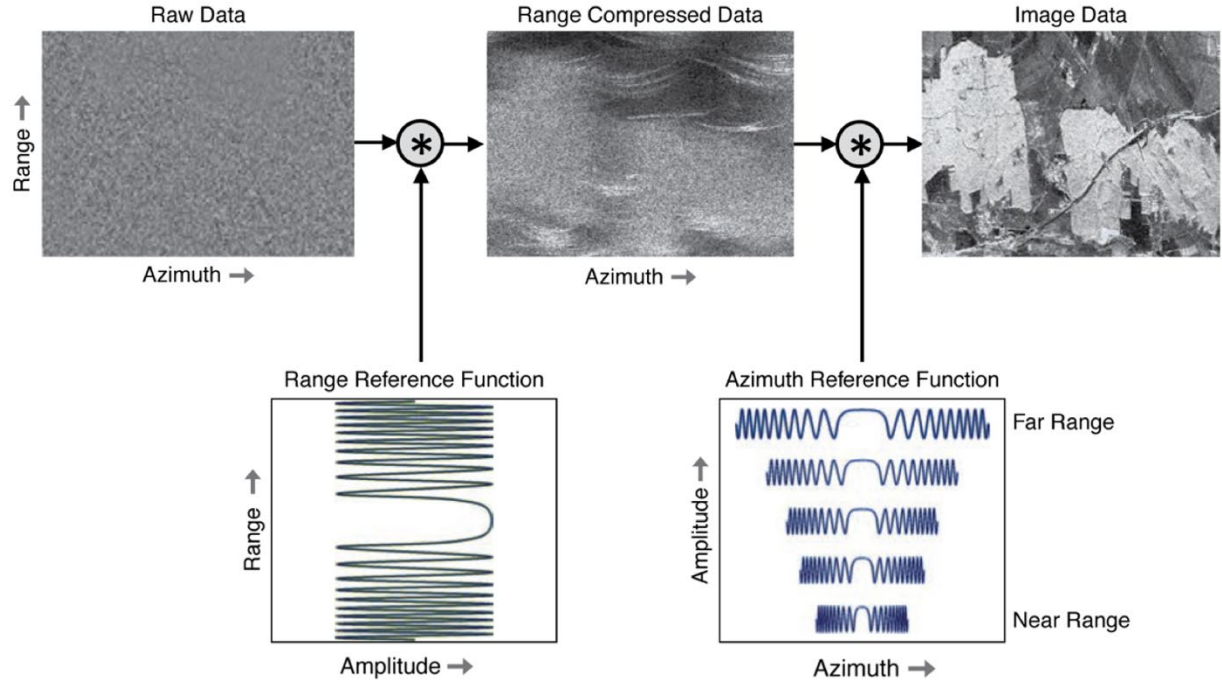


Figure 2.2 Summary of Azimuth and range compression

2.2 InSAR

Interferometric SAR is a powerful and developed remote sensing technique that enables the highly accurate measurement of surface topography or ground deformation over regional areas with meter-level resolution by comparing the phases of two or more complex SAR images for a given scene that have been acquired from slightly different positions or at different times (Bamler and Hartl, 1998).

The phase of a pixel on a SAR image can be represented as

$$\phi = -\frac{4\pi}{\lambda}r + \varepsilon \quad (2.7)$$

where λ is the wavelength of the radar, r is the range distance from the satellite to the ground target, ε is the sum of phase shifts due to the interaction between the incident radar wave and scatterers within a given resolution cell.

Before producing an interferogram, image co-registration is required to geometrically align two or more SAR images. Suppose the interactions between transmitted radar waves and surface scatterers are the same, i.e., ε in the SAR images are the same, the interferometric phase value is

$$\phi = -\frac{4\pi(r_1 - r_2)}{\lambda} \quad (2.8)$$

where r_1 and r_2 are the range distance in the two different acquisitions, respectively.

Fig 2.3 shows the imaging geometry of an InSAR system. Because of the spatial baseline of the two acquisitions, there is a phase variation between two neighboring pixels. The phase difference is

$$\Delta\phi = -\frac{4\pi}{\lambda} \frac{B_{\perp}s}{R \tan\theta} - \frac{4\pi}{\lambda} \frac{B_{\perp}h}{R \sin\theta} \quad (2.9)$$

where B_{\perp} is the perpendicular spatial baseline between the two acquisitions, s is the slant range difference between two neighboring pixels in the range direction, h is the height difference, R is the range distance, θ is the look angle.

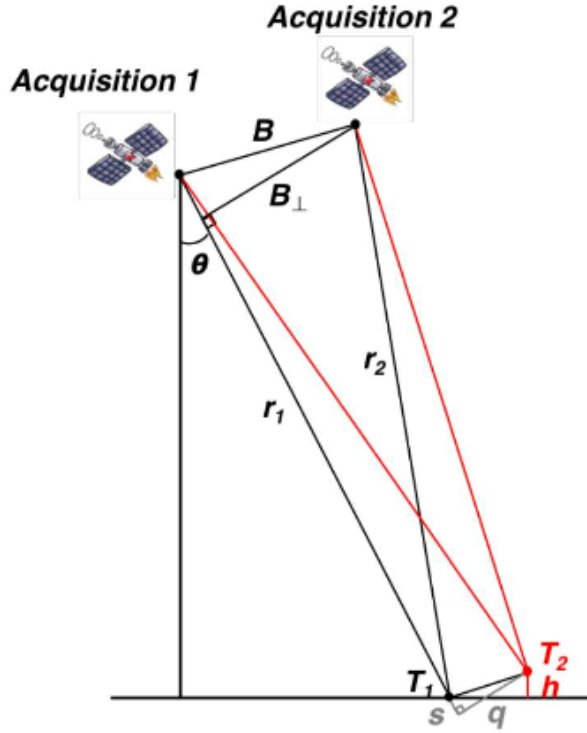


Figure 2.3 Illustration of the imaging geometry of an InSAR system. (modified from Lu and Dzurisin, 2014)

InSAR deformation maps can be influenced by geometrical and temporal decorrelation, atmospheric artifacts, topographic errors, and unwrapping errors. An interferometric phase has multiple components:

$$\phi = \phi_{def} + \phi_{topo} + \phi_{atm} + \phi_{orb} + \phi_{noise} \quad (2.10)$$

where ϕ_{def} is ground deformation, ϕ_{topo} is the residual topographic phase (DEM error), ϕ_{atm} is the atmospheric artifact, ϕ_{orb} is the residual orbit phase, and ϕ_{noise} is the noise between the two acquisitions.

The first part of Eq. 2.9 is because of the spatial separation of the two acquisitions and it should be reduced from the initial phase. The second part is called flattened interferometric phase. When there is no deformation between the two SAR images, the flatten phase can be used to extract the topographic elevation model (DEM), which means when there is deformation between the two SAR images,

$$\phi_{flatten} = \phi_{def} - \frac{4\pi}{\lambda} \frac{B_{\perp} h}{R \sin \theta} \quad (2.11)$$

The second part of Eq. 2.9 can also be used to represent DEM error ϕ_{topo} . ϕ_{topo} can be removed with a DEM.

2.3 InSAR time-series processing

InSAR time-series techniques are a class of methods that utilize a network of interferograms other than individual interferograms to retrieve information about the time-history of surface deformation.

2.3.1. Stacking

Stacking is an efficient InSAR method for estimating deformation rates, especially for poor-quality InSAR interferograms. By simply summing or stacking many interferograms, the signal to noise ratio (SNR) of InSAR measurements improves because the deformation signal reinforces while other phase components typically cancel out (Simons and Rosen, 2007). However, the assumption that the atmospheric statistics are stationary does not always hold in large-scale interferogram processing.

2.3.2. Small baseline SAR (SBAS)

The key strategy for the SBAS method is to minimize geometrical decorrelation and topographic error induced artifacts by only using interferograms formed with small temporal and spatial baselines, which provide more accurate time-series deformation. In the SBAS method, spatial averaging is often applied to further decrease decorrelation. Based on prior knowledge of the deformation signal, phase inversion methods such as least-squares (Schmidt and Bürgmann, 2003), singular value decomposition (Berardino et al., 2002), or L-1 norm minimization (Chen et al., 2014) can be used to retrieve the temporal evolution of phase values, hence time series of displacements. When SAR images are available from both ascending and descending tracks, Multidimensional Small Baseline Subset (MSBAS) can be applied by combining the two tracks for two-dimensional (vertical and east-west) deformation analysis (Samsonov and d'Oreye, 2017).

2.3.3. Persistent Scatterer Analysis

The SAR observation of a ground resolution cell is the coherent sum of contributions from all ground objects within the resolution cell. Relative movements of the ground objects and the changes in viewing angles of the satellite will cause a different summation then decorrelation in the interferograms. However, when a ground resolution cell is dominated by a single scatterer, which means the dominant scatterer returns significantly more energy than others, the total returned signals are much more stable. These pixels are called persistent scatterers (PS). The persistent scatterer InSAR (PSInSAR) technique (Ferretti et. al, 2001; Hooper et. al, 2004) identifies PS points in a stack of interferograms over the observation period to maintain good interferometric coherence.

2.4 InSAR applications in geohazards related to the oil and gas industry

InSAR is an effective tool to map ground deformation with centimeter to millimeter level precision and meter-level resolution in a large region, thus, small-sized and small-magnitude geohazards can be monitored (e.g., Massonnet and Feigl, 1998; Rosen et al., 2000; Lu and Dzurisin, 2014). It has been proved the capacity of detecting oil and gas industry related surface deformation (e.g., Yang et al., 2015) and induced seismicity (e.g., Shirzaei et al., 2016). Although the deformation caused by small-magnitude induced earthquakes may not be measurable by InSAR, InSAR can detect the previously-developed and currently developing surface deformation in the basin that potentially leads to catastrophic outcomes (e.g., surface collapse, pipeline leakage) in the near future. The abundant spaceborne SAR data archive such as ALOS-1/2 PALSAR-1/2, Sentinel-1A/B and TerraSAR-X, and future NISAR enables the long-term time-series tracking of the geohazards.

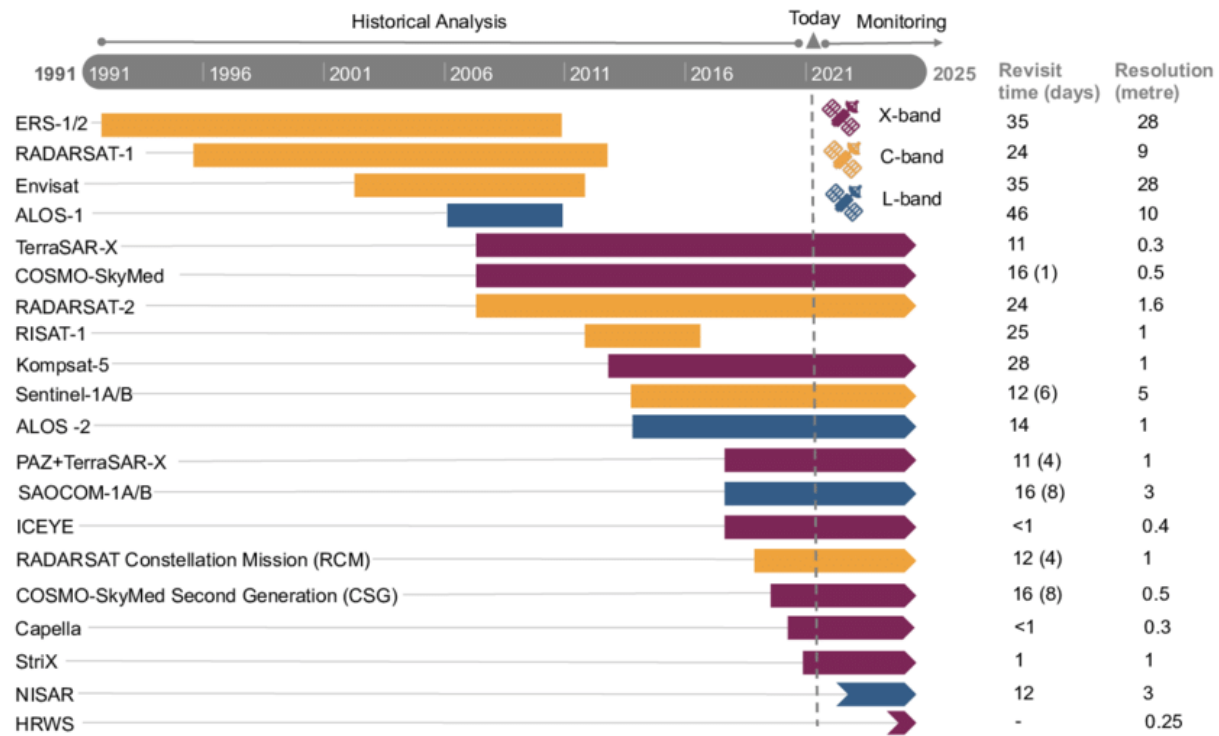


Figure 2.4 Timeline of past, present and future SAR missions between 1991 and 2025, and their main features. (Macchiarulo et al., 2022)

C-band Sentinel-1A/B imagery is a good choice to investigate the widely-distributed geohazards that are occurring in the whole Permian Basin considering the large coverage, short repeat cycle and continuously updating data. The ~250 km wide swath makes it possible to map the whole basin using essentially one ascending track and one descending track. The short time interval (6 or 12 days) allows dense observations over the vast basin. The continuously-acquired data offers the opportunity to monitor the state of newly developing geohazards and the development of other ongoing geohazards. Because the region is covered by short, sparsely distributed vegetation, C-band InSAR can maintain coherence throughout months or years. Once SAR datasets are acquired from NASA Alaska Satellite Facility, the interferograms can be

generated and the localized anomalies that can be considered as geohazards can be identified and categorized.

When the location and extent of the geohazards in the Delaware Basin are revealed, the progress of each geohazard can be captured by time-series InSAR measurement. The SBAS (Berardino et al., 2002) and PSInSAR (Hooper et al., 2004) methods can be used to generate time-series surface deformation in the Permian Basin. Troposphere correction via weather-models (e.g., TRAIN (toolbox for reducing atmospheric InSAR noise) (Bekaert et al., 2015), or GACOS (generic atmospheric correction online service for InSAR) (Yu et al., 2018) and ionosphere correction (particularly on L-band interferograms) via range split-spectrum methods (e.g., Fattahi et al., 2017) can be applied during the time-series InSAR processing. Being capable of collecting images from both ascending and descending tracks of Sentinel-1, Multidimensional Small Baseline Subset (MSBAS) will be applied by combining the two tracks for two-dimensional (vertical and east-west) deformation analysis (Samsonov and d'Oreye, 2017). The initial InSAR results can be further scrutinized with more SAR sensors from ALOS-1/2 (L band), and TerraSAR-X (X band) to monitor the history and the ongoing development of the selected geohazards.

Reference

- Bamler, R., and Hartl, P. 1998. Synthetic aperture radar interferometry. *Inverse problems*, 14(4), R1.
- Bekaert, D.P.S., Walters, R.J., Wright, T.J., Hooper, A.J., and Parker, D.J., 2015, Statistical comparison of InSAR tropospheric correction techniques, *Remote Sens. Environ.*, 170, 40–47. <https://doi.org/10.1016/j.rse.2015.08.035>
- Berardino, P., Fornaro, G., Lanari, R., and Sansosti, E., 2002, A new algorithm for surface deformation monitoring based on small baseline differential SAR interferograms, *IEEE Trans. Geosci. Remote Sens.*, 40, 2375–2383.
- Chen, J., Zebker, H.A., Segall, P. and Miklius, A., 2014. The 2010 slow slip event and secular motion at Kīlauea, Hawaii, inferred from TerraSAR-X InSAR data. *Journal of Geophysical Research: Solid Earth*, 119(8), pp.6667-6683.
- Cumming, I. G., & Wong, F. H. 2005. Digital processing of synthetic aperture radar data. Artech house, 1(3), 108-110.
- Curlander, J. C., and R. N. McDonough 1991. Synthetic aperture radar: systems and signal processing (book), New York: John Wiley & Sons, Inc.
- Fattahi, H., Simons, M., & Agram, P. 2017. InSAR time-series estimation of the ionospheric phase delay: An extension of the split range-spectrum technique. *IEEE Transactions on Geoscience and Remote Sensing*, 55(10), 5984-5996.
- Ferretti, A., Prati, C., & Rocca, F. 2001. Permanent scatterers in SAR interferometry. *IEEE Transactions on Geoscience and Remote Sensing*, 39(1), 8–20.
- Hanssen, R. 2001. *Radar Interferometry: Data Interpretation and Error Analysis*, vol. 2. Dordrecht, The Netherlands: Kluwer.
- Hooper, A., Zebker, H., Segall, B., and Kampes, B., 2004, A new method for measuring deformation on volcanoes and other natural terrains using InSAR persistent scatterers, *Geophys. Res. Lett.*, 31, L23611.
- Lu, Z., and D. Dzurisin. 2014. *InSAR Imaging of Aleutian Volcanoes: Monitoring a Volcanic arc from Space*, Geophysical Sciences, Springer Praxis Books, Springer: Chichester, UK, 2014, p. 390.
- Macchiarulo, V., Milillo, P., Blenkinsopp, C., Reale, C., & Giardina, G. 2022. Multi-temporal InSAR for transport infrastructure monitoring: recent trends and challenges. In *Proceedings of the Institution of Civil Engineers-Bridge Engineering* (pp. 1-26). Thomas Telford Ltd.

- Massonnet, D. and Feigl, K., 1998, Radar interferometry and its application to changes in the Earth's surface, *Reviews of Geophysics*, 36, 441–500.
- Moreira, A., Prats-Iraola, P., Younis, M., Krieger, G., Hajnsek, I., & Papathanassiou, K. P. (2013). A tutorial on synthetic aperture radar. *IEEE Geoscience and remote sensing magazine*, 1(1), 6-43.
- Rosen, P. A., Hensley, S., Li, F., Joughin, I., Madsen, S., and Goldstein, D., 2000, Synthetic aperture radar interferometry, *Proceedings of the IEEE*, 88(3), 333–382.
- Samsonov, S. and d'Oreye, N., 2012, Multidimensional time-series analysis of ground deformation from multiple InSAR data sets applied to Virunga volcanic province, *Geophys. J. Int.*, 191, 1095–1108.
- Schmidt, D.A. and Bürgmann, R., 2003. Time-dependent land uplift and subsidence in the Santa Clara valley, California, from a large interferometric synthetic aperture radar data set. *Journal of Geophysical Research: Solid Earth*, 108(B9).
- Shirzaei, M., Ellsworth, W. L., Tiampo, K. F., González, P. J., and Manga, M., 2016, Surface uplift and time-dependent seismic hazard due to fluid injection in eastern Texas, *Science*, 353(6306), 1416-1419.
- Simons, M. and Rosen, P.A., 2007. Interferometric synthetic aperture radar geodesy. *Geodesy*, 3, pp.391-446.
- Yang, Q., Zhao, W., Dixon, T. H., Amelung, F., Han, W. S., and Li, P., 2015, InSAR monitoring of ground deformation due to CO₂ injection at an enhanced oil recovery site, West Texas, *International Journal of Greenhouse Gas Control*, 41, 20-28.
- Yu, C., Li, Z., & Penna, N. T. 2018. Interferometric synthetic aperture radar atmospheric correction using a GPS-based iterative tropospheric decomposition model. *Remote Sensing of Environment*, 204, 109-121.
- Zebker, H. A., Rosen, P. A., Goldstein, R. M., Gabriel, A., & Werner, C. L. 1994. On the derivation of coseismic displacement fields using differential radar interferometry: The Landers earthquake. *Journal of Geophysical Research: Solid Earth*, 99(B10), 19617-19634.

CHAPTER 3

Modeling work

3.1 Poroelasticity

The subject of poroelasticity consists of two coupling effects: (1) solid to fluid coupling occurs when a change in stress produces a change in fluid pressure or fluid mass (e.g., compression of the rock induces a rise of pore pressure); (2) fluid to solid coupling occurs when a change in fluid pressure or fluid mass produces a change in the volume of the porous material (e.g., an increase of pore pressure induces a dilation of the rock).

Linear isotropic poroelastic processes can be described by the constitutive equations for the porous solid and the fluid, Darcy's law, the momentum conservation equation, and the continuity equation (mass conservation). Field equations including Navier equations and diffusion equations have been derived to reduce the number of variables, some of which are uncoupled based on assumptions.

The Biot's theory was formulated as the general three-dimensional theory of poroelasticity that is consistent with the two coupling effects. Simple and complex analytical solutions for practical problems have been developed, while numerical solutions allow more realistic simulations of the poroelastic behaviors.

The fundamental equations based on Biot's theory consist of momentum conservation (Eq. 3.1) and the continuity equation for mass conservation (Eq. 3.2):

$$\nabla \cdot \boldsymbol{\sigma} - \alpha \nabla p = \mathbf{f}, \quad \boldsymbol{\sigma} = \mathbf{D} \boldsymbol{\epsilon}, \quad (3.1)$$

where \mathbf{D} is the elasticity matrix which can be represented with Young's modulus E and Poisson's ratio ν , α is the tensor matrix for Biot's coefficient,

$$C\dot{p} - \nabla \cdot \frac{K}{\rho_f g} \nabla p - \alpha \epsilon = q, \quad (3.2)$$

where the compressibility $C = \frac{\alpha - \varphi}{K_s} + \frac{\varphi}{K_f}$, φ is porosity, K_s is the bulk modulus of rock, K_f is the bulk modulus of fluid, K is hydraulic conductivity, ρ_f is the fluid density.

3.2 Method of solution

3.2.1 Analytical solutions

The soil-pore fluid interaction (the relationship between soil strain and pore pressure) is a coupled system, which means that neither domain can be solved while separated from the other, and neither set of dependent variables can be explicitly eliminated at the differential equation level. However, analytical solutions based on specific assumptions can simplify and decouple the problem.

For fluid injection/extraction problem, Mathias et al. (2009) and Theis (1935) presented a simplified model of pressure increase and decline due to fluid injection and fluid extraction, respectively:

$$P_{inj}(r, t) = P_0 \left\{ \frac{1}{2\gamma} E_i \left(\frac{\alpha\chi}{4\gamma} \right) + \frac{1}{2\gamma} \left[\ln \left(\frac{\alpha\chi}{4\gamma} \right) + 0.57772 \right] \right\} \\ + P_0 \left\{ \begin{array}{ll} -\frac{1}{2} \ln \left(\frac{\chi}{2\gamma} \right) - 1 + \frac{1}{\gamma} - \frac{1}{\gamma} \left[\ln \left(\frac{\alpha}{2\gamma^2} \right) + 0.57772 \right] & \chi \leq 2\gamma \\ -\left(\frac{\chi}{2\gamma} \right)^{0.5} + \frac{1}{\gamma} - \frac{1}{2\gamma} \left[\ln \left(\frac{\alpha}{2\gamma^2} \right) + 0.57772 \right] & 2\gamma \leq \chi \leq \frac{2}{\gamma} \\ -\frac{1}{2\gamma} \left[\ln \left(\frac{\alpha\chi}{4\gamma} \right) + 0.57772 \right] & \chi \leq \frac{2}{\gamma} \end{array} \right\} \quad (3.3)$$

$$P_{pro}(r, t) = -\frac{Q_v \mu_p}{4\pi H k} E_i \left(-\frac{\mu_p (\varphi C_p + C_{rock}) r^2}{4kt} \right) \quad (3.4)$$

where E_i is the exponential integral operator defined as

$$\begin{aligned} E_i(x) &= -\int_{-x}^{\infty} \frac{e^{-t}}{t} dt \\ P_0 &= \frac{Q_m \mu_f}{2\pi H \rho_f k} \\ \gamma &= \frac{\mu_f}{\mu_{brine}} \\ \chi &= \frac{(r/r_w)^2}{t Q_m / (2\pi \varphi H r_w^2 \rho_f)} \\ \alpha &= \frac{Q_m \mu_f (C_{rock} + C_{brine})}{2\pi H \rho_f k} \end{aligned} \quad (3.5)$$

where r is the radial distance to the injection well (m); Q_m is the mass injection rate (kg/s); μ_f is the viscosity of injected fluid (Pa·s); H is the formation thickness (m); ρ_f is the density of injected fluid (kg/m³); k is the formation permeability (m²); μ_{brine} is the brine viscosity (Pa·s); r_w is the injection well radius (m); φ is the formation porosity; C_{rock} is the formation compressibility (Pa⁻¹) and C_{brine} is the brine compressibility (Pa⁻¹); Q_v is the volume production rate (m³/s); μ_p is the viscosity of produced fluid (Pa·s); C_p is the compressibility of produced fluid (Pa⁻¹).

3.2.2 Finite element method

Because of the complexity of the poroelastic governing equations, it is generally difficult to derive analytical solution of initial/boundary value problems, except for cases with simple

geometries. Even when analytical solutions exist, numerical methods may still be utilized since the forms are usually infinite series or integral transforms.

The finite element method has been utilized widely in practice because it allows material heterogeneity, irregular boundaries, distributed mechanical loads and fluid sources. The finite element method is based on the Galerkin weighted residual procedure and a finite element segmentation. Many FEM simulators based on Biot's theory have been developed.

The coupled system of equations can be rewritten as Eq. 3.6 using the finite element method:

$$\begin{aligned} \mathbf{K}_e \mathbf{u} - \mathbf{H} \mathbf{p} &= \mathbf{f} \\ \mathbf{H}^T \dot{\mathbf{u}} + \mathbf{S} \dot{\mathbf{p}} + \mathbf{Q} \mathbf{p} &= \mathbf{q} \end{aligned} \quad (3.6)$$

where \mathbf{u} is the column matrix of the nodal displacements, \mathbf{p} is the nodal pressure, \mathbf{f} is the body force, and \mathbf{q} takes into account the mass flux at a well. The others are square matrices. \mathbf{K}_e is solid stiffness matrix, \mathbf{H} is the coupling matrix that describes the coupling between volume changes in the solid and pressure changes in the pore fluid, \mathbf{S} is the compressibility matrix of the mixture of solids and fluids, \mathbf{Q} is the mass loss or gain from fluid flow in response to pore pressure gradients:

$$\begin{aligned} \mathbf{K}_e &= \int_{\Omega} \mathbf{B}^T \mathbf{D} \mathbf{B} \, dx \\ \mathbf{H} &= \int_{\Omega} \mathbf{B}^T \alpha \mathbf{N} \, dx \\ \mathbf{Q} &= \int_{\Omega} \nabla^T \mathbf{N} \frac{K}{\rho_f g} \nabla \mathbf{N} \, dx \\ \mathbf{S} &= \int_{\Omega} \mathbf{N}^T \mathbf{C} \mathbf{N} \, dx \end{aligned} \quad (3.7)$$

where Ω is the domain of solution, \mathbf{D} is the elasticity coefficient matrix, \mathbf{N} is the shape function, \mathbf{B} is the strain differential operator matrix.

3.3 Inverse method for geohazards related to oil and gas industry

3.3.1 Bayesian inversion

Bayesian inversion has been widely used for various types of geophysical inverse problems. The advantages of the Bayesian approach include: allowing for a priori knowledge about the parameters (i.e., easily giving constraints to the parameters); providing the description of the data and model errors after accounting for the data; and dealing with problems that are not deterministic or where no exact direct model or coupling exists. The Bayesian approach can update the probability density function of an interested parameter sequentially and thus calculate probabilistic data including not only the maximum a posteriori (MAP) estimates but also the confidence intervals of each parameter.

For the inverse poroelastic problem of solving precise mechanical and hydrogeologic parameters using InSAR observation and injection/production information, the data vector $\mathbf{d} = \{d^1, d^2, \dots, d^{N_D}\}$ (i.e., the spatial and temporal deformation observed by InSAR), is equal to a model function, \mathbf{G} (i.e., the analytical model or numerical model), of the model parameters $\mathbf{m} = \{m^1, m^2, \dots, m^{N_M}\}$ (i.e., interested mechanical and hydrogeologic parameters) plus error ϵ :

$$\mathbf{d} = \mathbf{G}(\mathbf{m}) + \epsilon \quad (7)$$

In a Bayesian framework, the posterior probability density function (PDF), $p(\mathbf{m}|\mathbf{d})$, gives the probability distribution of the estimated parameters \mathbf{m} representing the goodness of explaining the data \mathbf{d} , can be calculated as:

$$p(\mathbf{m}|\mathbf{d}) = \frac{p(\mathbf{d}|\mathbf{m})p(\mathbf{m})}{p(\mathbf{d})} \quad (8)$$

where $p(\mathbf{d}|\mathbf{m})$ is the likelihood function, expressing the probability distribution of \mathbf{d} when the parameters are given as \mathbf{m} based on the misfit between \mathbf{d} and the predicted model $\mathbf{G}(\mathbf{m})$; $p(\mathbf{m})$ is the prior PDF, quantifying prior information about \mathbf{m} independent to \mathbf{d} , allowing constraints for the mechanical and hydrogeologic parameters from previous research; $p(\mathbf{d})$ is a normalizing factor that does not rely on \mathbf{m} .

Suppose the errors are multivariate Gaussian with zero mean, and covariance matrix Σ_d , $\epsilon \sim N(0, \Sigma_d)$, the likelihood function can be calculated as:

$$p(\mathbf{d}|\mathbf{m}) = (2\pi)^{-\frac{N_D}{2}} |\Sigma_d|^{-\frac{1}{2}} \exp \left\{ -\frac{1}{2} [\mathbf{d} - \mathbf{G}(\mathbf{m})]^T \Sigma_d^{-1} [\mathbf{d} - \mathbf{G}(\mathbf{m})] \right\} \quad (9)$$

where Σ_d^{-1} is the inverse of the covariance matrix. This calculation can be extended to multiple datasets (i.e., multiple InSAR images). Consider K datasets, the data vector of the k th dataset would be:

$$\mathbf{d}_k = \mathbf{G}_k(\mathbf{m}) + \epsilon_k, \quad k = 1, 2, \dots, K \quad (10)$$

The likelihood function for multiple datasets can be calculated as:

$$p(\mathbf{d}_1, \mathbf{d}_2, \dots, \mathbf{d}_K | \mathbf{m}) = \prod_{k=1}^K (2\pi)^{-\frac{N_k}{2}} |\Sigma_k|^{-\frac{1}{2}} \exp \left\{ -\frac{1}{2} [\mathbf{d}_k - \mathbf{G}_k(\mathbf{m})]^T \Sigma_k^{-1} [\mathbf{d}_k - \mathbf{G}_k(\mathbf{m})] \right\} \quad (11)$$

where N_k is the number of data points of the k th dataset.

Prior information can be gathered through previous geologic research or well logs. If some of the parameters have exact values through on-site measurements, the model parameters space can be reduced by regarding them as constants.

3.2.3 Optimization method

The Markov Chain Monte Carlo (MCMC) technique is a robust method to sample and therefore characterize a posterior probability distribution in the Bayesian inference. The MCMC method generates random samples and explores the search space with a Markov Chain designed approach to spend more time around the maximum of the cost function. MCMC is time-consuming in high dimensions because it is fairly reliable and can work for complicated distributions in high-dimensional spaces. In sampling the posterior probability distribution with a Markov Chain designed approach, MCMC spends more time in the important regions and the density of the samples can approximate the posterior probability distribution after a large number of iterations.

MCMC begins with an initial series of model parameters $\mathbf{m}_{i=0}$ based on the prior information $p(\mathbf{m})$, where i is the number of times of the iterations. The initial values can be parameters from previous research or just chosen randomly in the allowed domain. The corresponding likelihood function $p(\mathbf{d}|\mathbf{m}_i)$ can be then estimated. A new series of model parameters can be generated by making a perturbation to each parameter in \mathbf{m}_i . By calculating the new likelihood function $p(\mathbf{d}|\mathbf{m}_{i+1})$ and comparing it with the previous one, the changes in model parameters will be accepted if $p(\mathbf{d}|\mathbf{m}_{i+1}) > p(\mathbf{d}|\mathbf{m}_i)$. However, if the new likelihood value is less than the previous one, the change will not be simply rejected but will be accepted with a probability as the ratio of the new likelihood value and the previous one. This means that the changes will still be accepted if $p(\mathbf{d}|\mathbf{m}_{i+1})/p(\mathbf{d}|\mathbf{m}_i) \geq a$, where a is a random number in the range of 0 to 1, while, if $p(\mathbf{d}|\mathbf{m}_{i+1})/p(\mathbf{d}|\mathbf{m}_i) \leq a$, the trial series of parameters in \mathbf{m}_{i+1} will be replaced by values of \mathbf{m}_i . This mechanism makes MCMC less likely to be trapped in the local minima. New series of model parameters will be generated and the steps explained above

will be iterated. The loop will be terminated when the posterior probability distribution is believed to be approximated (usually 10^5 - 10^7 interactions).

MCMC requires huge computation especially when the search space is large, but it is still rewarding since it gives access to the joint PDF of the model parameters, which can be used to assess the precision of the estimates. The values with maximum probability will be regarded as the final solutions of the mechanical and hydrogeologic parameters.

Reference

- Biot, M. A. (1941). General theory of three-dimensional consolidation. *Journal of applied physics*, 12(2), 155-164.
- Idier, J. (Ed.). (2013). *Bayesian approach to inverse problems*. John Wiley & Sons.
- Lewis, R. W. and Schrefler, B.A. (1998) *The Finite Element Method in the Static and Dynamic Deformation and Consolidation of Porous Media*. John Wiley & Sons.
- Meng, C., (2017). Benchmarking Defmod, an open source FEM code for modeling episodic fault rupture. *Computers & Geosciences*, 100, pp.10-26.
- Sambridge, M., & Mosegaard, K. (2002). Monte Carlo methods in geophysical inverse problems. *Reviews of Geophysics*, 40(3), 3-1.
- Wang, H. (2000). *Theory of linear poroelasticity with applications to geomechanics and hydrogeology* (Vol. 2). Princeton university press.
- Zienkiewicz, O. and Taylor, R. (2000). *The Finite Element Method: The Basis*. Butterworth-Heinemann.

CHAPTER 4

Permian Basin background

4.1 Permian Basin geology

The Permian Basin, located in western Texas and southeastern New Mexico, occupies about 169,330 km². As shown in Fig. 4.1, the Permian Basin comprises three main tectonic components: the Delaware Basin (containing carbonate deposits of the Delaware Mountain Group), Midland Basin (also containing carbonate deposits originating from the Guadalupian times) and Central Basin Platform (comprising carbonate reef deposits and shallow marine clastic sediments) (Galley, 1958).

The depositional history of the Permian basin can be subdivided into three distinct stages (Adams, 1965; Ward et al., 1986). After the breakup of the late Precambrian super continent, during the early part of the Paleozoic Era (approximately 600 to 350 million years ago), the Permian Basin was inundated by relatively shallow seas, shallow-marine deposition dominated the early Paleozoic sedimentation, consisting mainly of relatively uniform and widespread shelf carbonates and sandstones and thin basinal shales (Hills, 1984). Then by the Permian Period, the geometry of the Permian Basin consisted of two sags separated by a platform established as a result of the Hercynian collisional orogeny. This intense tectonic movement resulted in the deposition of widespread siliciclastic sediments in the deeper basins during the early Pennsylvania and was followed by the development of carbonate shelves and margins around the edges of these foreland basins during the early Permian. In the Permian and post Permian period,

sediments filled the newly created foreland basins. The Midland and Delaware Basins were mainly sandstone fills while the platforms and shelves were sites of carbonate deposition.

The Permian Basin has experienced several divergent and convergent deformation events since the Proterozoic Eon. Each subsequent event was influenced by the accumulated tectonic fabric through fault reactivation and strain transfer. These events have generated a complex network of regional faults that have spatially compartmentalized the Permian Basin (Horne et al., 2021) (Fig. 4.1). It is important to learn the detailed fault network to improve the research about ground deformation and induced seismicity in this region.

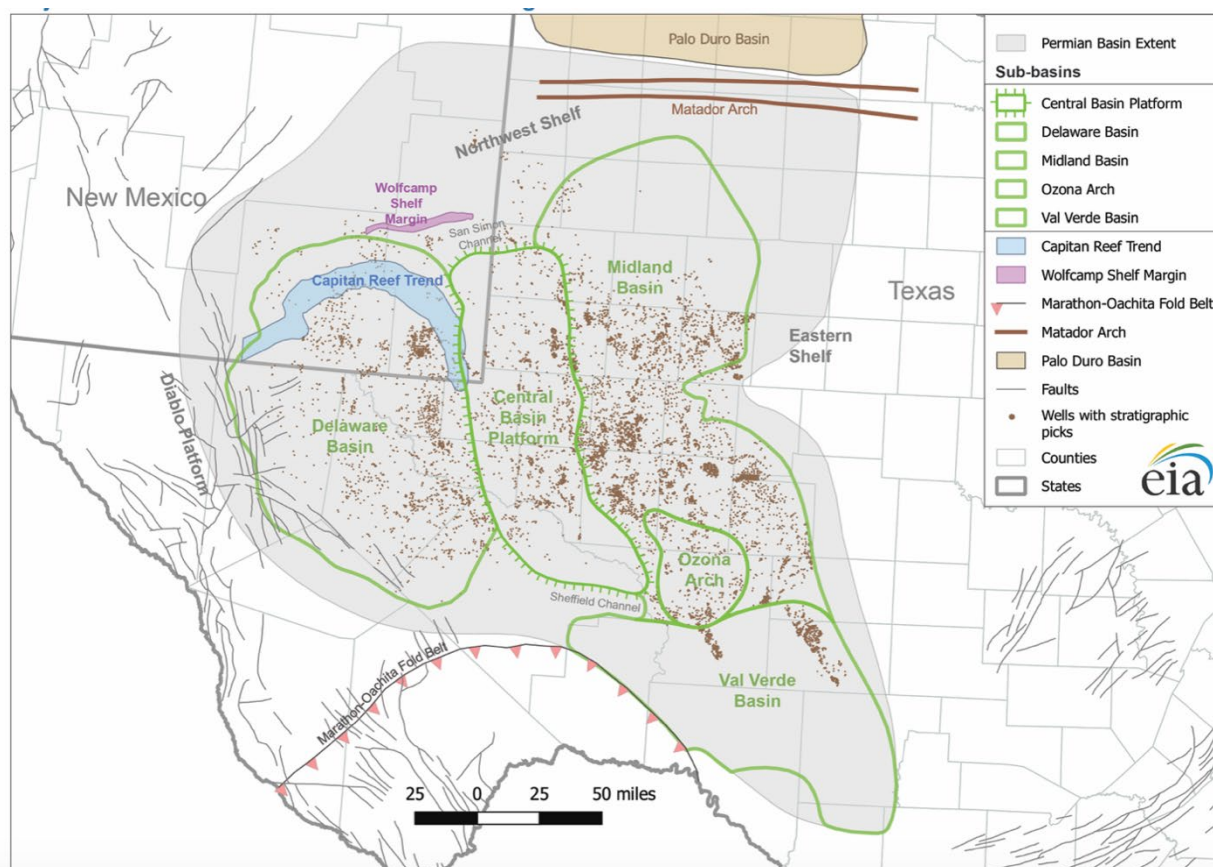


Figure 4.1 Major structural and tectonic features in the region of the Permian Basin. Image Source: U.S. Energy Information Administration based on DrillingInfo Inc., U.S. Geological Survey.

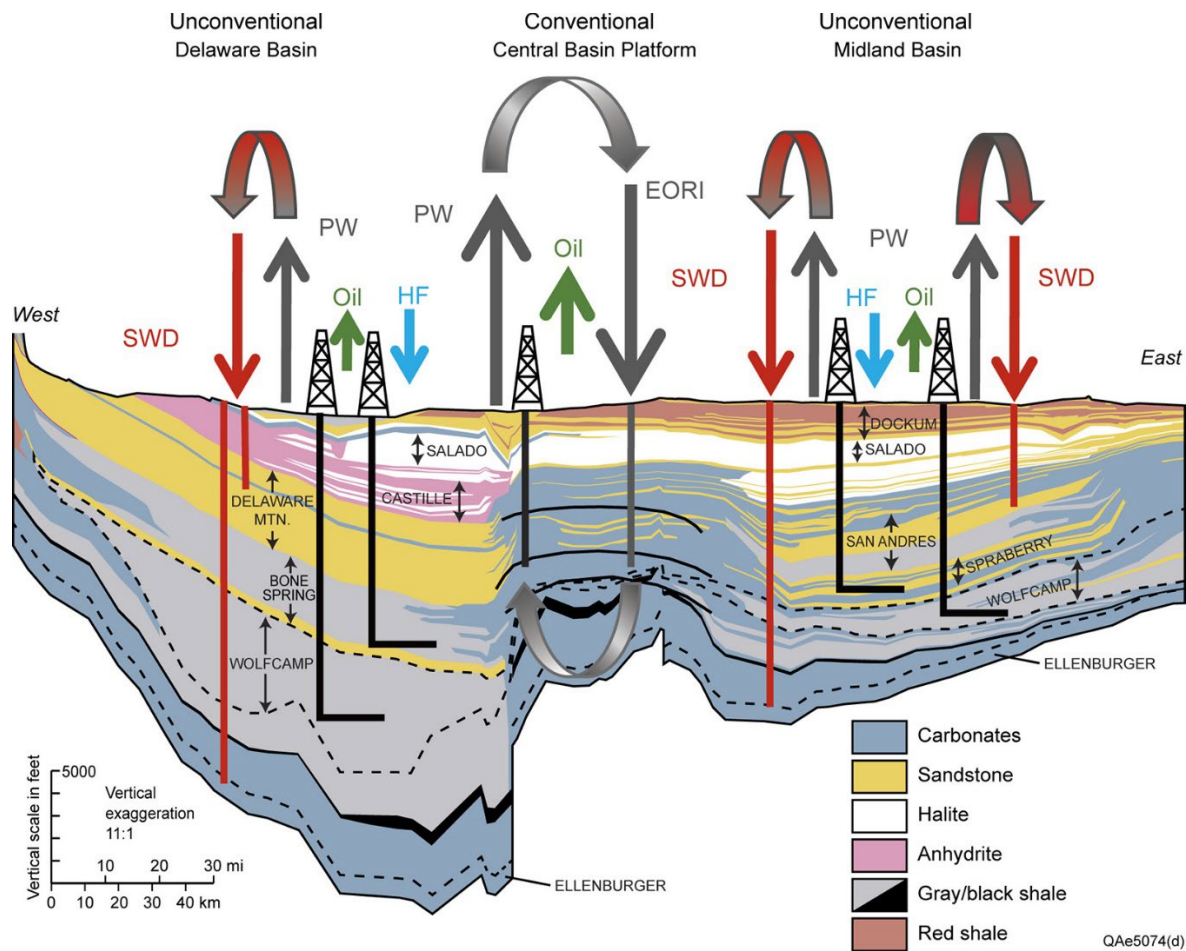


Figure 4.2 East–west cross section along the southern margin of the Permian Basin. (Scanlon et al., 2017)

4.2 Hydrocarbon production

The Permian Basin is one of the largest oil producing provinces in the United States (Fig. 4.3). More than 40,000 producing wells have been installed since 2011. According to U.S. Energy Information Administration, the oil production rate in this region is 1,057 barrels per day and the gas production exceeds 2,050 thousand cubic feet per day. The large oil and gas production is mainly attributed to the substantial remaining deposits of hydrocarbon in the reservoirs (Dutton et al., 2005), but the use of unconventional hydrocarbon production methods

(e.g., hydraulic fracturing (Fig. 4.4a), enhanced oil recovery (EOR) techniques (Fig. 4.4d)) also largely contributed to the massive hydrocarbon production.

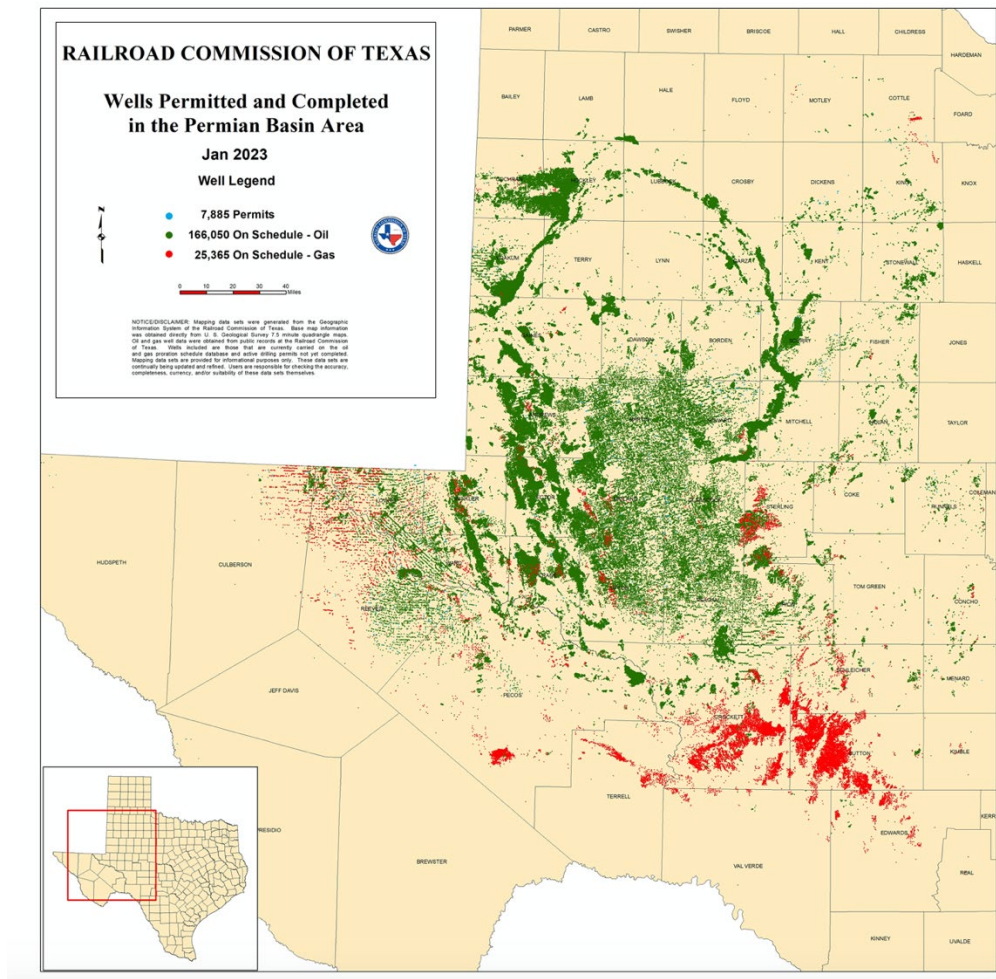


Figure 4.3 Permian Basin production wells (from Texas RRC).

According to a recent assessment from U.S. Geological Survey (2018), the Delaware Basin contains undiscovered resources of 46.3 billion barrels of oil and 281 trillion cubic feet of gas in the Bone Spring and Wolfcamp Formation. Hydrocarbon extraction from these shale

formations with conventional methods could be relatively hard. The unconventional hydrocarbon production methods can produce fractures in the rock formation that stimulate the flow of natural gas or oil, increasing the volumes that can be recovered. With these new methods, shale gas extraction, production of coalbed methane and hydrocarbon production in tight sands are all economically viable. In the Permian Basin, horizontal wells have been installed from hundreds in 2010 to thousands nowadays according to EIA.

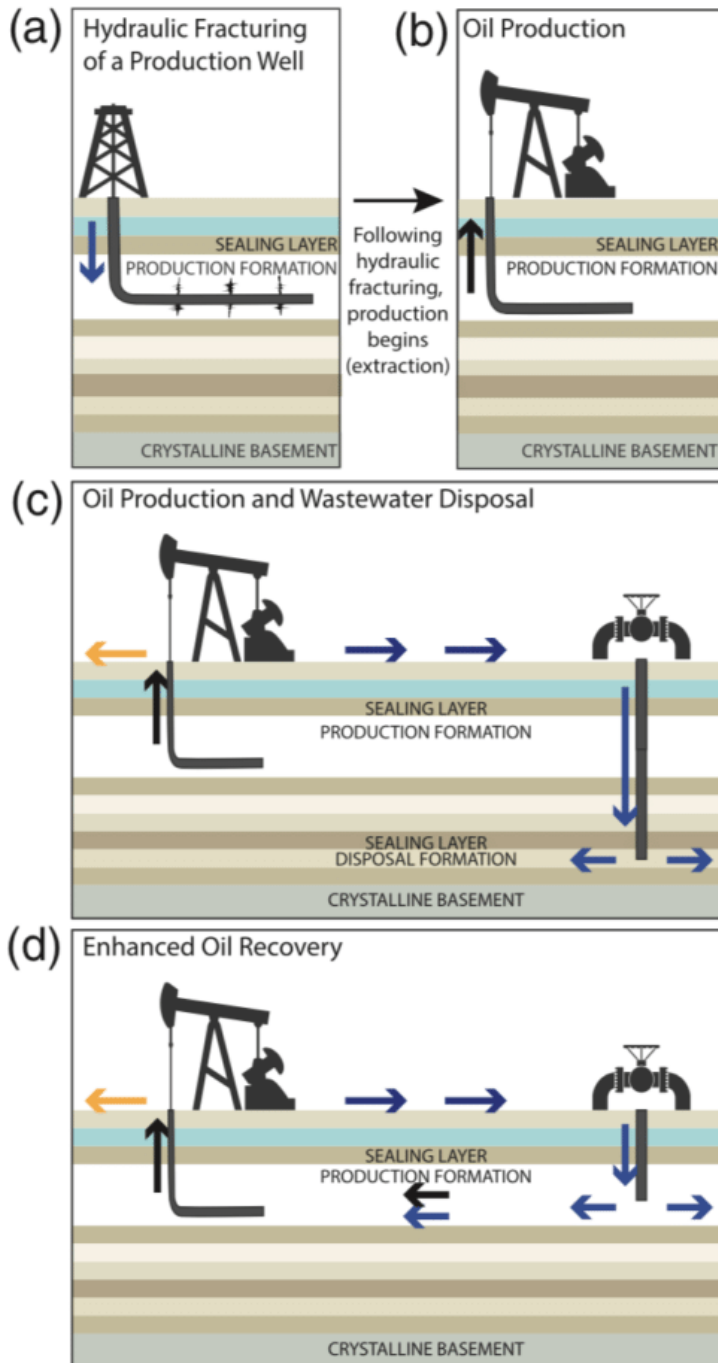


Figure 4.4 Simplified diagrams of oil-field operations. The geology in these diagrams is simplified from natural situations in which there are many more rock layers. Arrows show the directions of fluid being injected or withdrawn. The arrow color indicates the contents of the fluid: black (oil, gas, and wastewater), yellow (oil and gas), and blue (wastewater). (a) In a hydraulic fracturing operation, fluids are injected at high pressure into a production well, causing fractures in the surrounding rock that increase permeability. The increased permeability allows the extraction of oil or gas from a larger region. Following the hydraulic fracturing of a well, the

well goes into production (b). (c) Production wells extract oil and gas, and as a byproduct, salt water (commonly called “produced water” or “wastewater”), which is injected to a different subsurface formation at a disposal well. (d) Enhanced oil recovery (EOR), an alternative to wastewater disposal, involves injecting the water back into the formation holding the oil and gas to sweep oil and gas toward the production well. (Rubinstein and Mahani, 2015)

4.3 Human impacts

As the Permian Basin is located in the mid-continent region of the United States, the lithosphere here is tectonically stable. Considering the densely distributed oil and gas wells (Fig. 4.3), geohazards in the Permian Basin are usually regarded to be oil and gas industry related. 90 years of intense hydrocarbon production in the Permian Basin has negatively impacted the surface and subsurface stability. Conventional hydrocarbon production techniques that extract oil and gas by natural pressure from the wells may not cause immediate, significant effects on the surface stability. However, despite the economic benefits, the unconventional hydrocarbon producing techniques using fluid injection into the shale and sand formations to capture oil and gas may have a greater impact on solid earth stability, particularly over long periods of time (Zoback, 2010).

4.3.1 Ground deformation

The dominant geohazard in the Permian Basin is surface deformation (subsidence or uplift) (Kim and Lu, 2018). Hydrocarbon production may cause surface subsidence as the oil and gas are pumped out from underground. Fluid injection including wastewater disposal and CO₂ injection for enhanced oil recovery increases pore pressure inside the injection zone, the pressure perturbation will propagate to overlying layers with time, causing surface uplift. Regional (to basin scale) and localized (kilometer scale) ground deformation in the Permian Basin has been

detected by InSAR with its large coverage, meter level resolution, short repeat cycle and continuously updating data (Kim and Lu, 2018; Staniewicz et al., 2020).

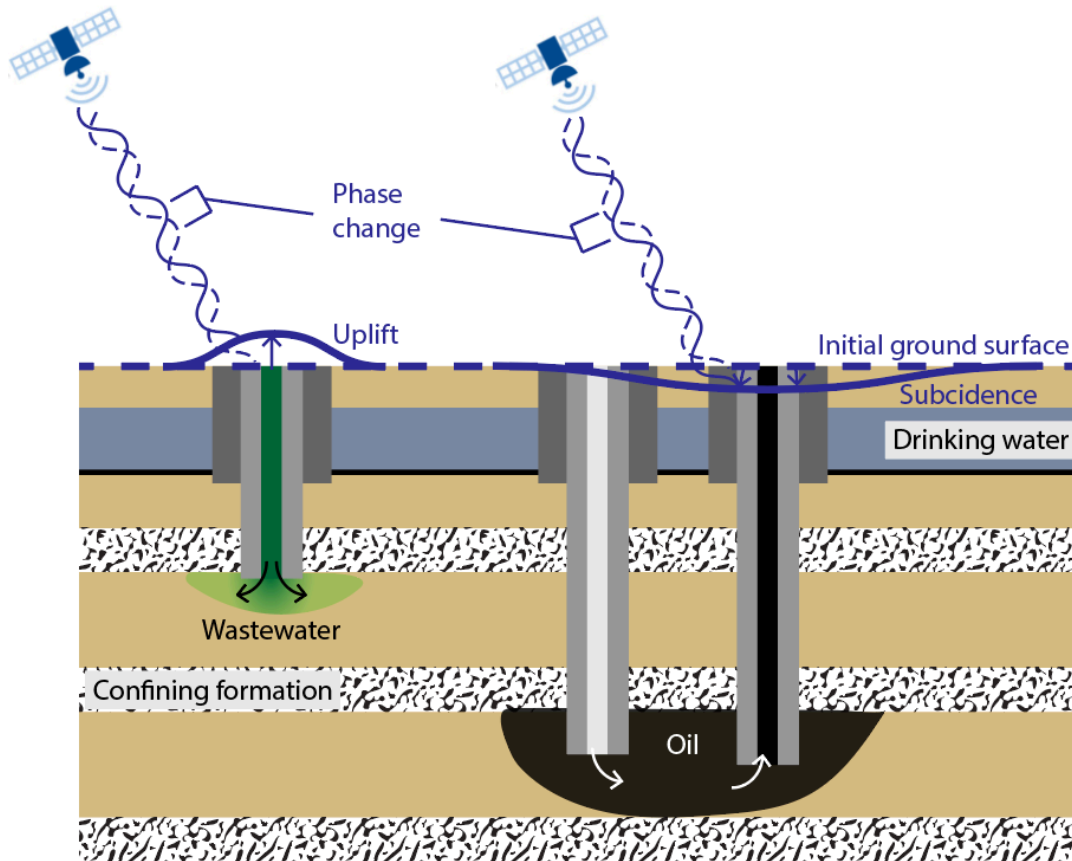


Figure 4.5 Illustration of InSAR detection of ground deformation induced by Wastewater injection and enhanced recovery wells.

4.3.2 Induced seismicity

In some cases, the increasing pore pressure due to fluid injection decreases the effective normal stress on adjacent faults, enhancing chances of failure and finally triggering induced seismicity. The critical stress fault failure can be written as

$$\tau_{critical} = C + \mu(\sigma_n - P) \quad (4.1)$$

Where C is the cohesive strength of the fault surface, μ is the coefficient of state friction. σ_n is the normal stress, P is the pore pressure (Jaeger and Cook, 1969).

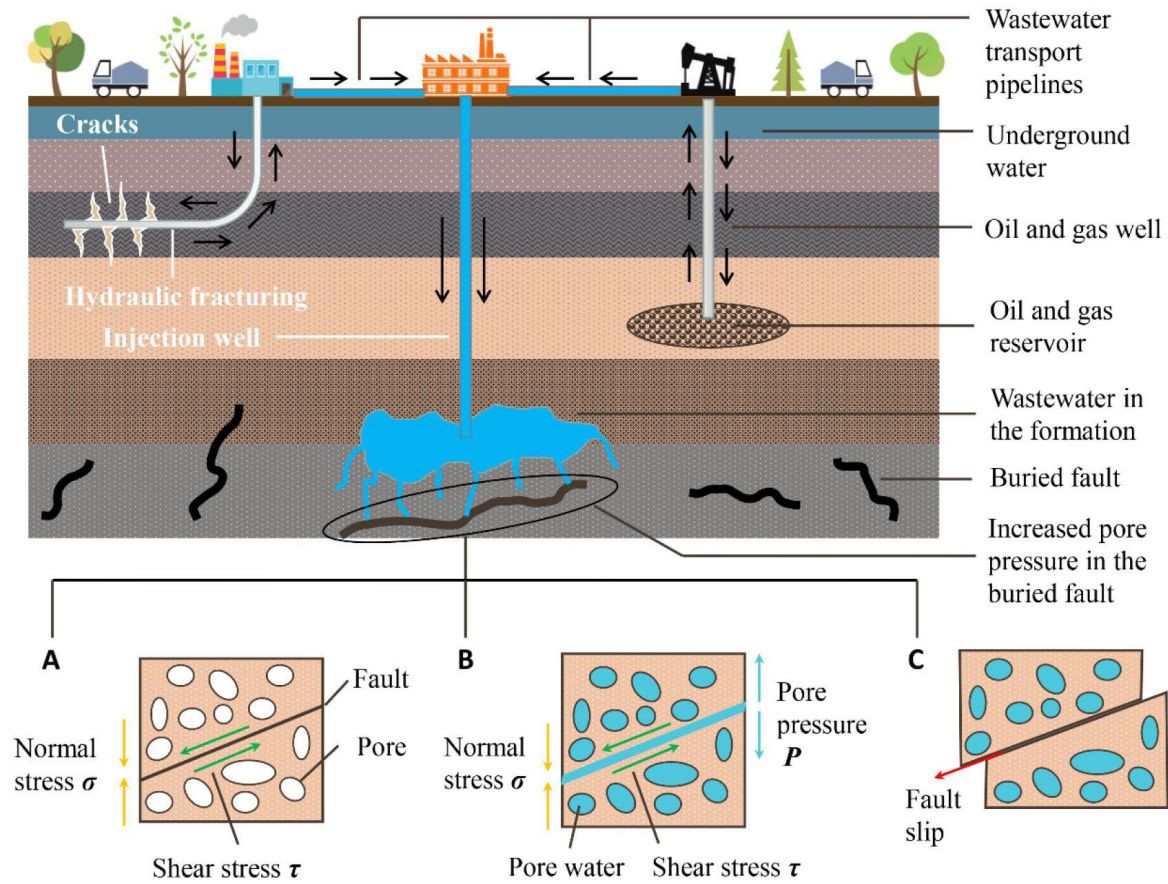


Figure 4.6 The whole process of fault slip induced by fluid injection in industrial production (He et al., 2020).

The induced seismicity rate in the Permian Basin has increased in recent years mainly due to human activities (Ellsworth, 2013). The increase has been attributed to large-volume wastewater disposal, hydraulic fracturing, and carbon sequestration. The induced seismicity rate

in the Delaware Basin has increased by orders of magnitude within the past ~5 years, and the vast majority of the seismicity is most likely associated with wastewater disposal (Skoumal et al., 2019; Zhai et al., 2021). Several studies have investigated how to link certain instances of wastewater injection and hydraulic fracturing to induced seismicity (Skoumal et al., 2020; Grigoratos et al., 2020).

Reference

- Adams, J. E., 1965. Stratigraphic-tectonic development of Delaware Basin. AAPG bulletin, 49(11), 2140-2148.
- Dutton, S.P., Kim, E.M., Broadhead, R.F., Raatz, W.D., Breton, C.L., Ruppel, S.C., and Kerans, C., 2005, Play analysis and leading-edge oil-reservoir development methods in the Permian basin: Increased recovery through advanced technologies, AAPG Bull., 89, 5, 553-576.
- Ellsworth, W. L. (2013). Injection-induced earthquakes. Science, 341(6142), 1225942.
- Galley, J. E., 1958, Oil and geology in the Permian Basin of Texas and New Mexico: North America, in L. G. Weeks, ed., Habitat of Oil: AAPG, 395-446.
- Gaswirth, S. B., French, K. L., Pitman, J. K., Marra, K., Mercier, T. J., Leathers-Miller, H., M., Schenk, C. J., Tennyson, M. E., Woodall, C. A., Brownfield, M. E., Finn, T. M., and Le, P. A., 2018, *Assessment of Undiscovered Continuous Oil and Gas Resources in the Wolfcamp Shale and Bone Spring Formation of the Delaware Basin, Permian Basin Province, New Mexico and Texas*, 2018. No. 2018-3073. US Geological Survey.
- Grigoli, F., Cesca, S., Priolo, E., Rinaldi, A. P., Clinton, J. F., Stabile, T. A., Dost, B., Fernandez, M. G., Wiemer, S., and Dahm, T., 2017. Current challenges in monitoring, discrimination, and management of induced seismicity related to underground industrial activities: A european perspective. Reviews of Geophysics, 55(2):310–340.
- He, M., Li, Q. and Li, X., 2020. Injection-induced seismic risk management using machine learning methodology—a perspective study. Frontiers in Earth Science, 8, p.227.
- Hills, J.M., 1984. Sedimentation, tectonism, and hydrocarbon generation in Delaware Basin, west Texas and southeastern New Mexico. AAPG bulletin, 68(3), pp.250-267.
- Horne, E.A., Hennings, P.H., Zahm, C.K., Callahan, O.A. and Eichhubl, P., 2021. Basement-rooted faults of the Delaware Basin and Central Basin Platform, Permian Basin, West Texas and southeastern New Mexico. The geologic basement of Texas: A volume in Honor of Peter T. Flawn, (286).
- Jaeger JC, Cook NGW, 1969. Fundamentals of rock mechanics. London: Methuen & Co. Ltd.
- Kim, J.W. and Lu, Z., 2018, Association between localized geohazards in West Texas and human activities, recognized by Sentinel-1A/B satellite radar imagery, Scientific reports, 8(1), 4727.
- Ward, R. F., Kendall, C. G. S. C., & Harris, P. M., 1986, Upper Permian (Guadalupian) facies and their association with hydrocarbons—Permian basin, west Texas and New Mexico. AAPG bulletin, 70(3), 239-262.

- Rubinstein, J.L. and Mahani, A.B., 2015. Myths and facts on wastewater injection, hydraulic fracturing, enhanced oil recovery, and induced seismicity. *Seismological Research Letters*, 86(4), pp.1060-1067.
- Scanlon, B.R., Reedy, R.C., Male, F. and Walsh, M., 2017. Water issues related to transitioning from conventional to unconventional oil production in the Permian Basin. *Environmental science & technology*, 51(18), pp.10903-10912.
- Sellards, E.H., Adkins, W.S., and Plummer, F.B., 1932, *The geology of Texas: Volume I Stratigraphy*, The University of Texas Bulletin 3232.
- Skoumal, R.J., Barbour, A.J., Brudzinski, M.R., Langenkamp, T. and Kaven, J.O., 2019, Induced seismicity in the Delaware Basin, Texas, *Journal of Geophysical Research: Solid Earth*.
- Skoumal, R. J., Barbour, A. J., Brudzinski, M. R., Langenkamp, T., and Kaven, J. O., 2020. Induced seismicity in the delaware basin, texas. *Journal of Geophysical Research: Solid Earth*, 125(1).
- Snee, J.E.L. and Zoback, M.D., 2018. State of stress in the Permian Basin, Texas and New Mexico: Implications for induced seismicity. *The Leading Edge*, 37(2), pp.127-134.
- Staniewicz, S., Chen, J., Lee, H., Olson, J., Savvaidis, A., Reedy, R., Breton, C., Rathje, E. and Hennings, P., 2020. InSAR reveals complex surface deformation patterns over an 80,000 km² oil-producing region in the Permian basin. *Geophysical Research Letters*, 47(21), p.e2020GL090151.
- Streit, J.E. and Hillis, R.R., 2004. Estimating fault stability and sustainable fluid pressures for underground storage of CO₂ in porous rock. *Energy*, 29(9-10), pp.1445-1456.
- Yeo, I.W., Brown, M.R.M., Ge, S. and Lee, K.K., 2020. Causal mechanism of injection-induced earthquakes through the Mw 5.5 Pohang earthquake case study. *Nature communications*, 11(1), p.2614.
- Zhai, G., Shirzaei, M. and Manga, M., 2021. Widespread deep seismicity in the Delaware Basin, Texas, is mainly driven by shallow wastewater injection. *Proceedings of the National Academy of Sciences*, 118(20), p.e2102338118.
- Zoback, M.D., 2010, *Reservoir Geomechanics* (Cambridge University Press, 2010).

CHAPTER 5

Effective depth detection: a case study of wastewater leakage

5.1 Introduction

Wastewater, also referred to as “produced water” or “oilfield brine”, is a byproduct of oil and gas production. Oil and gas are pumped out with wastewater and then separated by going through a separation phase or by treating with chemicals. The produced wastewater typically contains a large amount of sodium chloride as well as possibly toxic or radioactive chemicals depending on the rock formations being produced (Konkel, 2016). Small quantities of residual hydrocarbons and industrial substances used in the well construction could also be included in the wastewater. Therefore, wastewater should be safely treated to avoid air and/or surface pollution. Predominantly, it is injected into underground porous zones which should be sealed above and below by unbroken, impermeable rock layers following the safety regulations of the state and federal agencies. The injection zones should be sufficiently deep (the typical range is from 500 to 3,000 m in depth) in order to mitigate the contamination of shallow groundwater aquifers. However, approximately 5% of the oil-field related wastewater in the United States is discharged to the environment (Sirivedhin and Dallbauman, 2004), posing health risks, environmental contamination, and negative ecological impacts. There are many potential pathways for the wastewater to enter surface and groundwater, including spills from pipelines or tanker trucks transporting the wastewater, leakage and overflows from wastewater storage ponds, and upward migration of the fluids through the subsurface or failed injection well casings (Akob

et al., 2016). Unlike the visible spills at the surface, subsurface leakages are usually harder to detect. Mechanical integrity tests that examine internal and external mechanical components of the well function are required every five years to ensure there is no significant leak in the well according to the regulations of the U.S. Environmental Protection Agency (EPA). However, those infrequent tests could be augmented by alternative approaches such as in-situ fluid pressure measurements (Barbour et al., 2019) to monitor the underground processes to help detect the leakage as quickly as possible.

The Ken Regan field, located in northern Reeves County, West Texas within the Delaware Basin, produces hydrocarbons from the Delaware (Olds) sandstone of the upper Bell Canyon Formation (Hamilton, 1984), which overlies the Cherry Canyon and Brushy Canyon Formations successively. These three formations, deposited in the Guadalupian time of the Permian Period, comprise the Delaware Mountain Group, which contains more than 260 hydrocarbon reservoirs and has produced a large amount of oil and gas (Dutton et al., 2003; Nance, 2009). Then in Ochoan time, the sandstone and shale of the Delaware Group were covered by evaporites and limestone of the Castile Formation, which were in turn covered by evaporites interbedded with limestone, dolomite, sand, and shale of the Salado and Rustler Formations, which sealed and preserved the hydrocarbons. Partly dissolved dolomite, limestone, and gypsum of the Rustler Formation host the Rustler Aquifer (Mace et al., 2001) (Fig. 5.1). All deposition occurred in a marine environment until the Jurassic Period, after which the area was uplifted above sea level and underwent erosion and subaerial deposition, turning to the Delaware Basin. In Quaternary time, the climate became more arid, and deposition of silts, sands, and gravels from surrounding high areas, formed Cenozoic Alluvium, in which the water-bearing

sediments host the major unconfined aquifer in West Texas: the Pecos Valley Aquifer (Fig. 5.1a). The stratigraphy of the geologic settings is shown in Table 5.1.

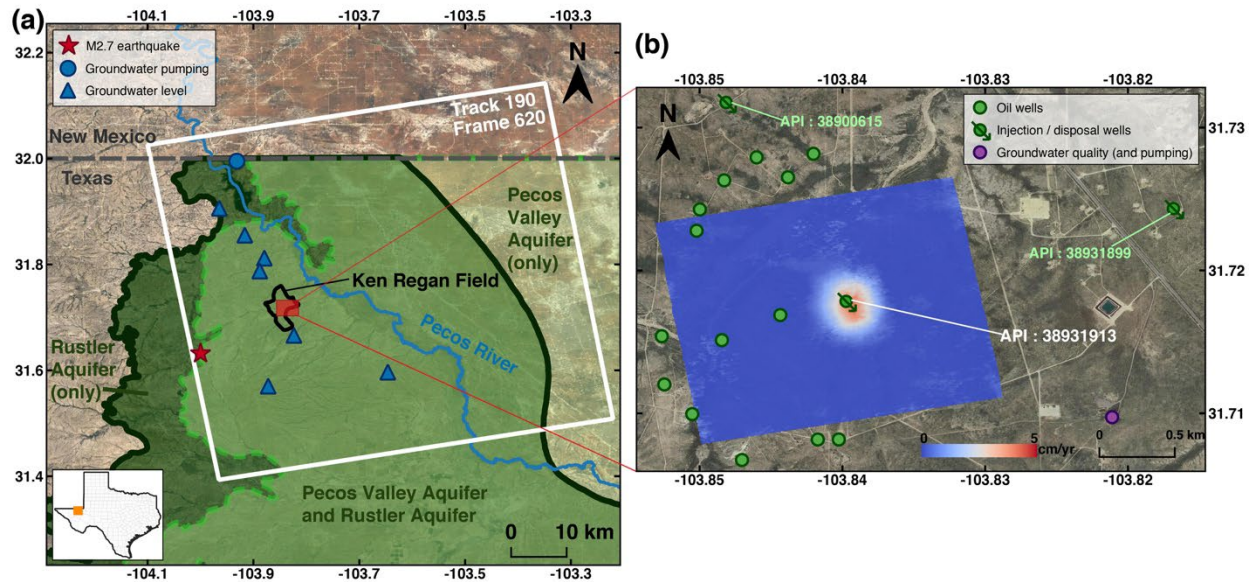


Figure 5.1 Study area of the case in Reeves county. (a) Coverage of the ALOS PALSAR scenes used (white box). Black line shows the boundary of the Ken Regan field. Dark green line and light green line represent the boundaries of the Rustler Aquifer (subcrop) and Pecos Valley Aquifer in Texas, respectively. Red star represents the epicenter of the M2.7 earthquake that occurred in May 2018. Blue circle represents the groundwater well for livestock drawing from the Rustler Aquifer in this area. Blue triangles are groundwater wells which provide groundwater leveling records. (b) Vertical deformation rate (cm/yr) (in a red box of Fig. 5.1a) estimated from InSAR. Green circles with and without arrows indicate active injection/disposal wells in the Ken Regan field and oil production wells within 1.5 km from the deformation center during the research period, respectively. Purple circle represents the groundwater well (state well no. 4618201) which provides groundwater quality records. The figures have been created using open-source software QGIS 3.6 available at <https://qgis.org/en/site/forusers/download.html>. The ALOS PALSAR data used in this study were downloaded through the Vertex online archive <https://vertex.daac.asf.alaska.edu> provided by Alaska Satellite Facility (ASF). The Landsat imagery used as background images of Fig. 1a and Fig. 1b were obtained from the EarthExplorer (EE) <https://earthexplorer.usgs.gov> provided by the United States Geological Survey (USGS).

Geologic layers	Depth (m)	Layers in three-layer model	Hydraulic conductivity (six-layer model)	Hydraulic conductivity (three-layer model)
Cenozoic Alluvium	0-50	Caprock	3×10^{-1} m/s	5×10^{-12} m/s
Rustler Formation	50-200		3×10^{-2} m/s	
Salado Formation	200-500		1×10^{-10} m/s	
Castile Formation	500-1020		5×10^{-12} m/s	
Bell Canyon	1020-1350	Injection Zone (Reported injection point: 1040 m)	1×10^{-6} m/s	1×10^{-6} m/s
Cherry Canyon	1350-1650			
Brushy Canyon	1650-2200	Base rock	5×10^{-9} m/s	5×10^{-9} m/s

Table 5.1 Stratigraphy of the study area.

The injection/disposal well American Petroleum Institute (API) No. 38931913 is located in the Ken Regan field (31.718° N 103.84° W). Originally completed for oil and gas production in 1989, by 1992, the well was granted a permit to dispose previously oil and gas produced wastewater by the Texas Railroad Commission (RRC), Texas' primary oil/gas-regulatory agency. In 2001, oil and gas production ceased and the well became a dedicated wastewater disposal well. Total oil and gas production from this well is more than 8,000 barrels and 100,000 thousand cubic feet (MCF), respectively. As a disposal well, it played an important role in the

Ken Regan field, undertaking 44% of the total injection volume in the whole field from 2007 to 2011. After 2015, the injection rate decreased greatly, accommodating only 0.6% of the total injection volume in the field. In 2017, the injection operations at the well were concluded. The depth of injection is reported to be 1,040 m (according to H-10 form provided by Texas RRC) where the Bell Canyon Formation lies (Table 5.1).

Generally, as the pore pressure builds up inside a deep wastewater injection zone, the pressure increases can propagate to other surrounding underground and overlying rock/soil layers, resulting in surface uplift (Chen, 2011). When basement faulting exists, the decrease of the effective normal stress on the adjacent faults can also increase the chances of failure and cause induced seismicity (Hornbach et al., 2016). However, there have been only a few ways to monitor the spatial pattern of the surface displacement caused by oil and gas activities in remote areas. In-situ methods to measure surface uplift in the well vicinity are labor-intensive, time-consuming, and sparsely distributed. Moreover, in many cases, it is challenging to pinpoint hydrocarbon production or wastewater injection wells that have experienced such surface displacement and are thus candidates for increased attention to ensure safe operation.

Interferometric Synthetic Aperture Radar (InSAR) is an effective tool for mapping ground deformation with centimeter-to-millimeter-level precision and meter-level resolution (Lu and Dzurisin, 2014). InSAR has been successfully used for monitoring surface deformation induced by wastewater injection and other oil field related fluid injection processes, and has proven its capacity to measure small to large induced deformation over localized to regional spatial scales (Yang et al., 2015; Kim and Lu, 2018; Loesch and Sagan, 2018). Both inverse elastic and forward poroelastic models have been constructed to simulate surface deformation induced by wastewater injection. Although elastic models may not be fully realistic and cannot

be applied to all geological settings, they can still provide insight into the subsurface geomechanical process (Samsonov et al., 2015). Poroelastic models are believed to more closely approximate reality and have performed well in many known cases (Yang et al., 2015). However, it is difficult to get precise hydro-geomechanical parameters of various geologic materials in the poroelastic models without obtaining samples from the subsurface or complete well logs. Poroelastic models are usually used to simulate the properties of the strata (Shirzaei et al., 2019) but are seldom used for analyzing unexpected underground processes such as wastewater leakage and subsurface fluid migration.

In this chapter, we used data acquired by the Advanced Land Observation Satellite (ALOS) Phased Array type L-band Synthetic Aperture Radar (PALSAR) from 2007 to 2011 to generate InSAR images and analyze the time series deformation induced by wastewater disposal at the API No. 38931913 well. Elastic Mogi (1958) and Okada (1985) models were utilized to provide the initial estimates of geomechanical processes that were further analyzed using three-dimensional, finite element based, poroelastic models via Defmod (Ali, 2014). Initially, six-layer models (Cenozoic Alluvium - Rustler Formation - Salado Formation - Castile Formation - injection zone - base rock) were employed to test and refine the local hydrologic properties. With the displacement-driven refinement, we next used a three-layer model (caprock - injection zone - base rock) to investigate the underlying geomechanical processes, which could provide information about undesired subsurface processes such as wastewater leakage and fluid migration.

5.2 Method

5.2.1 InSAR processing

ALOS PALSAR data are used to detect ground deformation in the Ken Regan field. The area covered with sparse, short vegetation is more likely to be coherent using L-band data. 14 images (ascending track: 190, frame: 620) from January 18, 2007 to March 16, 2011 were acquired to generate interferograms. We have applied 1×2 multilook window to maintain high resolution and coherence. Adaptive spatio-temporal filtering has been applied to suppress noise components related to atmospheric artifacts. Because we have SAR datasets from an ascending track only, we cannot retrieve both the horizontal (east-west) and the vertical deformation. However, the observed line-of-sight (LOS) deformation is dominated by the vertical deformation in the wastewater disposal well of the Delaware Basin (Kim and Lu, 2018). We therefore convert LOS to the vertical deformation. The vertical displacement d_{ver} can be calculated as:

$$d_{ver} = d_{LOS} / \cos \theta \quad (5.1)$$

where d_{LOS} is the LOS displacement and θ is the incidence angle. The lack of descending track data makes the horizontal displacement unavailable, causing uncertainties in the above conversion. It has been shown that the horizontal deformation is less than $\sim 20\%$ of the vertical deformation in wastewater injection cases in the region (Kim and Lu, 2018).

We remove the topographic effects using 1-arcsec digital elevation model (DEM) data from the shuttle radar topography mission (SRTM) (Jarvis et al., 2008). After removing topographic effects, 31 interferograms with high coherence (>0.4) were chosen for the time-series analysis using the Small Baseline Subset (SBAS) technique (Berardino et al., 2002). By minimizing the temporal and spatial baseline between the acquisitions required for applying the SBAS method, decorrelation artifacts can be further mitigated. The abundant multi-temporal

InSAR observations over a small area (2×1.7 km) help separate signatures of deformation and atmospheric effects with the aid of spatio-temporal filtering.

5.2.2 Inverse elastic models

We used Mogi modeling (Mogi, 1958) to simulate the surface deformation maps and estimate the corresponding injection volume and depth. This technique models the deformation from a point source in an elastic half-space, which is widely applicable in geophysical studies (Lu and Dzurisin, 2010) and has been used for modeling deformation caused by fluid injection (Samsonov et al., 2015). Displacement induced by wastewater injection can be calculated according to Eq. 5.2:

$$\begin{pmatrix} u_x \\ u_y \\ u_z \end{pmatrix} = \Delta V \frac{(1 - \nu)}{\pi R^3} \begin{pmatrix} x \\ y \\ d \end{pmatrix} \quad (5.2)$$

$$R = \sqrt{x^2 + y^2 + d^2}$$

Where x and y are the distance in the x and y directions from the point to the injection well, d is the injection depth, u_x , u_y , u_z are the displacements in the x , y , and z directions, ΔV is the injection volume, ν is the Poisson's ratio, and R is the radial distance (distance between the source and the point whose coordinates are x and y at the surface). We determined the best-fit models and parameters by searching over the range of the parameters and minimizing the root mean square of the residuals.

In addition to the Mogi modeling, a horizontal Okada model (Okada, 1985) with uniform opening in an elastic half-space, was also applied for the estimation of the injection depth. Okada models are usually used as the source model for earthquakes (Wright et al., 2003) and volcanoes and have been used for wastewater injection (Kim and Lu, 2018).

5.3.3 Forward poroelastic model

Defmod (Ali, 2014), an open-source finite element code for modeling crustal deformation, was benchmarked and validated by Meng (2017) and has been successfully used to model earthquakes induced by fluid withdrawal and/or injection (Meng, 2018), and to investigate deformation in a geothermal field (Ali et al., 2018). In this study, we used the poroelastic module of Defmod to model the surface uplift due to wastewater injection. Trelis™ was used to generate the mesh files required by Defmod. For each 3D model, more than 100,000 tetrahedral elements were generated in the mesh file; the surface area is $3 \text{ km} \times 3 \text{ km}$. The mesh file was plugged into Defmod to solve the coupled system of the momentum equation and the continuity equation in the discretized form:

$$\begin{aligned} K_e u - H p &= f \\ H^T \dot{u} + S \dot{p} + K_c p &= q \end{aligned} \quad (5.3)$$

where K_e and K_c are solid and fluid stiffness matrices; H is the coupling matrix; S is the compressibility matrix; u is the displacement field; p is the pressure field; f is the body force and q is the in/out flow.

The well log of the API No. 38931913 well only covers part of the Bell Canyon Formation, so properties (depth, Young's modulus, Poisson's ratio, hydraulic conductivity, etc.) of the underground layers are obtained from previous research (Beauheim and Holt, 1990; National Research Council, 1984; Richey et al., 1985; Meyer et al., 2012; Ewing et al., 2012) and adjacent well logs (Borns and Shaffer, 1985; Karacan, 2009; Al-Kattan and Al-Ameri, 2012). As the Brushy Canyon is generally less permeable than the other two formations in the Delaware Mountain Group, we classified the Bell Canyon and Cherry Canyon both as injection zone and the Brushy Canyon as base rock. Although the Rustler Formation and Cenozoic Alluvium are comparatively permeable, we hypothesize that the hydraulic conductivities of these

two formations in the vicinity are locally low; this restriction is derived from InSAR results and poroelastic models (discussed in 5.4.1). Thus, we consider all formations above Bell Canyon as caprock (Table 5.1).

5.3 Results

5.3.1 InSAR time series analysis

InSAR processing was used to generate time series deformation maps from January 18, 2007 to March 16, 2011 (Fig. 5.2). We have detected an area of persistent uplift (Fig. 5.2). The uplift occupies an area with a radius of 250 m, which is relatively localized compared with other km-sized fluid injection induced deformation (Yang et al., 2015; Kim and Lu, 2018; Loesch and Sagan, 2018; Samsonov et al., 2015). The cumulative vertical deformation reaches nearly 17 cm during 2007-2011. However, the study area has been seismically quiet according to USGS and TexNet earthquake catalogs; the epicenter of the nearest earthquake, a M2.7 event that occurred in 2018, is more than 10 km away from this area (red star in Fig. 5.1a). These comparatively long distances suggest they are irrelevant to the observed small-radius uplift. Only one wastewater disposal well (API No. 38931913) is located within the uplift area, and other injection/disposal wells active during the research period are distributed about 2 km away from the deformation center (Fig. 5.1b). There are active oil production wells within a distance of 1.5 km (Fig. 5.1b), but the total production volume of all 14 wells is less than 1% of the injection volume in the wastewater disposal well. Thus, we focus our attention on the correlation between the uplift and the wastewater injection at API No. 38931913 well.

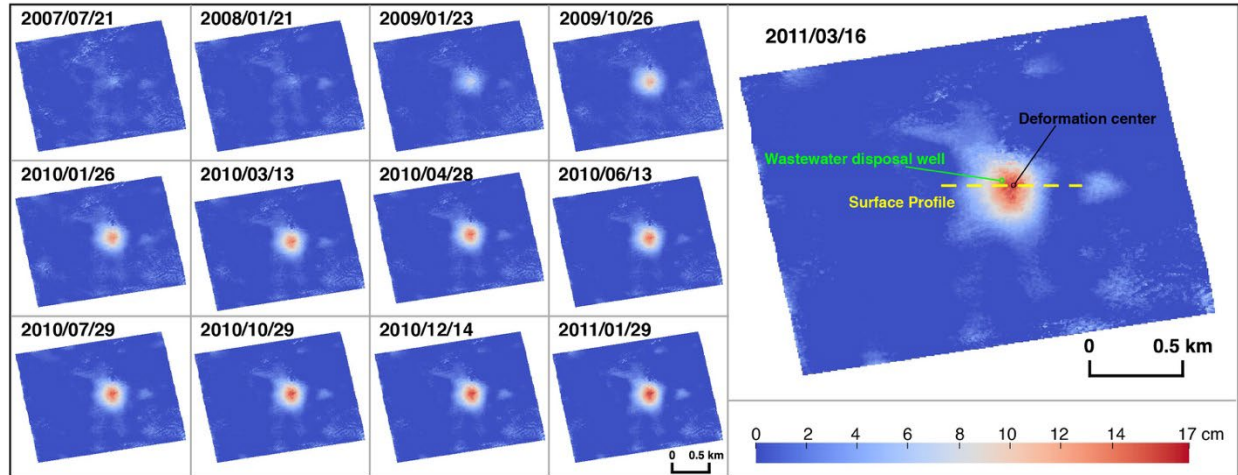


Figure 5.2 Time series cumulative vertical deformation maps from 2007/01/18 to 2011/03/16 over the study area. The reference image in 2007/01/18 is omitted. Green circle represents the API No. 38931913 wastewater disposal well. Black circle represents the deformation center. Yellow dash line shows the surface profile of the total vertical deformation plotted in Figure 5.5(d).

The deformation center lies ~ 70 m southeast of the disposal well. Most vertical wells are tilted and the pressurized wastewater injection can be conducted distant from an actual surface wellbore location. The southeastward offset between the deformation center and the disposal well also implies the direction of the groundwater flow. Due to the lack of groundwater stations in the study area, it is difficult to determine the direction of local groundwater flow within different layers of aquifer systems. Sharp (2001) suggested a probable southeastward direction of the nearby regional flow system (Salt Basin - Toyah Basin - Pecos River system), consistent with our observation. Groundwater level measurements at wells in the Pecos Valley Aquifer provided by the Texas Water Development Board (TWDB) also indicate a southward direction along with an eastward component (Fig. 5.1a). However, the local flow direction within the Rustler Aquifer in the Delaware Basin can be affected by variations in the potentiometric surface resulting from

oil-related production activities (e.g., water production) as well as local features produced by evaporite dissolution and collapse.

The cumulative peak vertical displacement is highly correlated with the cumulative injection volume from January 2007 to early 2011 (Fig. 5.3). Both the displacement rate and the injection volume rate decreased after March 2010, suggesting the displacement responded almost instantaneously (within the ALOS repeat cycle 46 days and 1-month interval of the injection data) to the wastewater injection. Assuming the displacement is zero when the injection starts, the cumulative vertical displacement and cumulative injection volume show high correlation in the linear fitting (inset of Fig. 5.3). The ratio between injection volume (10^4 m^3) and vertical displacement (cm) is 2.24 with an R-squared value of 97.5%. The high correlation indicates the ground surface was heaving due to the wastewater injection in the No. 38931913 disposal well. The Sentinel-1A/B images acquired over this region have not been able to detect any deformation during 2015-2019 when the injection decreased the rate and finally ceased, further supporting the conclusion that the ground uplift was caused by wastewater injection.

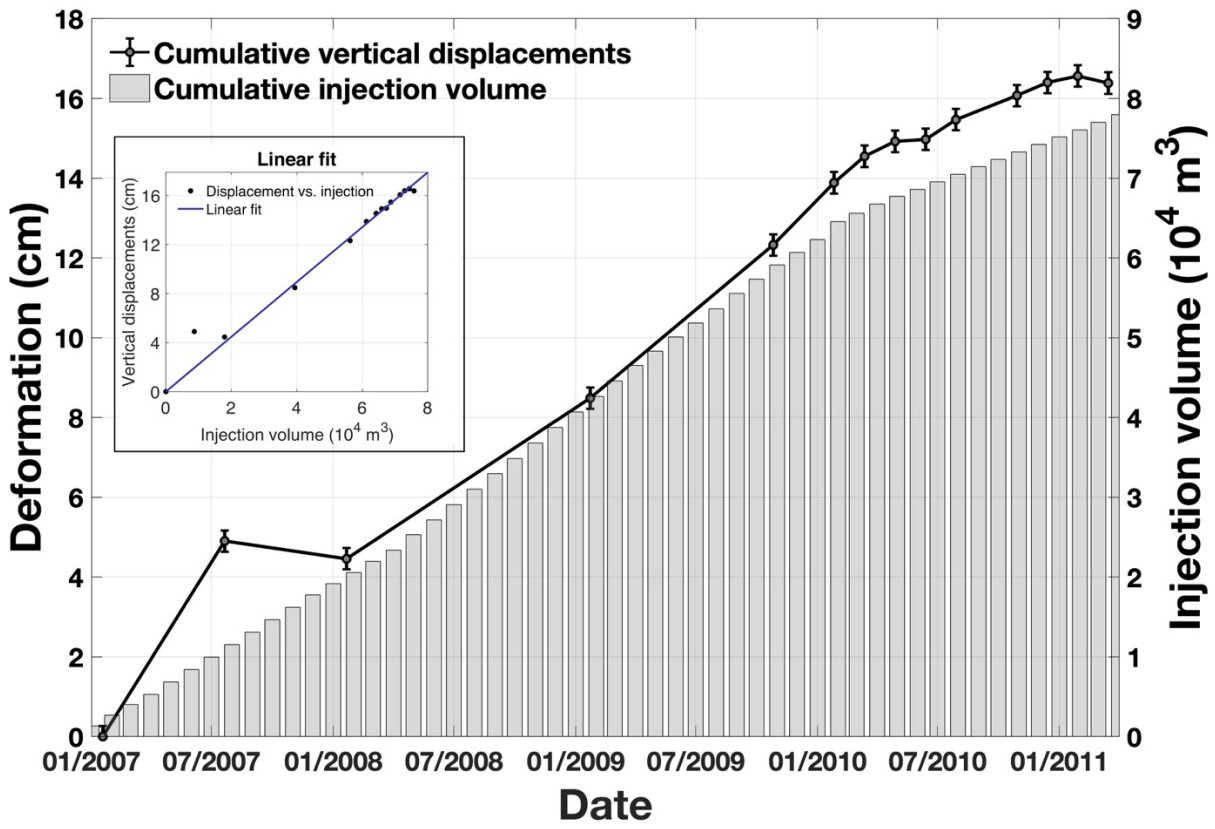


Figure 5.3 Comparison of the cumulative wastewater injection volume (gray bars) and time-series cumulative vertical deformation at the deformation center (black line). The error bars show uncertainties obtained in the time-series analysis. Linear fitting of the cumulative vertical deformation and the cumulative wastewater injection volume assuming the displacement is zero when the injection starts (inset).

5.3.2 Inverse elastic models

Due to the instantaneous and linear response between the fluid injection and displacement, the elastic models are expected to be reasonable for estimating the parameters related to geomechanical processes in the injection zone and surrounding strata despite some limitations (Samsonov et al., 2015). As inverse Mogi models are easy to implement, they were constructed to simulate the time series deformation observed by InSAR and estimate the

effective injection depth and volume. The Mogi model to calculate an analytical solution for surface deformation due to a point source in an elastic half space performs well (Fig. 5.4) with a root mean square error (RMSE) of 1.46 cm, but the total effective injection volume derived from the Mogi model is only 27% of the reported injection volume. And notably, the modeled effective average injection depth was only 177 m, which is much shallower than the reported injection depth of 1,040 m. Okada models were also utilized to model the deformation and check the parameters from the Mogi model. The total effective injection volume at the rectangular dislocation source (217×343 m) was just 21% of the reported injection volume. The effective injection depth derived from the Okada model averages 186 m, again much shallower than the reported injection depth.

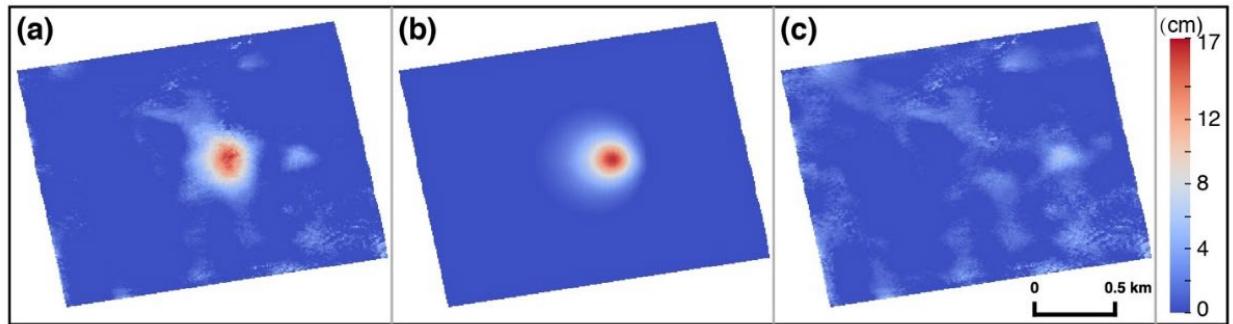


Figure 5.4 Mogi model of cumulative vertical deformation from 2007/01/18 to 2011/03/16. (a) Observation, (b) simulated deformation, and (c) residual.

5.3.3 Forward poroelastic models

Finite element models were applied to model the total deformation map (2007/01/18 – 2011/03/16) by taking into account the poroelastic effects in the pressure and displacement fields. With the refinement of the six-layer models (Cenozoic Alluvium - Rustler Formation -

Salado Formation - Castile Formation - injection zone - base rock) based on observed displacement (see Discussion 5.4.1), a three-layer (caprock - injection zone - base rock) poroelastic model with reported injection volume and reported depth was utilized to simulate the total surface deformation (Fig. 5.5a). The profile of the surface vertical displacement in comparison with the profile of the observation is shown in Fig. 5.5d. The deformation simulated based on the reported injection information (injection depth: 1,040 m) is broader and its magnitude is smaller (blue line in Fig. 5.5d) than our InSAR observation (black circles in Fig. 5.5d), indicating that the underlying geo-mechanical process cannot be simply interpreted by the reported injection depth and volume. The huge difference between the simulation and the observation makes it difficult to find the best solution of effective volume and depth taken the reported injection information as the first step. To avoid time-consuming computation in the iterative scheme of finite element models, we need better initial estimates of the solution, which could be provided by the elastic models. We thus simulate the poroelastic deformation using source parameters from the Mogi (injection depth: 176 m). As the Mogi-derived depth is within the caprock, we modeled a one-layer (caprock only) poroelastic scenario for simplicity (Fig. 5.5b). The spatial size of the poroelastic-modeled uplift is similar to the Mogi-derived deformation (green line in Fig. 5.5d) but its magnitude is smaller, which is consistent with the comparison of elastic and poroelastic models by Samsonov (2015). In order to further refine this solution and obtain a best-fit model, we tried a range of effective injection depth and volume in both the three-layer and one-layer models. The best-fit parameters are found in the one-layer model with an effective injection volume of $4.4 \times 10^4 \text{ m}^3$ (57% of the reported injection volume) and an effective injection depth of 130 m, even shallower than the depth derived from the inverse elastic models (Fig. 5.5c and 5.5d).

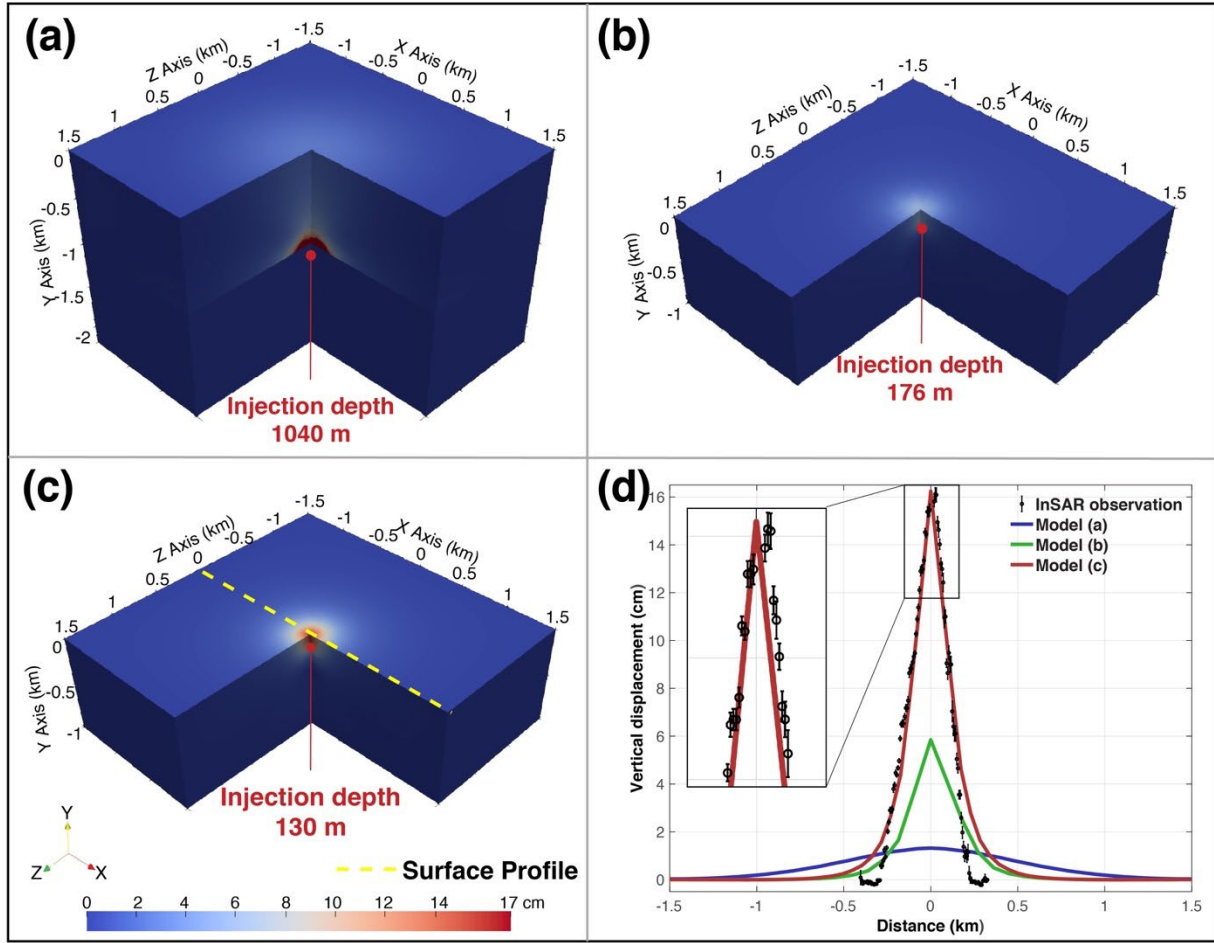


Figure 5.5 Final displacement fields and surface profiles of the forward poroelastic models. Orientation axes show the optic angle of the deformation field. Red dots represent the injection depths. Yellow dashed line shows the surface profile plotted in (d). (a) Three-layer model using reported injection depth and volume. (b) One-layer (caprock) model using Mogi-derived depth and volume. (c) Best-fit model derived by poroelastic modeling. (d) Comparison of vertical displacement surface profiles of InSAR observation and the poroelastic models. The error bars of the InSAR observation show uncertainties obtained in the time-series analysis. The upper part of the comparison is enlarged in the inset.

The shallow effective injection depth derived from both inverse elastic models and forward poroelastic models suggests that part of the injected wastewater somehow leaked into a

shallower aquifer in the caprock and induced localized surface uplift, while the remaining wastewater may have diffused away in the injection zone or other strata.

5.4 Discussion

5.4.1 Insights into local hydrologic properties

The hydraulic conductivities of the Rustler Formation and Cenozoic Alluvium are generally high ($> 10^{-6}$ m/s). We have analyzed multiple six-layer (Cenozoic Alluvium - Rustler Formation - Salado Formation - Castile Formation - injection zone - base rock) poroelastic models with varying injection depths and volumes, but none generated an area of uplift as localized as the observation, and the magnitude of uplift fail to reach even 10 cm (versus the ~17 cm observed). There are five hydrologic units in the Rustler Formation with 11 hydro-stratigraphic divisions (Beauheim and Holt, 1990). Theoretically, we can refine the model with those divisions to seek solutions for the uplift. However, due to the lack of information in the well log, the local stratigraphy cannot be described with an accuracy of 10-meter level. The failure in generating localized deformation is reasonable because high hydraulic conductivities render rapidly spreading fluid (or pore pressure). The pressure change cannot be accumulated, thus no obvious surface deformation can be induced. A confined aquifer somehow existing within the Rustler Formation and/or Cenozoic Alluvium could help confine the wastewater, but it is difficult to explain how the fluid flows into, but not out of, the aquifer. Besides, the confined aquifer would behave similarly to locally impermeable material in terms of induced deformation. Therefore, we make the refinement of the local hydrologic properties assuming that the Rustler Formation and Cenozoic Alluvium are locally impermeable and perform as caprock.

We assume the uplift area is a circle for the simulation, and thus the hydrologic properties of the strata can be considered isotropic. However, the trend of the surface profile on the east side of the deformation center is slightly larger than the west side, which indicates the local lateral properties could be slightly anisotropic. Anisotropic lateral properties would be consistent with the observed center of the deformation offset from the wastewater disposal well.

5.4.2 Poroelastic models based on the reported injection depth

When constructing wells, low permeable substances, such as drilling mud that is used to aid the drilling of boreholes, could also be injected to depth. A possible mechanism for a localized surface uplift with deep injection is that a confined aquifer in the injection zone was formed by a surrounding layer of impermeable material and the injection coincidentally occurs in the confined aquifer which prevents the wastewater from diffusing away. To evaluate this theory, we added a 10 m wide impermeable material into the injection zone in the three-layer poroelastic model to simulate a confined aquifer (Fig. 5.6a). The output of reported injection depth and volume in Fig. 5.6b shows a broader and significantly smaller uplift. Different shapes of the confined aquifer were simulated but none of them performs as well as expected. The non-localized deformation in these cases further proves that the effective injection depth should be shallower than the reported depth.

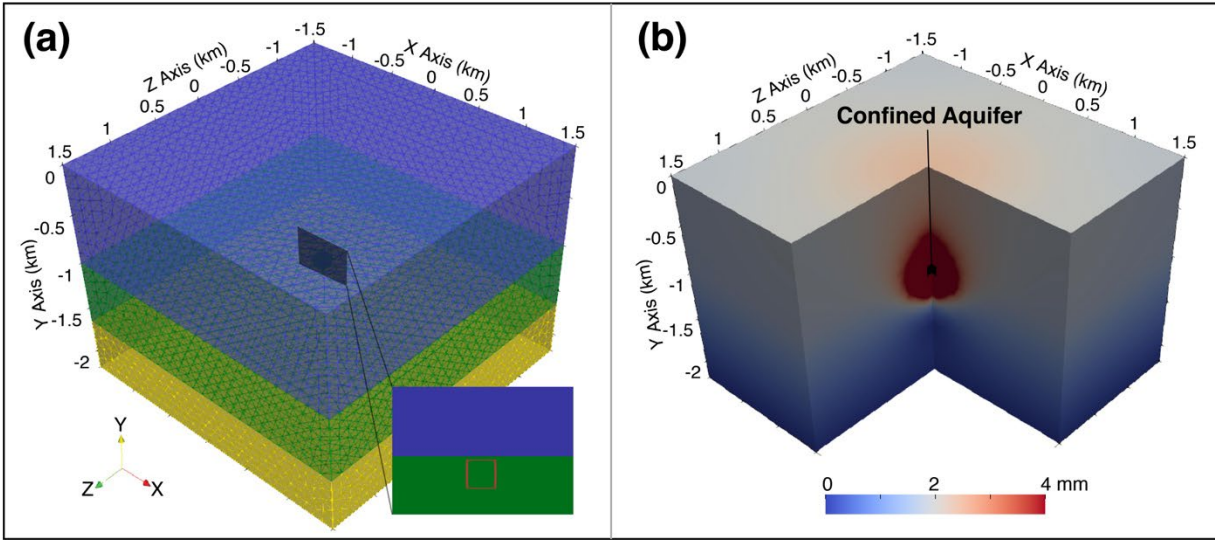


Figure 5.6 Three-layer poroelastic model with a confined aquifer. (a) Geometry and mesh of the finite element model. Blue, green and yellow brick represent the caprock, injection zone, and the base rock, respectively. Enlarged rectangle shows the location of the surrounding impermeable material (red square), inside of which is a confined aquifer. Orientation axes show the optic angle of the deformation field. (b) The final displacement field of (a) using reported depth and volume. The black shape shows the location of the confined aquifer.

5.4.3 Possible causes of the shallow effective injection depth

According to the results of the best-fit poroelastic model, 57% of the reported injection volume leaks to the effective injection depth 130 m (in the range of Rustler Aquifer), inducing the localized surface uplift. The remaining 43% of the wastewater could diffuse away in the reported injection zone or other strata, causing negligible far-field deformation. Possible causes of the leakage (Fig. 5.7) could include: failure in the production casing, sealing problem, and fluid migration through the subsurface fractures (Gómez, 2014).

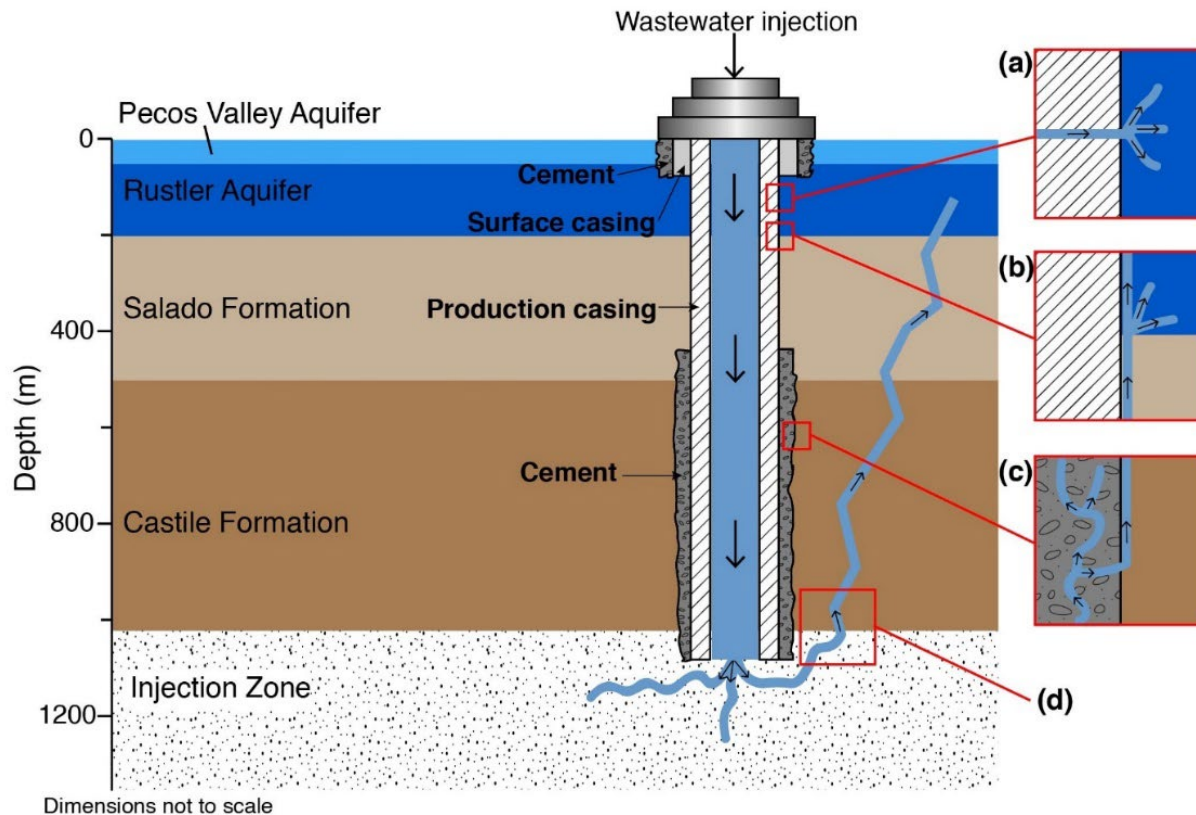


Figure 5.7 Stratigraphy, well completion, and possible pathways for upward migration of wastewater. Possible leakage caused by (a) failed production casing, (b) sealing problem - through the space between the casing and the wellbore, (c) sealing problem - through vertical channel in the faulty cement, and (d) fault and fracture systems. The figure has been created using university-licensed Adobe Illustrator.

5.4.3.1 Failed production casing

The surface casing and the surrounding cement, built for protecting the underground source of drinking water - the Pecos Valley Aquifer (Fig. 5.7), is reported to extend to 77 m deep according to the casing records of the API No. 38931913 wastewater disposal well. The production casing along with surface casing and sealing cement in the 0-77 m deep are less likely to fail, but in the effective injection depth of 130 m, the production casing (typically made from

carbon steel) and the inside tubing (ideally corrosion-resistant material) are subject to a corrosion accelerated by chemicals (e.g., Hydrogen Sulfide) present in both the Rustler Formation and the injected wastewater. In 2007, the well was about 20 years old. Even a well originally constructed within safety parameters from materials that passed mechanical integrity tests could possibly experience later leakage due to a casing failure including corrosion, axial cracking, and joint/coupling problems.

A direct conjecture is that the production casing failed at the effective injection depth of 130 m allowing 57% of the wastewater to flow out at this failed section (Fig. 5.7a). The failed section does not need to be a complete mechanical failure, which would allow all the wastewater to leak at the effective injection depth. Instead, small cracks (or holes in corroded pipes) are sufficient, which is a more likely scenario. With high pressure during the injection and small perforations in the production casing, the remaining 43% of the wastewater could flow down through the wellbore and diffuse away into the reported injection zone. In this case, the relationship between displacement rate and cumulative injection volume rate may not be linear but more complicated, with (at least) both the pressure and the area of failed wellbore section considered as important factors.

5.4.3.2 Sealing problems

Sealing problems may be caused by voids between production casing/cement and surrounding sediments (Fig. 5.7b). In this case, the wastewater flows up from the reported injection zone along the wellbore either until the deepest permeable aquifer, into which the wastewater will diffuse, or until the void disappears. Considering the deepest permeable aquifer assumption, if we ignore the hypothesis for the model that the Rustler Formation is impermeable,

then the wastewater will accumulate in the Rustler Formation as it is the first permeable aquifer (Fig. 5.7b). Nevertheless, the lowest layer inside the Rustler Formation is a permeable aquifer, not a confining bed, indicating the effective depth would be 200 m but not 130 m. It is coincident that the effective injection depth from the Okada model is ~200 m but that is meaningless because if so, the wastewater will diffuse rapidly at that aquifer and not induce a localized surface uplift. Thus, the upward migration of wastewater is less possibly to end at the deepest permeable aquifer, the sealing problem can explain the shallow effective injection depth only if the voids between production casing/cement and surrounding sediments appear from 130 m depth to deeper.

The bottom part of the production casing is sealed by cement (Fig. 5.7). If the seal worsens over time or the well has not been sealed properly, after the wastewater is disposed into the injection zone, it may flow up along the vertical channel in the faulty cement (Fig. 5.7c). The flowing-up wastewater could either gather in the top of the cement or flow out into any part of the cement and then flow up along the voids between the cement and the surrounding sediments if possible. It will not diffuse in the formations because the Salado and the Castile Formations are not permeable aquifers comparatively. However, the top of the cement to protect the bottom casing is reported to be 445 m, deeper than the effective depth, indicating a sealing problem in the cement cannot solely explain the leakage, but could perhaps provide an additional pathway for upward fluid migration in the bottom part of the well.

Leakage due to sealing problems can only be explained by the hypothesis that voids between the production casing and surrounding sediments occur from 130-445 m combined with faulty cement and/or voids between cement and surrounding sediments present from 445 m to

the reported injection zone, providing continuous pathways for wastewater to flow up from the reported depth to the effective injection depth.

5.4.3.3 Subsurface fractures

Plenty of fault and fracture systems are located underlying the Delaware Basin, and have been thought to bring hydrologic communication between different layers of aquifer systems (Anderson, 1981). These fractures may provide pathways for the upward migration of wastewater (Fig. 5.7d). To link the reported injection zone and the effective injection depth, we added a tube of high permeability material with a radius of 10 m as a path simulating the fracture into the three-layer poroelastic model (Fig. 5.8a). The inclination of the tube is positioned to model the 70 m distance between the deformation center and the wastewater disposal well. We also assume that there is a high permeability confined aquifer (a sphere with a radius 20 m) at the effective injection depth to increase the attraction for the wastewater. However, the output displacement field in Fig. 5.8b indicates that the 20 m wide path still cannot draw as much wastewater as we expected (or the pore pressure change cannot accumulate to what we expected) if no other forces are added, while the fractures, in reality, should be much narrower than 20 m. Thus, leakage due to subsurface fractures cannot be the main cause of the localized uplift.

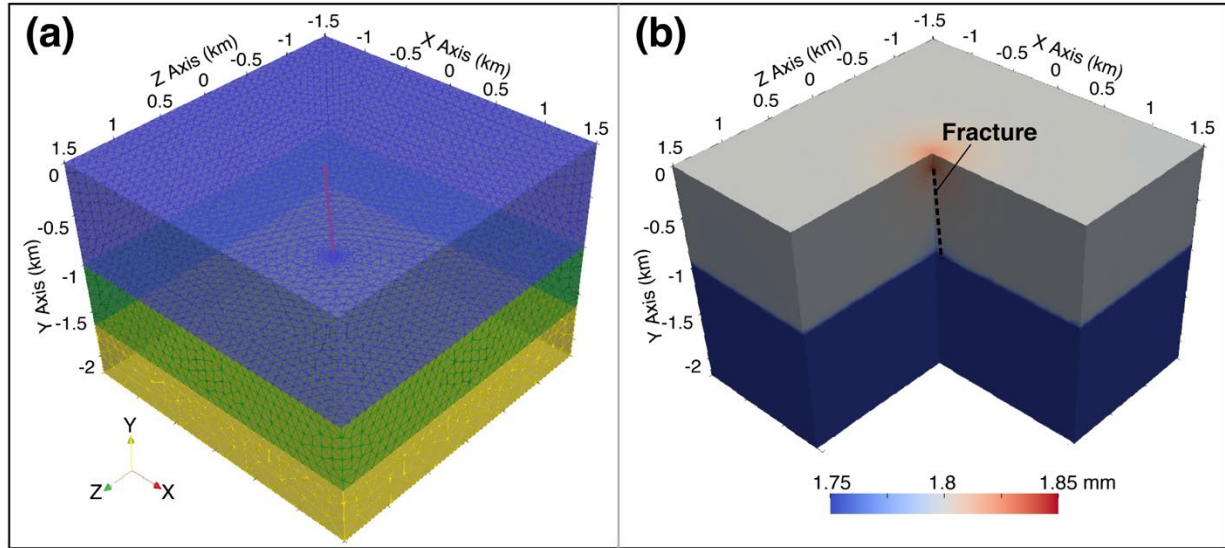


Figure 5.8 Three-layer poroelastic model with a fracture. **(a)** Geometry and mesh of the finite element model. Blue, green and yellow brick represent the caprock, injection zone, and the base rock, respectively. Red inclined cylinder (10 m radius) and the sphere (20 m radius) at the top of the cylinder represent the highly permeable pathway (the fracture) and the confined aquifer, respectively. Orientation axes show the optic angle of the deformation field. **(b)** The final displacement field of (a) using reported depth and volume. Black dashed line shows the location of the fracture.

Other limitations of this explanation include the following. (1) If the injection completes, previously accumulated wastewater in the upward confined aquifer will spread back into the injection zone via the same fracture(s) as the hydraulic conductivities of the fracture and injection zone are higher than the surrounding caprock. If so, we should see subsidence over time, which has not been observed so far. (2) Generally, the actual fractures are distributed irregularly and randomly, which cannot induce the very circular surface uplift as observed.

Possible reasons for the leakage are therefore concluded to be failed production casing, sealing problem(s), or the combination effect of these two, while the leakage along subsurface fractures and resulting uplift are less plausible.

5.4.4 Impacts of the leakage

The effective injection depth of 130 m is inside the Rustler Aquifer. The Rustler Aquifer is only used for irrigation and livestock and not municipal and domestic supply due to high concentrations of dissolved solids (Reeves County Groundwater Conservation District, 2018). Although the drinking water may not be directly impacted, the possible leakage can pose risks to crops and livestock. There is only one single groundwater well pumping for livestock in this area from the Rustler Aquifer (blue circle in Fig. 5.1a). However, some groundwater from the Rustler Formation does eventually discharge into the Pecos River (Mercer, 1983). Upward leakage into the overlying strata could also happen (Alexander et al., 1964), impacting water quality in the overlying aquifers. Besides, the fault and fracture systems provide pathways for rapid water migration.

Due to the void of groundwater wells into the Rustler Aquifer in the vicinity, we cannot check the nearby water quality in the Rustler Formation. However, the groundwater quality in the Pecos Valley Aquifer can reflect conditions in the Rustler Aquifer to some extent as a result of upward water migration. We compared the groundwater quality records from the nearest groundwater well into the Pecos Valley Aquifer (state well no. 461820, 31.71° N 103.821° W, the purple circle in Fig. 5.1b) with the cumulative wastewater injection volume. Fig. 5.9 shows an increase of dissolved sodium in the Pecos Valley Aquifer. The dissolved sodium increased 13 mg/L during 2007-2011 and 5 mg/L during 2011-2018, which could be related to wastewater injection. The wastewater injection rate was high from 2007 to 2011; the corresponding growth rate of dissolved sodium was also comparatively large (3.25 mg/(L·yr)). When the wastewater injection rate decreased after 2011, the growth rate of dissolved sodium also decreased (0.71 mg/(L·yr)). The similar trend of the dissolved sodium in the Pecos Aquifer and the cumulative

injection volume suggests that the wastewater injection may influence the groundwater quality in the Pecos Valley Aquifer. As this well is used for livestock and the pumping has not been concluded, this reduced level of groundwater quality is still within acceptable parameters. The possible leakage of toxic fluids can bring health risks, environmental contamination, and negative ecological effects. As we have not observed clear subsidence since the injection operations concluded with Sentinel-1 results, the wastewater seems to disperse slowly, reducing the risk to some extent.

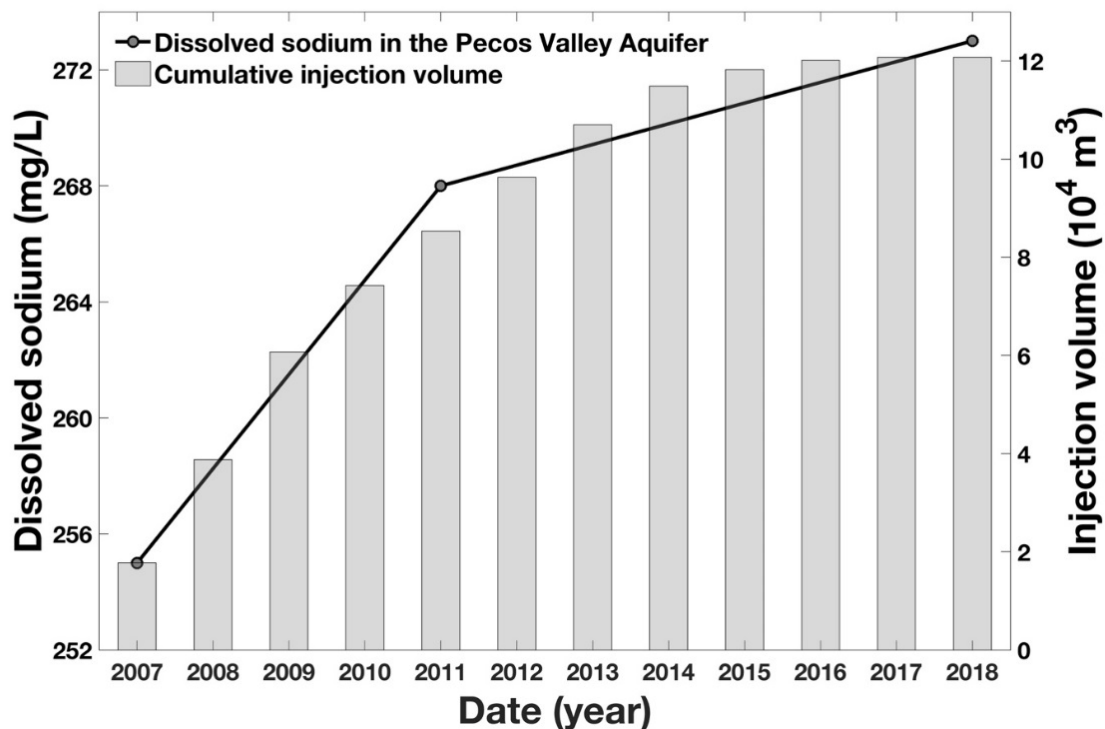


Figure 5.9 Comparison of the cumulative wastewater injection volume (gray bars) and the dissolved sodium in the Pecos Valley Aquifer (black line).

5.5 Conclusion

In our study, InSAR has shown the capability to measure a localized surface displacement related to fluid injection. The surface uplift near the wastewater disposal well (API NO. 38931913) in the Ken Regan field is caused by wastewater disposal in this well. The inverse elastic Mogi model performs well to roughly estimate the effective injection depth and volume from the measured InSAR deformation. Defmod is effective in investigating the poroelastic subsurface processes. The combination of InSAR results and poroelastic models generated by Defmod gives a clue about hydrologic properties of the strata. The modeled effective injection depth (130 m) of this well is much shallower than the reported injection depth (1,040 m). A reasonable explanation is that the well has experienced leakage due to a failed production casing and/or sealing problem(s). Leakage into the Rustler Aquifer poses some risk, but maybe not be serious when the wastewater disperses slowly away as is believed to be the case. Our analysis that exploits InSAR observation and numerical models provides an indirect leakage monitoring technique to supplement current infrequent leakage detection methods.

Reference

- Akob, D. M. *et al.* Wastewater disposal from unconventional oil and gas development degrades stream quality at a West Virginia injection facility. *Environ. Sci. Technol.* **50**, 5517–5525 (2016).
- Al-Kattan, W. & Al-Ameri, N. J. Estimation of the rock mechanical properties using conventional log data in North Rumaila field. *Iraqi J. Chem. Pet. Eng.* **13**, 27–33 (2012).
- Alexander, W. H., Myers, B. N. & Dale, O. C. *Reconnaissance Investigations of the Ground Water Resources of the Guadalupe, San Antonio, and Nueces River Basins, Texas*. (U.S. Geological Survey and Texas Water Commission, 1964).
- Ali, S. T. Defmod - Parallel multiphysics finite element code for modeling crustal deformation during the earthquake/rifting cycle. Preprint at <http://arxiv.org/abs/1402.0429> (2014).
- Ali, S. T. *et al.* Geodetic measurements and numerical models of transient deformation at Raft River geothermal field, Idaho, USA. *Geothermics* **74**, 106–111 (2018).
- Anderson, R. Y. Deep-seated salt dissolution in the Delaware basin, Texas and New Mexico. in *Environmental Geology and Hydrology in New Mexico* 131–145 (New Mexico Geological Society, 1981).
- Barbour, A. J., Xue, L., Roeloffs, E. & Rubinstein, J. L. Leakage and increasing fluid pressure detected in Oklahoma’s wastewater disposal reservoir. *J. Geophys. Res. Solid Earth* [10.1029/2019JB017327](https://doi.org/10.1029/2019JB017327) (2019).
- Beauheim, R. L. & Holt, R. M. Hydrogeology of the WIPP Site. in *Geological and Hydrological Studies of Evaporites in the Northern Delaware Basin for the Waste Isolation Pilot Plant (WIPP), New Mexico, Geological Society of America 1990 Annual Meet Field Trip 14 Guidebook* 131–179 (The Dallas Geological Society, 1990).
- Berardino, P., Fornaro, G., Lanari, R. & Sansosti, E. A new algorithm for surface deformation monitoring based on small baseline differential SAR interferograms. *IEEE Trans. Geosci. Remote Sens.* **40**, 2375–2383 (2002).
- Borns, D. J. & Shaffer, S.-E. *Regional Well-log Correlation in the New Mexico Portion of the Delaware Basin*. (Sandia National Laboratories, 1985).
- Chen, Z. R. Poroelastic model for induced stresses and deformations in hydrocarbon and geothermal reservoirs. *J. Petrol. Sci. Eng.* **80**, 41–52 (2011).
- Dutton, S. P., Flanders, W. A. & Barton, M. D. Reservoir characterization of a Permian deep-water sandstone, East Ford field, Delaware basin, Texas. *AAPG Bulletin* **87**, 609–627 (2003).

- Ewing, J. E. *et al.* *Final Groundwater Availability Model Report for the Rustler Aquifer*. (Texas Water Development Board, 2012).
- Gómez, J. A. *Drinking Water: EPA Program to Protect Underground Sources from Injection of Fluids Associated with Oil and Gas Production Needs Improvement*. (U.S. Government Accountability Office, 2014).
- Hamilton, D. C. Ken Regan (Delaware) Field, Reeves County, Texas. *AAPG Bulletin* **68**, 116–116 (1984).
- Hornbach, M. J. *et al.* Ellenburger wastewater injection and seismicity in North Texas. *Phys. Earth Planet. In.* **261**, 54–68 (2016).
- Jarvis, A., Reuter, H. I., Nelson, A. & Guevara, E. Hole-filled seamless SRTM data V4. Tech. rep., International Centre for Tropical Agriculture (CIAT). (2008).
- Karacan, C. Ö. Elastic and shear moduli of coal measure rocks derived from basic well logs using fractal statistics and radial basis functions. *Int. J. Rock Mech. Min. Sci.* **46**, 1281–1295 (2009).
- Kim, J.-W. & Lu, Z. Association between localized geohazards in West Texas and human activities, recognized by Sentinel-1A/B satellite radar imagery. *Sci. Rep.* **8**, [10.1038/s41598-018-23143-6](https://doi.org/10.1038/s41598-018-23143-6) (2018).
- Konkel, L. Salting the earth: the environmental impact of oil and gas wastewater spills. *Environ. Health Perspect.* **124**, A230–A235 (2016).
- Loesch, E. & Sagan, V. SBAS analysis of induced ground surface deformation from wastewater injection in East Central Oklahoma, USA. *Remote Sens.* **10**, [10.3390/rs10020283](https://doi.org/10.3390/rs10020283) (2018).
- Lu, Z. & Dzurisin, D. Ground surface deformation patterns, magma supply, and magma storage at Okmok volcano, Alaska, from InSAR analysis: 2. Coeruptive deflation, July–August 2008. *J. Geophys. Res. Solid Earth* **115**, [10.1029/2009JB006970](https://doi.org/10.1029/2009JB006970) (2010).
- Lu, Z. & Dzurisin, D. *InSAR Imaging of Aleutian Volcanoes: Monitoring a Volcanic Arc from Space*. (Springer, 2014).
- Mace, R. E., Mullican, W. F. & Angle, E. S. *Aquifers of West Texas*. (Texas Water Development Board, 2001).
- Meng, C. Benchmarking Defmod, an open source FEM code for modeling episodic fault rupture. *Comput. Geosci.* **100**, 10–26 (2017).
- Mercer, J. W. *Geohydrology of the Proposed Waste Isolation Pilot Plant site, Los Medanos Area, Southeastern New Mexico*. (U.S. Geological Survey, 1983).

- Meyer, J. E., Wise, M. R. & Kalaswad, S. *Pecos Valley Aquifer, West Texas: Structure and Brackish Groundwater*. (Texas Water Development Board, 2012).
- Mogi, K. Relations between the eruptions of various volcanoes and the deformations of the ground surfaces around them. *Bull. Earthq. Res. Inst.* **36**, 99–134 (1958).
- Nance, H. S. *Middle Permian basinal siliciclastic deposition in the Delaware Basin: the Delaware Mountain Group (Guadalupian)*. (Bureau of Economic Geology. The University of Texas at Austin, 2009).
- National Research Council. *Review of the Scientific and Technical Criteria for the Waste Isolation Pilot Plant (WIPP)*. (National Academy Press, 1984).
- Okada, Y. Surface deformation due to shear and tensile faults in a half-space. *Bull. Seismol. Soc. Am.* **75**, 1135–1154 (1985).
- Reeves County Groundwater Conservation District. *Reeves County Groundwater Conservation District Management Plan*. (Texas Water Development Board, 2018).
- Richey, S. F., Wells, J. G. & Stephens, K. T. *Geohydrology of the Delaware Basin and Vicinity, Texas and New Mexico*. (U.S. Geological Survey, 1985).
- Samsonov, S., Czarnogorska, M. & White, D. Satellite interferometry for high-precision detection of ground deformation at a carbon dioxide storage site. *Int. J. Greenh. Gas Con.* **42**, 188–199 (2015).
- Sharp, J. M. Regional Groundwater Flow Systems in Trans-Pecos Texas. in *Aquifers of West Texas* 41–55 (Texas Water Development Board, 2001).
- Shirzaei, M., Manga, M. & Zhai, G. Hydraulic properties of injection formations constrained by surface deformation. *Earth Planet. Sci. Lett.* **515**, 125–134 (2019).
- Sirivedhin, T. & Dallbauman, L. Organic matrix in produced water from the Osage-Skiatook Petroleum Environmental Research site, Osage county, Oklahoma. *Chemosphere* **57**, 463–469 (2004).
- Yang, Q. *et al.* InSAR monitoring of ground deformation due to CO₂ injection at an enhanced oil recovery site, West Texas. *Int. J. Greenh. Gas Con.* **41**, 20–28 (2015).
- Wright, T. J., Lu, Z. & Wicks, C. Source model for the Mw 6.7, 23 October 2002, Nenana Mountain Earthquake (Alaska) from InSAR. *Geophys. Res. Lett.* **30**, [10.1029/2003GL018014](https://doi.org/10.1029/2003GL018014) (2003).

CHAPTER 6

Effective volume detection: a case study of under-reported volume

6.1 Introduction

West Texas, one of the most prolific hydrocarbon-producing regions in the world, has recently been explored by energy companies because of the rich undiscovered resources (Gaswirth et al., 2018) as well as the application of improved oil recovery (IOR) and enhanced oil recovery (EOR) methods (Zapivalov, 2015). To manage the produced water in the oil and gas industry, the most common way is to inject wastewater into porous rock formations through disposal wells. Improper management of wastewater not only causes environmental and health concerns (Johnston et al., 2016) but sometimes also induces detectable surface uplift (Loesch and Sagan, 2018), which may further cause ground instability and threaten the infrastructures. The coupling of the pore fluid pressure to the rock deformation is usually considered a poroelastic process. Pressurized fluid injection forces fluid into the subsurface reservoir, thereby increasing pore fluid pressure in the reservoir that propagates outward from the well with time. This pressure perturbation causes deformation in the overlying strata and induces geodetically-detectable surface deformation and even seismicity (Tung et al., 2021). The local hydro-geomechanical parameters, especially Young's modulus and hydraulic conductivity, play an essential role in this poroelastic process because they control the pore pressure distribution and hence surface uplift (Newell et al., 2017). Reliable estimates are therefore critical to risk

prediction and minimization. However, precise local hydro-geomechanical parameters are seldom obtainable due to the lack of well logs in West Texas.

Interferometric Synthetic Aperture Radar (InSAR) is an effective tool to map ground deformation. With centimeter-to-millimeter level precision and meter-level resolution in a large region, this method has proven the capacity to detect surface deformation uplift induced by fluid injection in a localized or regional scale (Kim and Lu, 2018; Staniewicz et al., 2020; Samsonov et al., 2015). Previous studies indicated that InSAR observation can provide constraints on mechanical parameters (Yang et al., 2015) and hydrogeologic parameters (Shirzaei et al., 2019). The parameters of interest can be solved by jointly inverting the deformation observed by InSAR and well injection information (e.g., injection volume and depth, fluid density and temperature) (Shirzaei et al., 2019). The spatial time-series deformation derived by InSAR can provide a powerful constraint for the poroelastic process, but due to stringent computation constraints, many studies used only one spatial map (e.g., the cumulative deformation (Shirzaei et al., 2019), an interferogram (Alghamdi et al., 2020)) or temporal deformation at one location (Deng et al., 2020).

The finite element method (FEM) is widely used to solve poroelastic problems related to fluid injection, because it allows material heterogeneity, irregular boundaries, distributed mechanical loads, and multiple fluid sources (Kim and Deo, 2000; Yin et al., 2011; Denlinger and O'Connell, 2020). FEM is based on the Galerkin weighted residual procedure and a finite element discretization of the physical domain. Programs have been developed to solve poroelastic problems. Defmod (Ali, 2014) is a finite element code based on Biot's poroelastic theory (Biot, 1941) that has been successfully used to model deformation induced by wastewater disposal (Zheng et al., 2019) as well as to investigate deformation in a geothermal field (Ali et

al., 2018). We estimate parameters using the results from these numerical simulations based on Bayes theorem (Bishop, 2006).

The Bayesian inversion (Idier, 2013) has been applied to various geophysical inverse problems (Shen et al., 2013) including many poroelastic applications for the characterization of poroelastic materials using various data, such as InSAR measurements (Bagnardi and Hooper, 2018) and acoustical and mechanical measurements (Chazot et al., 2012). The Bayesian approach can quantify the constraints and prior conditions on model parameters, resulting in maximum a posteriori (MAP) estimates and confidence intervals of each parameter. Thus we can constrain our model parameters using both InSAR and well measurements, and include a priori knowledge of the parameters as well as data and model errors. The Monte Carlo method (Sambridge and Mosegaard, 2002) is a robust optimization method and has been widely implemented to characterize a posterior probability distribution in the Bayesian inference.

We use InSAR to measure the surface uplift induced by wastewater disposal at a site in west Texas. Deng et al. (2020) observed the uplift and modeled the surface deformation at the well with the maximum injection volume using a five-layer model assuming poroelastic behavior. In this research, The InSAR-derived spatio-temporal deformation is simulated by poroelastic FEM. A Bayesian Monte Carlo approach is applied to solve for local Young's modulus, hydraulic conductivity, and subsurface effective volumes, which can help understand the underlying mechanism and shed insights into the local hydrogeology.

6.2 Method

6.2.1 Research Area

The study site is located in the Delaware Basin, a hydrocarbon-rich sedimentary basin in west Texas (Fig. 6.1a). The geologic stratigraphy is shown in Table 6.1 according to previous geologic research (Beauheim and Holt, 1990; Dutton et al., 2003; Richey et al., 1985; Mercer, 1983; Nance, 2009; Freeze and Cherry, 1979) and well logs from EnverusTM. We divide the strata into three layers for the simulation based on the rock composition of each formation. The injection zone comprises Bell Canyon and Cherry Canyon because of their relatively-high hydraulic conductivities, in which the wastewater can diffuse away rapidly. Certainly, the injection depths of the wastewater disposal wells fall in the injection zone (Table 6.1). Above the injection zone, the caprock is defined to be the layers above the Delaware Mountain Group, formed in upper and post Permian. Although the Rustler Aquifer and the post Permian sediments are pervious, formations from Lamar to Yates with impervious rock composition can be regarded as confining layers, allowing the simplification of one-layer caprock. Underneath the injection zone, the Brushy Canyon and the Bone Spring formation are considered to be base rock with relatively low hydraulic conductivities, preventing the diffusion of the wastewater.

7 injection wells and 55 production wells were active in the research period (Fig. 6.1, Table 6.2). Only the injection wells near the deformation center contribute to the surface deformation (Deng et al., 2020). 13 production wells are located in the Bone Spring formation (~2.8 km deep), and the other 42 wells produce from the Wolfcamp formation (~3.5 km deep). Monthly injection volume records of the wastewater disposal wells (Fig. 6.1b) are archived in the Railroad Commission of Texas (Texas RRC).

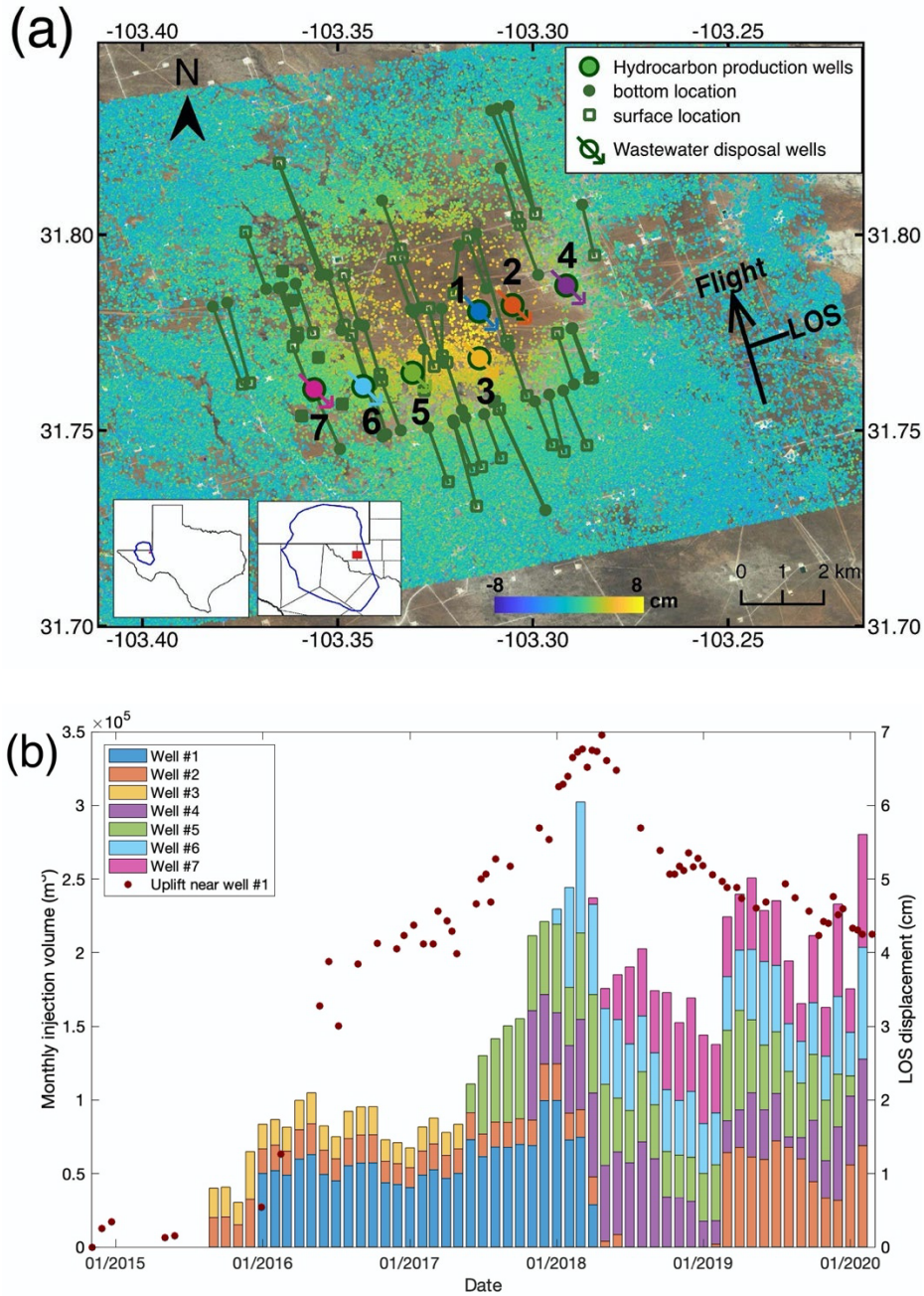


Figure 6.1 Background information in the research area. **(a)** Maximum cumulated line-of-sight (LOS) deformation map from Nov. 2014 to May 2018. Color-coded circles with arrows and green symbols indicate the location of 7 wastewater disposal wells and 55 hydrocarbon production wells active during the research period in the deformation area, respectively. Horizontal wells are plotted as green lines linking the surface and bottom locations. The blue contour in the lower left panels represents the boundary of the Delaware basin and the red rectangle marks the research area. **(b)** Reported monthly injection volumes of the 7 wastewater disposal wells (color-coded bars) from the Railroad Commission of Texas (Texas RRC) and time series of InSAR LOS deformation near well #1 (red circles).

System	Series	Formation	Main rock type	Formation tops (km)	Layers in the model
		Post Permian sediments			Caprock
Permian	Ochoan	Rustler	Halite	0.221	
	Guadalupian	Yates	Anhydrite/Dolomite	0.696	
		San Andres	Anhydrite/Dolomite	1.093	
		Lamar	Limestone/shale	1.567	
		Bell Canyon	sandstone	1.577	Injection zone
		Cherry Canyon	sandstone/siltstone	1.856	
		Brushy Canyon	sandstone/shale	2.319	Base rock
	Leonardian	Bone Spring	Limestone/sandstone	2.777	
	Wolfcampian	Wolfcamp	shale	3.565	

Table 6.1 Geologic stratigraphy.

Injection Well No.	API No.	Field	County	Fluid type	Injection interval (km)
1	4249533675	WINK, S.	WINKLER (TX)	Salt Water (100%)	1.58 - 2.32
2	4249530150	WINK, S.	WINKLER (TX)	Salt Water (100%)	1.58 - 2.30
3	4249510835	WINK, S.	WINKLER (TX)	Salt Water (100%)	1.58 - 1.97
4	4249533871	WINK, S.	WINKLER (TX)	Salt Water (100%)	1.59 - 2.28
5	4230133335	PHANTOM	LOVING (TX)	Salt Water (100%)	1.58 - 1.93
6	4230133444	WINK, S.	LOVING (TX)	Salt Water (100%)	1.61 - 2.29
7	4230133840	WINK, S.	LOVING (TX)	Salt Water (100%)	1.59 -2.30

Table 6.2 7 wastewater disposal wells.

6.2.2 InSAR processing

SAR images from November 2014 to February 2020 acquired from ascending track P78 of Sentinel 1A/B are processed to measure the surface deformation. The C-band data (wavelength of 5.55 cm) are sensitive to detect small magnitude deformation and the short time interval (6 or 12 days) allows temporally dense observations. To obtain the spatiotemporal deformation, the Stanford Method for Persistent Scatterers (StaMPS) (Hooper, 2008), a software that incorporates persistent scatterer and small baseline methods and is widely used for estimating time-series deformation precisely (more details in Hooper et al., 2004, 2007 and Hooper, 2008), is applied to extract coherent pixels, mitigate atmospheric artifacts (primarily in water-vapor rich summer), and track surface movements at the persistent scatterers. Because the InSAR observations are relative in space and time, the first acquisition date (November 2014)

and clusters of pixels distant from the deforming location assuming that the neighboring area is not experiencing significant deformation are used for references in both domains. The time-series line-of-sight (LOS) deformation maps are downsampled using quadtree downsampling (Dutton et al., 2003) for model simulation to reduce computation and maintain enough significant information on the deformation pattern.

6.2.3 Forward poroelastic finite element model

To simulate InSAR observed deformation, a three-layer three-dimensional finite element model is built. 107,654 tetrahedral elements are generated in the mesh file to describe the geometry of the three-layer geologic settings and the injection points. The elements are denser near the injection points for better spatial resolution (Fig. 6.2). The mesh covers an area of 20 km x 20 km, and the origin point of the mesh is set to the surface location of the dominant well #1. The vertical direction of the top surface is set to be a free surface while other boundaries are set far away and fixed because the horizontal displacement in the far field is negligible. We suppose the geologic settings in the research area are laterally homogenous because the InSAR observation seems to be spatially continuous without abrupt jumps (Fig. 6.5a), and the research site is localized (~2 km radius). We analyze fluid injection using the poroelastic module of Defmod (Ali, 2014) and solve for the surface deformation resulting from the fluid injection. The fundamental equations (Zienkiewicz and Taylor, 2000; Lewis and Schrefler, 1998) based on Biot's theory consist of momentum conservation (Eq. 6.1) and the continuity equation for mass conservation (Eq. 6.2):

$$\nabla \cdot \boldsymbol{\sigma} - \boldsymbol{\alpha} \nabla p = \mathbf{f}, \quad \boldsymbol{\sigma} = \mathbf{D} \boldsymbol{\epsilon}, \quad (6.1)$$

where \mathbf{D} is the elasticity matrix which can be represented with Young's modulus E and Poisson's ratio ν , $\boldsymbol{\alpha}$ is the tensor matrix for Biot's coefficient,

$$C\dot{p} - \nabla \cdot \frac{K}{\rho_f g} \nabla p - \alpha \epsilon = q, \quad (6.2)$$

where $C = \frac{\alpha - \varphi}{K_s} + \frac{\varphi}{K_f}$, φ is porosity, K_s is the bulk modulus of rock, K_f is the bulk modulus of fluid, K is hydraulic conductivity, ρ_f is the fluid density.

The coupled system of equations can be rewritten as Eq. 6.3 using the finite element method:

$$\begin{aligned} K_e u - H p &= f \\ H^T \dot{u} + S \dot{p} + Q p &= q \end{aligned} \quad (6.3)$$

where K_e is solid stiffness matrix, H is the coupling matrix, S is the fluid compressibility matrix, Q is the fluid permeability matrix, u is the displacement field, f is the body force, p is the pressure vector and q is the volumetric flow into and out of the well. The mesh file, along with information including material properties, boundary conditions, time steps, and injection volumes are plugged into Defmod to solve the governing equations.

Reported injection/production records are collected mainly from Texas RRC, the primary state regulator of oil-related activities in Texas, and EnverusTM. Due to the monthly reported volume, the time step is set to one month. The output is the three-dimensional displacement field, we then convert the displacement to LOS direction and interpolate the time-series deformation to dates of InSAR observed data for further comparison.

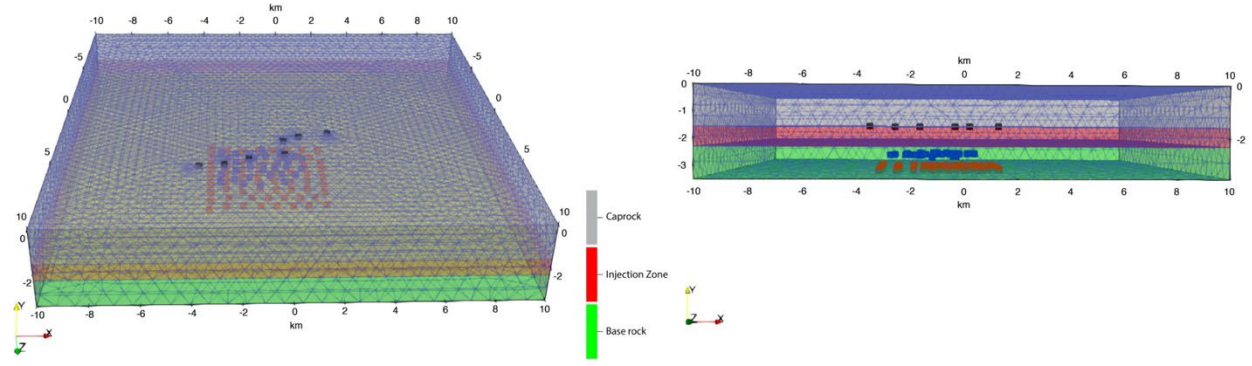


Figure 6.2 Mesh of the Three-layer finite element model. Reference point is the location of well #1. Black dots represent the locations of 7 wastewater disposal wells. Blue and red dots indicate the nodes for production in Bone Spring formation and Wolfcamp formation, respectively.

6.2.4 Bayesian Monte Carlo approach

In a Bayesian framework, the posterior probability density function (PDF), $p(\mathbf{m}|\mathbf{d})$, can be computed from the prior PDF $p(\mathbf{m})$ that modulates any prior information about the model parameters \mathbf{m} independent of the observed data, and the likelihood function $p(\mathbf{d}|\mathbf{m})$ expresses the probability distribution of \mathbf{d} when the parameters are given as \mathbf{m} . The un-normalized posterior distribution $p(\mathbf{m}|\mathbf{d})$, based on the misfit between \mathbf{d} and the predicted model, is:

$$p(\mathbf{m}|\mathbf{d}) \propto p(\mathbf{d}|\mathbf{m})p(\mathbf{m}) \quad (6.4)$$

Here the data vector $\mathbf{d} = \{d^1, d^2, \dots, d^n\}$ are the spatio-temporal deformation observed by InSAR ($n = 66$ is the number of InSAR images), the model parameters $\mathbf{m} = \{m^1, m^2, \dots, m^l\}$ are Young's modulus, hydraulic conductivities in three layers, and the scaling factors of effective volumes to reported volumes in injection well #1 ($l = 7$ is the number of total model parameters). If the poroelastic model is defined as \mathbf{G} , then the likelihood function is simply related to the standard deviation of all the data-model misfits, defined here as $S(\mathbf{G}(\mathbf{m}), \mathbf{d})$, as:

$$p(\mathbf{d}|\mathbf{m}) = \exp(-0.01 \times S(\mathbf{G}(\mathbf{m}), \mathbf{d})) \quad (6.5)$$

The Markov Chain Monte Carlo samples the model space to generate the evolution of posterior distribution. An initial series of model parameters $\mathbf{m}_{i=0}$ is selected from prior information, where i is the number of iterations. A new series of model parameters can be generated by making a perturbation to each parameter of \mathbf{m}_i and plugged into Defmod. The likelihood functions $p(\mathbf{d}|\mathbf{m}_i)$ and $p(\mathbf{d}|\mathbf{m}_{i+1})$ are then recomputed. The Metropolis law defines the probability of acceptance for model parameters \mathbf{m}_{i+1} :

$$P_{\text{accept}} = \begin{cases} 1 & \text{if } p(\mathbf{d}|\mathbf{m}_{i+1}) \geq p(\mathbf{d}|\mathbf{m}_i) \\ p(\mathbf{d}|\mathbf{m}_{i+1})/p(\mathbf{d}|\mathbf{m}_i) & \text{if } p(\mathbf{d}|\mathbf{m}_{i+1}) < p(\mathbf{d}|\mathbf{m}_i) \end{cases} \quad (6.6)$$

We define the threshold of acceptance $\chi_{\text{crit}} = \chi_{\text{min}} + 0.25$, where χ_{min} is the minimum misfit (Fig. 6.3). Here we choose the initial values by referring to previous research (Zheng et al., 2019).

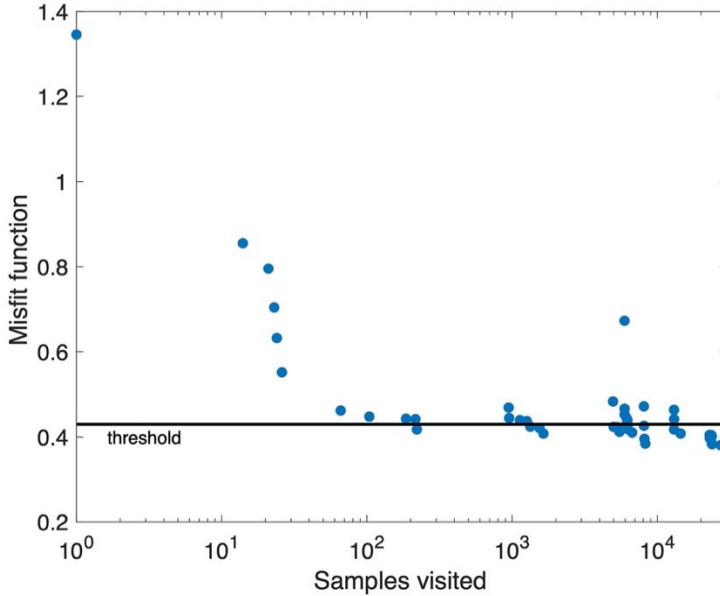


Figure 6.3 Convergence of Monte Carlo.

Poisson's ratio	0.25
Fluid density	1020 kg/m ³
Fluid bulk modulus	2.3×10 ⁹ Pa
Porosity	0.05
Biot coefficient	1
Rock density	2.5×10 ³ kg/m ³

Table 6.3 Parameters used in the poroelastic model.

6.3 Results

6.3.1 InSAR analysis

We observe surface uplift and the follow-on recovery over an area with a radius of ~2 km at the site in Winkler and Loving counties, west Texas (Fig. 6.1a). Compared to the smaller amount of average monthly production volumes from deeper formations, the larger volumes and shallower depths of injection are more likely to contribute to surface uplift that we have measured with InSAR. The maximum deformation of ~7 cm is observed near the injection well #1 around May 2018 (Fig. 6.1a), exactly at the end of the injection of this well, and the deformation began to recover afterward, the approximately flat pattern after May 2018 indicates a mild disposal scheme in terms of ground instability. In addition, the start of the uplift coincided with the start of injection in well #1, and the trend of the InSAR time series matches with the monthly injection record of well #1 (Fig. 6.4a). Taking both the spatial proximity and temporal agreement into account, well #1 can be considered the dominant well for the observed

deformation, thus we have added the scaling factor of injection volume in well #1 into model parameters (discussed in 6.4.1).

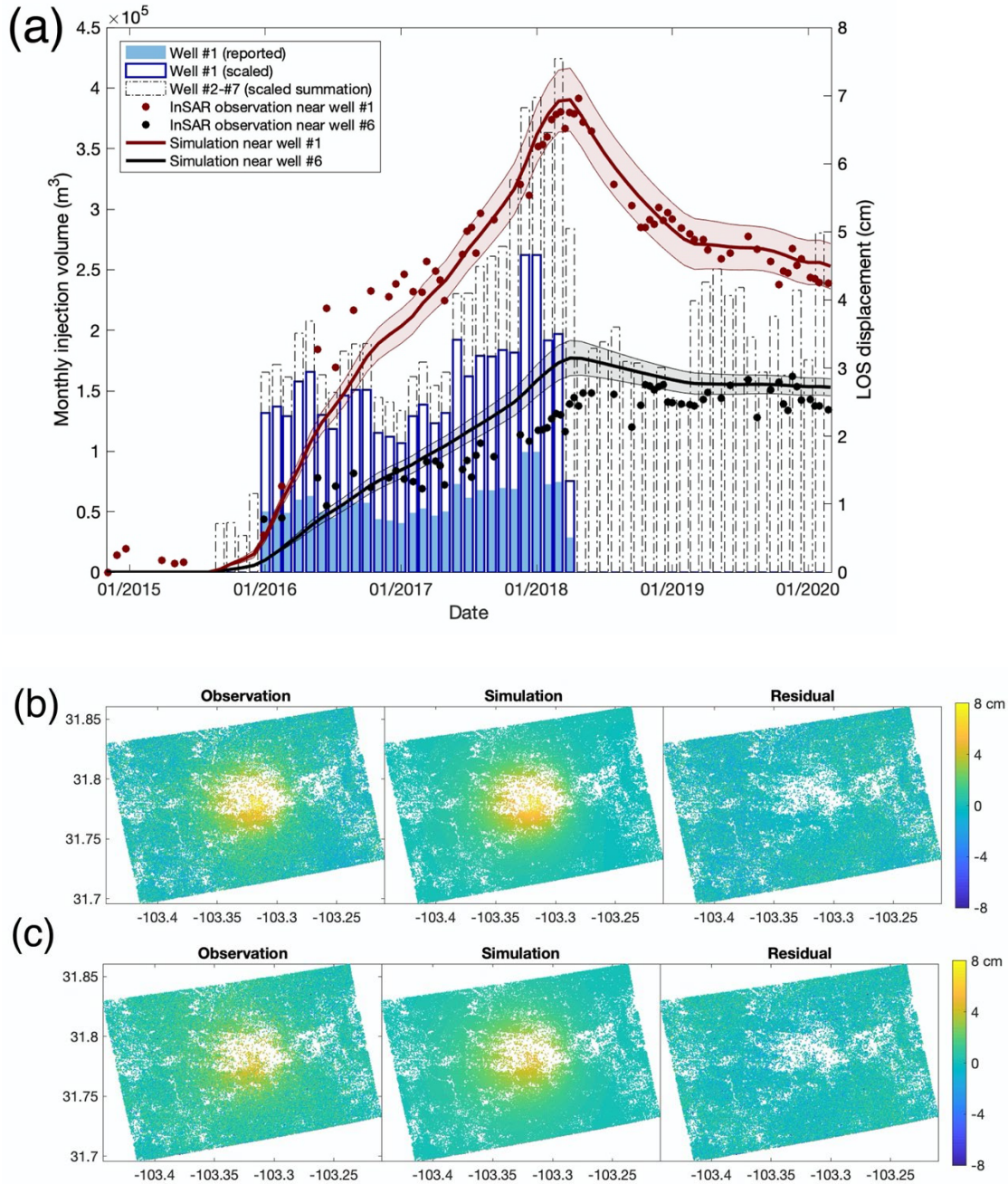


Figure 6.4 Results from the Bayesian Monte Carlo approach. (a) Comparison between time series displacement from InSAR observation (circles) and the best-fit simulation (solid lines) in the inversion period. Uncertainty is plotted with semi-opaque ranges. Blue filled and void bars

represent the reported volume from RRC and scaled effective volume from the best-fit simulation of well #1, respectively. **(b)** Maximum cumulative InSAR observed displacement, best-fit simulation, and the residual maps in May 2018. **(c)** Cumulative InSAR observed displacement, best-fit simulation, and the residual maps at the end of the whole research period with scaled volume.

With results from Bayesian inversion of the InSAR spatio-temporal observations, the best-fit simulation is calculated from the forward poroelastic finite element modeling plugging in the MAP estimates of model parameters including Young's modulus, hydraulic conductivity, and the scaling factor of injection volume in well #1. Uncertainty is calculated based on the standard deviation of accepted models from the Monte Carlo method. Spatial maps of InSAR displacements and the best-fit simulation based on the Bayesian Monte-Carlo approach in May 2018 (i.e., the maximum displacement) (Fig. 6.4b) and the end of the research period (Fig. 6.4c) are compatible with each other. The simulation of the temporal evolution of the maximum displacement point (near well #1) agrees closely with the observation, especially the change in the displacement rate after March 2019.

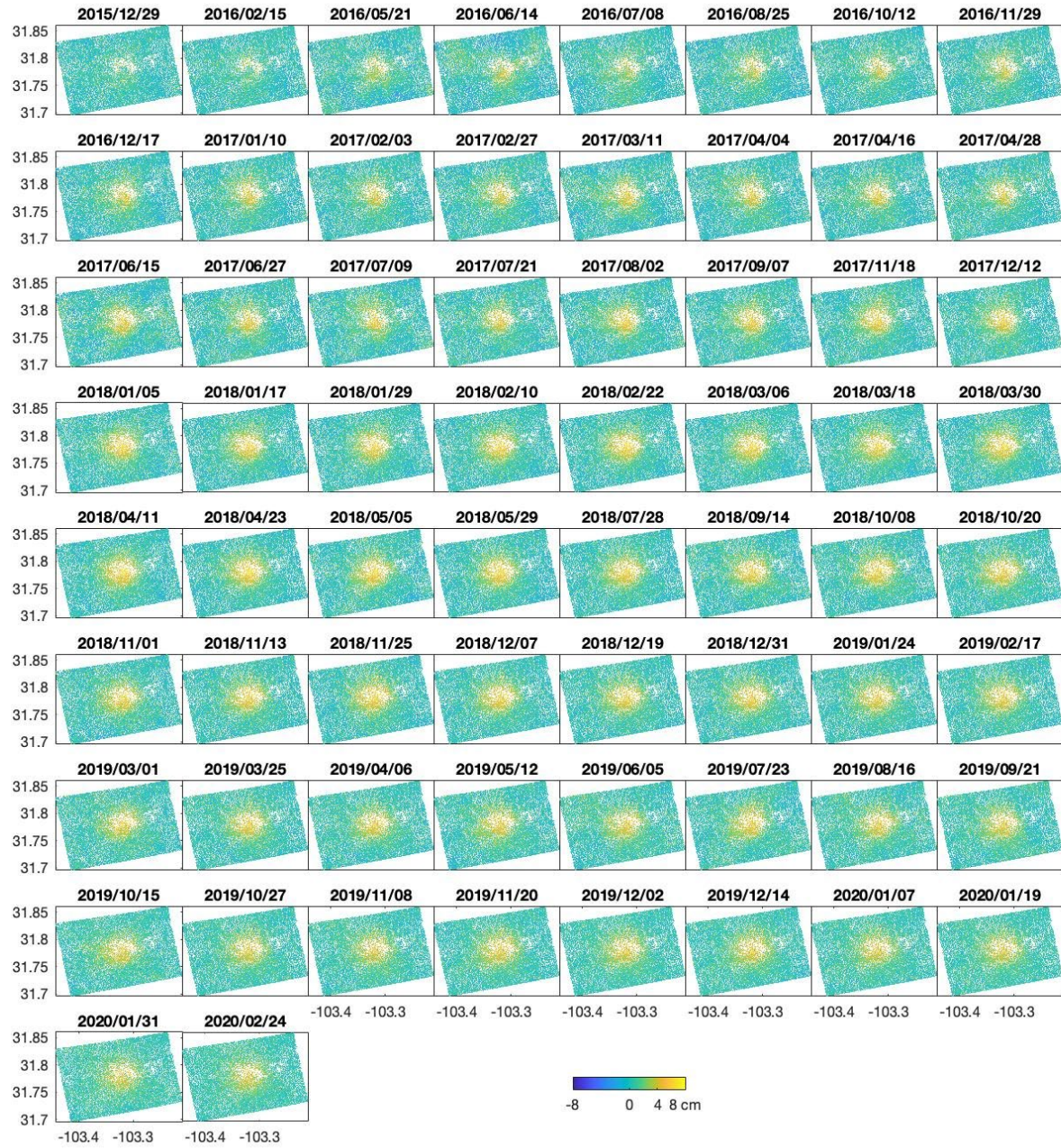
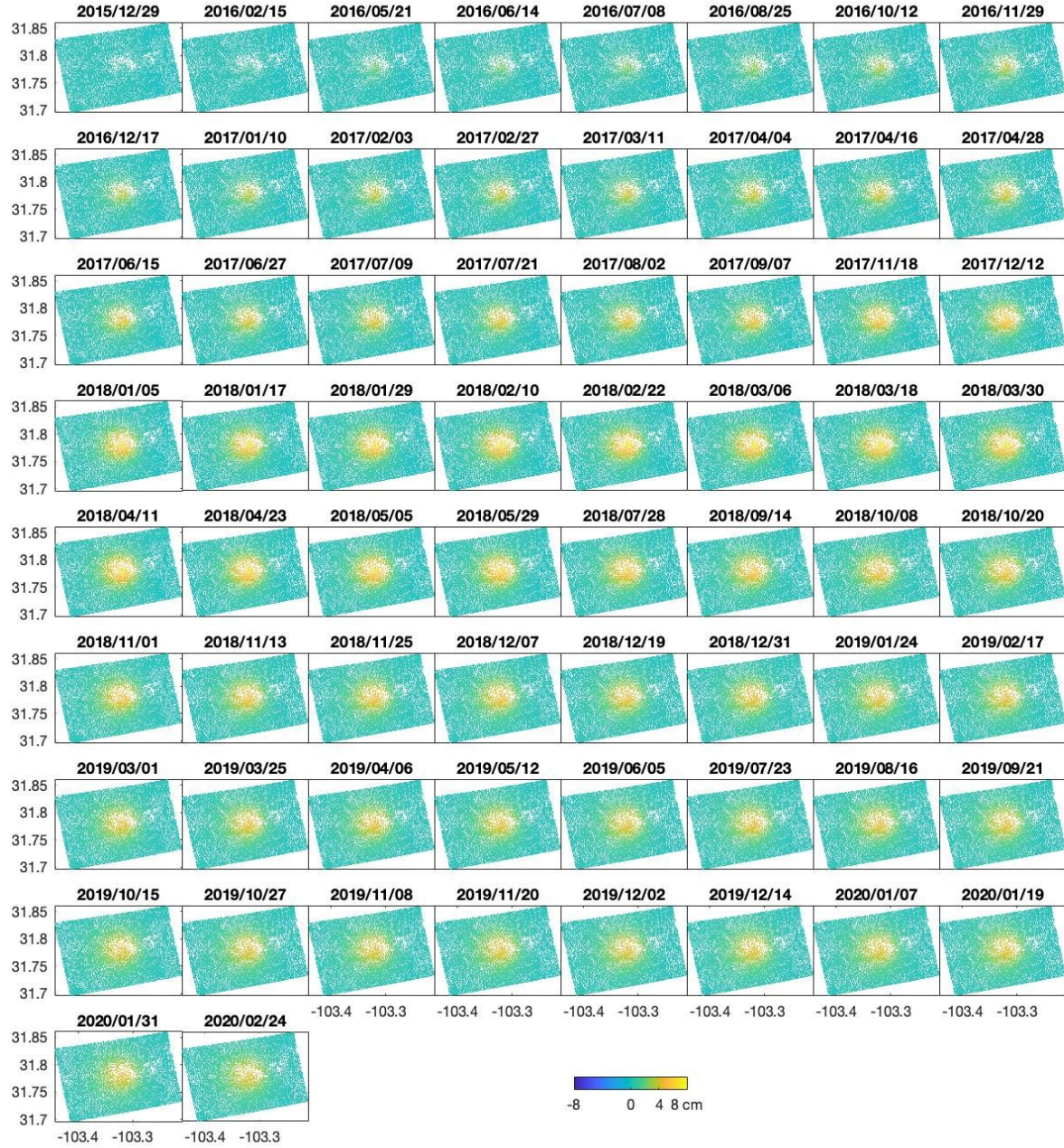
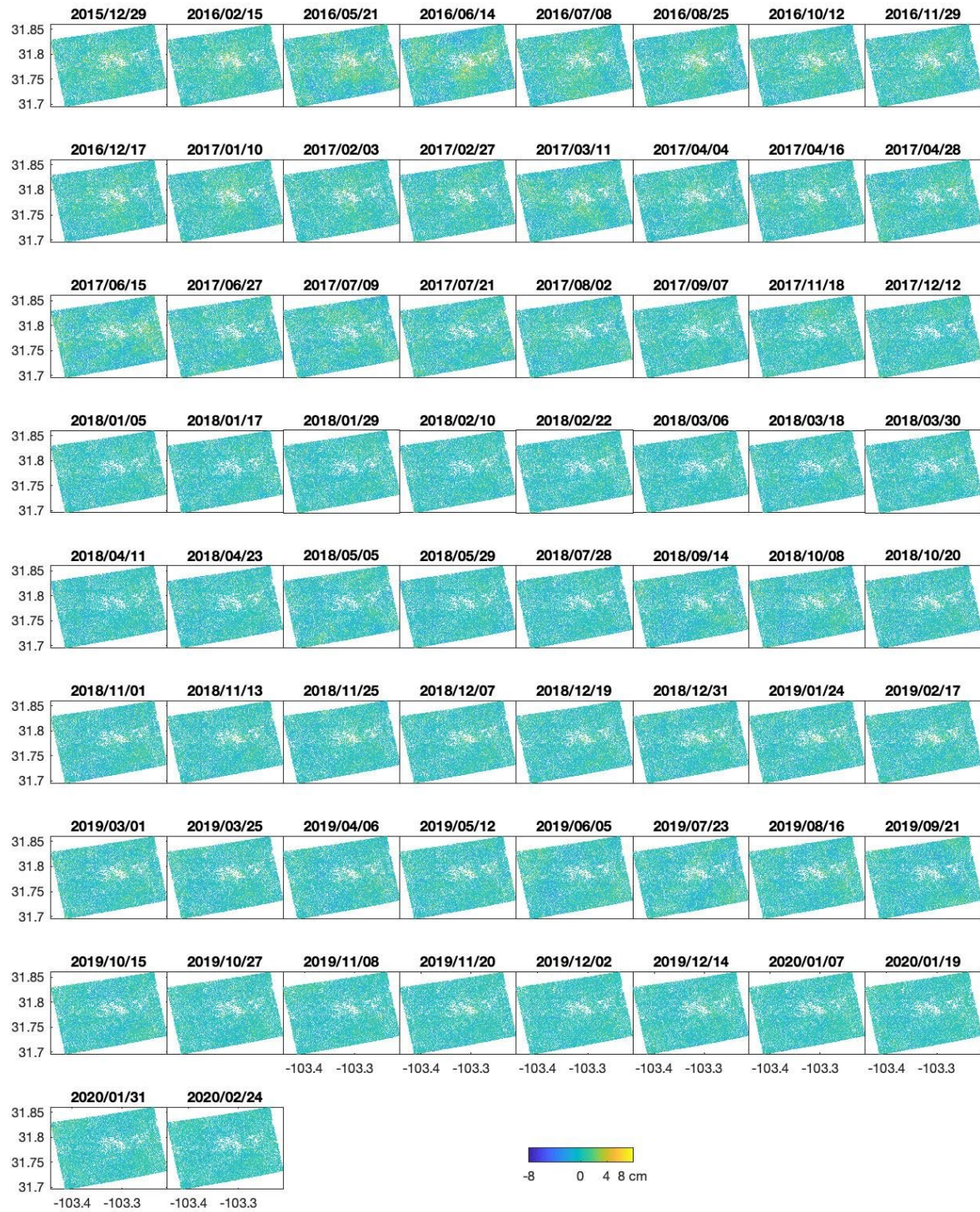


Figure 6.5 Observation, simulation and residuals. **(a)**. InSAR observation after injection starts.



(b). Best-fit simulations.



(c). Residuals.

6.3.2 Estimated injection volumes and hydro-geomechanical parameters

Marginal posterior probability distributions are plotted in Fig. 6.6, where the MAP probability estimates and the confidence intervals of the model parameters can be found.

The estimated effective injection volumes are found to be ~ 2.6 times as much as the reported volumes in the dominant well #1. This disparity is qualitatively reasonable. Based on the assumption of no heterogeneity and no abrupt temporal change of the hydro-mechanical parameters, if there is no excess of reported volumes in well #1, similar uplift would be expected in March 2019 because of the comparable reported volumes from well #2 (Fig. 6.1b). However, no uplift has been observed by our InSAR analysis (discussed in 6.4.1). As no other injection is found in this area, this discrepancy leads to the skepticism of reported volumes from the oil company. The results of effective volumes could provide invaluable information for wastewater disposal management and regulation.

Young's modulus in the caprock, the injection zone, or the base rock approaches 80 GPa, which is comparatively high but still within the reasonable range in this field (Yang et al., 2015). All three layers can reach convergences no matter whether the layer is a confining layer or not.

As for hydraulic conductivity, the situation is different. The best-fit simulation suggests the hydraulic conductivity in the injection zone to be 5.97×10^{-8} m/s, seemingly a bit low when compared to the frequently used values of Bell Canyon $10^{-6} \sim 10^{-7}$ m/s (Deng et al., 2020) but still within the reasonable range (Beauheim, 1990). The reason can be the fact that the injection zone could involve not only sandstone but also siltstone or dolostone. The disparity of only half of a magnitude is acceptable considering the combination with Cherry Canyon. This result confirms the feasibility of the division of the injection zone layer. Unlike Young's modulus, hydraulic conductivity in caprock and base rock fails to converge. This should be attributed to the prior

distribution based on the fact that the caprock and the base rock are confining layers (Table 1). When those two layers are set to be impervious, all hydraulic conductivities in the impervious range can seal and preserve fluid in the injection zone. The failure to converge further suggests the caprock and the base rock can be considered as a single layer each.

Although the complicated local hydrogeology may cause site-limited validity of the hydro-mechanical parameters, they can still help provide a reference for adjacent oil fields and also study the future evolution of this case.

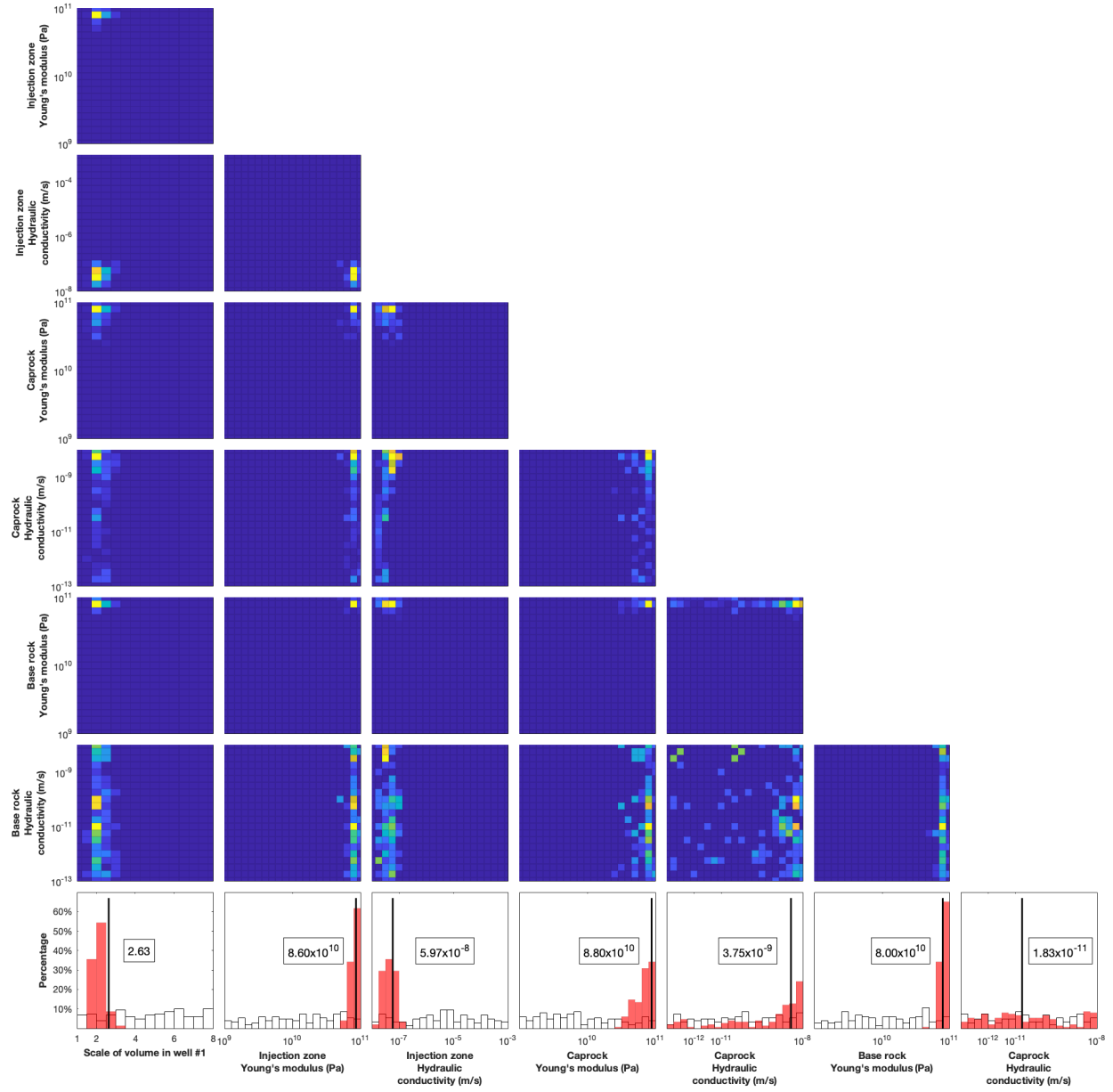


Figure 6.6 Marginal posterior probability distributions. One-dimensional figures are prior (open histograms) and posterior distributions (red histograms) of all model parameters. Two-dimensional marginals are plotted according to frequency (cold colors for low frequency, warm colors for high frequency).

6.4 Discussion

6.4.1 Why are injection volumes added to model parameters?

The InSAR observation data can be separated into three periods: 1) November 2014 to May 2018; 2) May 2018 to February 2019; and 3) March 2019 to February 2020. In period 1, injection in well #1 dominates the uplift which occurs at the beginning of this injection and ends at the completion of the injection. In period 2, the uplift starts to recover and keeps at a relatively large deformation rate. As the trend starts directly from the completion of well #1, the whole period 2 can be considered as recovery due to the end of the injection. In period 3, the deformation rate becomes smaller, reflecting some perturbation at around March 2019. Since well #1 has not been reactivated after August 2019 while well #2, which is only 0.5 km from the deformation center, has been reactivated at the start of period 3, the variation of the deformation rate is highly likely due to the reactivation of well #2.

This study was initially proposed to solve local hydrogeology. Thus, the original model parameter set consists of only three Young's modulus and three hydraulic conductivities, and the injection volume of well #1 is fixed as the reported volume. The results with reported volumes are plotted in Fig. 6.7. Although we can find some parameters within the reasonable range to fit the observed deformation in periods 1 and 2, we always see a deformation rebounding after the reactivation of well #2 in period 3. The rebound is found not only from the best-fit simulation but all the accepted models (Fig. 6.7b), which means the Bayesian Monte Carlo method cannot return to an acceptable simulation in this time interval if only hydro-geomechanical parameters are used as model parameters.

When the best solution cannot fit surface deformation, both the geologic stratigraphy and injection information could be questioned as they are the two preset components in the inversion.

As described in 6.3.2, failure of convergence for hydraulic conductivities in the caprock and base rock can further convince the feasibility of one-layer caprock and base rock each. The depths of geologic layers are implied from well logs which are believed to be relatively accurate. The sample spaces of hydro-geomechanical parameters are in a fairly large range. Hence, we have determined to maintain the geologic stratigraphy and question the injection information.

The two crucial factors in the injection record impacting surface deformation are depth and volume. Supposing the effective depth is in the caprock or base rock where the hydraulic conductivity is low, the wastewater should diffuse away slowly, and the surface deformation after the completion of injection of well #1 should maintain the level or alleviate tardily. Therefore, the abrupt, and almost simultaneous retrieval of the surface uplift after May 2018 suggests retaining the reported depths. Eventually, the reported volumes are questioned. Thus, we apply scaling factors of the monthly injection volumes of the well(s). In consideration of the spatial proximity between the well locations and the deformation center, the temporal correlation, and the relatively large amount of volume per month, we add the scaling factor for injection volume in well #1 into the model parameters to calculate the effective injection volume.

The fact of no rebounding observed by InSAR itself can provide a piece of evidence for the excess effective volume of well #1. The simulation of rebounding is due to the compatible reported injection volume rate of well #1 in period 1 and well #2 in period 3 and the small distance between these two wells. To fix this problem, the excess of reported volumes in well #1 is a reasonable explanation for the discrepancy of displacements in periods 1 and 3 because it relatively reduces the contribution for surface uplift from injection volumes from well #2. Actually, in the case of scaled volume, some of the accepted models also show the same pattern of rebounding after the reactivated injection volume in well #2 (Fig. 6.7b). The patterns of

deformation near well #1 in the validation period lean to rebound: the smaller the excess effective volume is, the severer the rebounding is. In addition, according to Deng et. al (2020), modifications to the Skempton ratio were made to solve for the deformation with a poroelastic model, which also suggests that normal parameters of Young's modulus and hydraulic conductivity cannot fit the InSAR observation. Here we attribute this anomaly to excess effective injection volume.

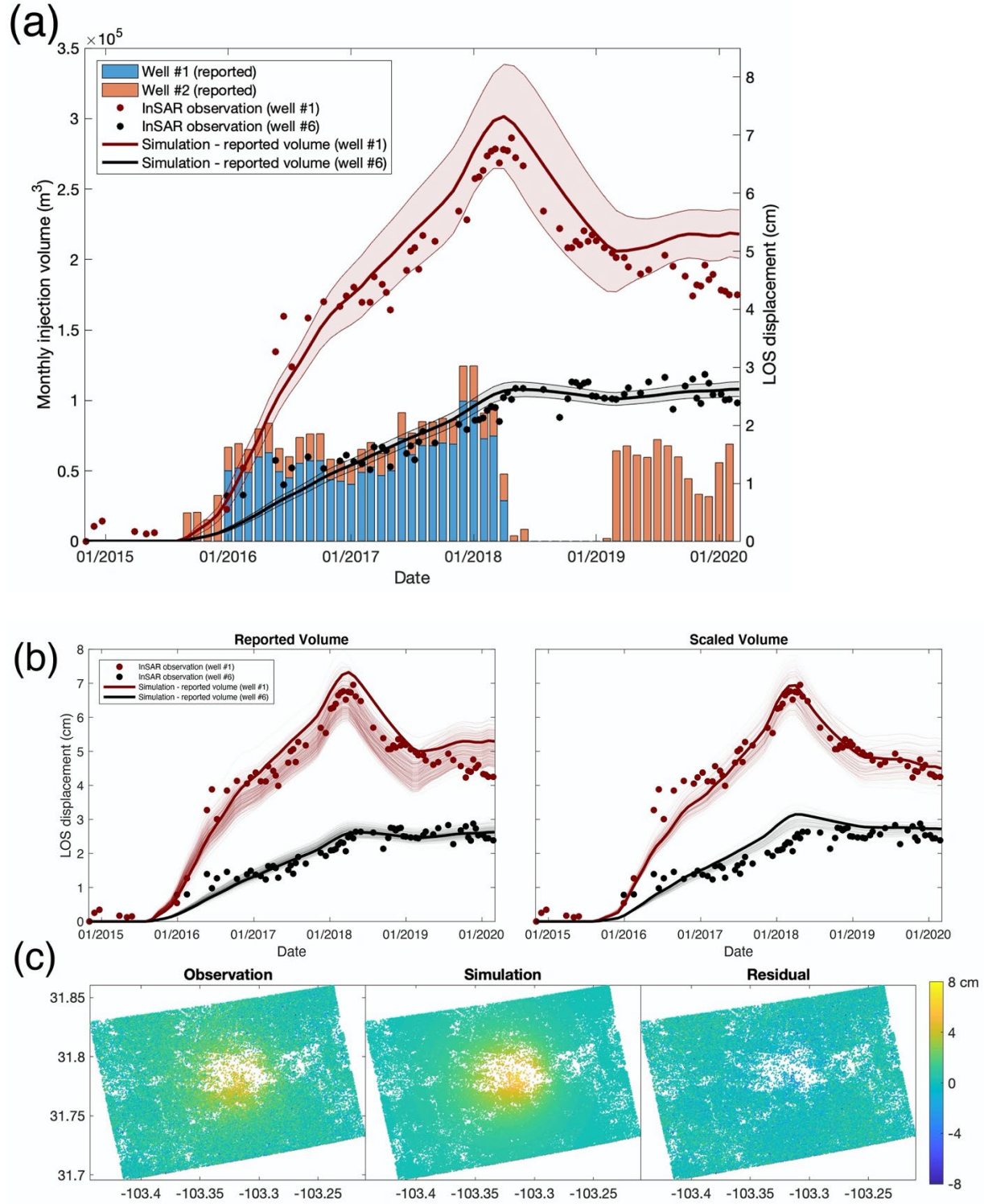


Figure 6.7 Best-fit results based on fixed reported volume. **(a)** Comparison between time series displacement from InSAR observation (circles) and the best-fit simulation (solid lines) in the whole research period using reported injection volume from Texas RRC. Uncertainty is plotted with semi-opaque ranges. Reported monthly injection volumes in well #1 and #2 in the whole

research period are plotted using bars. **(b)** Accepted models in one run (30000 times) are plotted as semi-opaque lines. **(c)** Maximum cumulative InSAR observed displacement, simulation based on reported injection volume, and the residual map in May 2018.

6.4.2 Production

As for hydrocarbon production, the deformation rate is almost zero from Nov 2014 to Dec 2015 when there was no injection but production, indicating the production events do not induce surface displacement. Hence, we did not include it in the modeling. Taking account of the production in deeper formation that generally induces surface subsidence, adding production information to the inversion will require even more excess injection volume to reach the InSAR observation, thus the conclusion of excess injection volume will remain the same. We provide a rough estimate of the influence of hydrocarbon production with the average injection rate based on yearly production and peak production from EnverusTM in Fig. 6.8. Although the total hydrocarbon production per month in Wolfcamp formation is comparable with the injection volume, it is less likely to impact the localized surface deformation because it is a semi-pervious aquifer with a large depth. Here we care about production in the shallower Bone Spring formation, which is more than 1 magnitude impervious than the Wolfcamp formation. Although the monthly volume rate of injection per well is ten times larger than the production for Bone Spring formation, the densely distributed production wells still generate subsidence up to 0.7 cm (Fig. 6.8a), which means the excess effective volume could be even larger.

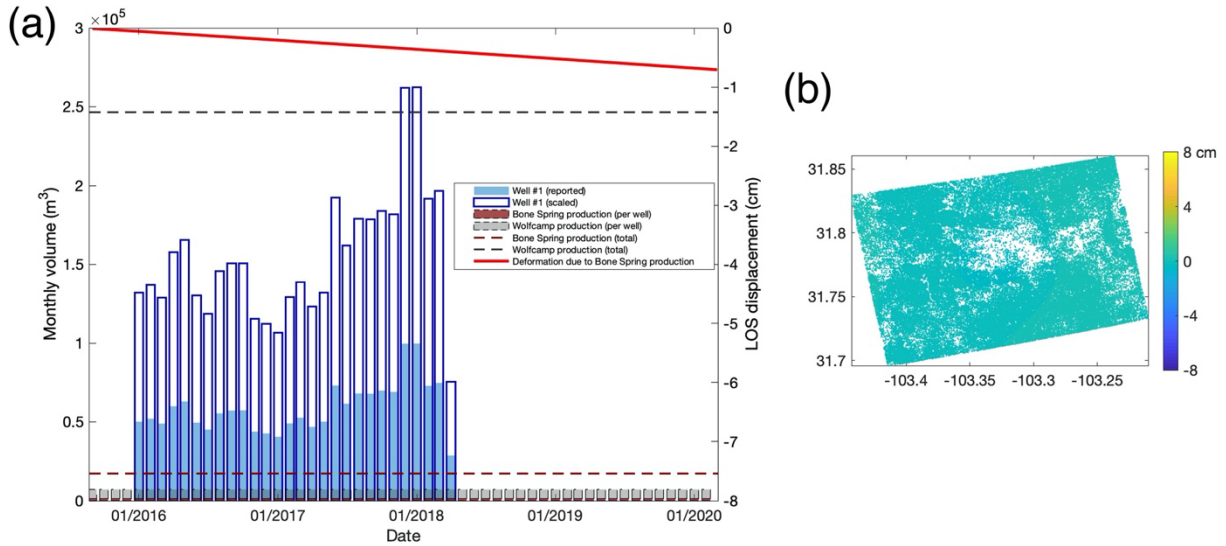


Figure 6.8 Production. **(a)** Comparison between monthly injection volume rate from dominating well #1 and monthly hydrocarbon production volume rate from Bone Spring formation and Wolfcamp formation. Red line is the LOS surface displacement induced by production from Bone Spring formation. **(b)** Spatial map of the simulated surface displacement induced by production from Bone Spring formation.

6.4.3 Possibility of fewer constraints

The Bayesian Monte Carlo approach is a robust method compared to others: it allows for a priori knowledge about the parameters, calculates probabilities of MAP estimates, characterizes a posterior probability distribution, and gives confidence intervals of each parameter (Fig. 6.6).

In terms of InSAR constraints, several studies used only temporal displacements of the deformation center or the cumulative spatial deformation of the whole research period in the deformation modeling due to the huge computation burden, which could lead to biased solutions and may not satisfy other constraints. Here we have explored the posterior probability distributions using constraints such as spatio-temporal data, the cumulative spatial deformation

map, and the temporal evolution of the deformation center, respectively (Fig. 6.9). Marginal distributions are shown in Fig. 6.10.

In this case, spatial constraints cannot simulate the temporal evolution, especially in period 3 (Fig. 6.9a). The temporal constraints perform better to simulate period 3 but underfit the spatial deformation range (Fig. 6.9b). The MAP estimates for hydro-geomechanical parameters of the three methods are all at the same magnitude, while spatial constraints and temporal constraints have a smaller scale factor of injection volume in well #1, which explains their failure to simulate period 3. The narrower distributions and the highest probabilities of MAP estimates of spatio-temporal constraints both indicate that utilizing the whole spatio-temporal InSAR data can be used to discard biased solutions substantially and reach better convergence. Therefore, to reduce the computation burden, spatial constraints and temporal constraints are good choices for quick rough results, but if possible, the use of spatio-temporal InSAR data as constraints is a better option for precise local hydrogeology retrieval.

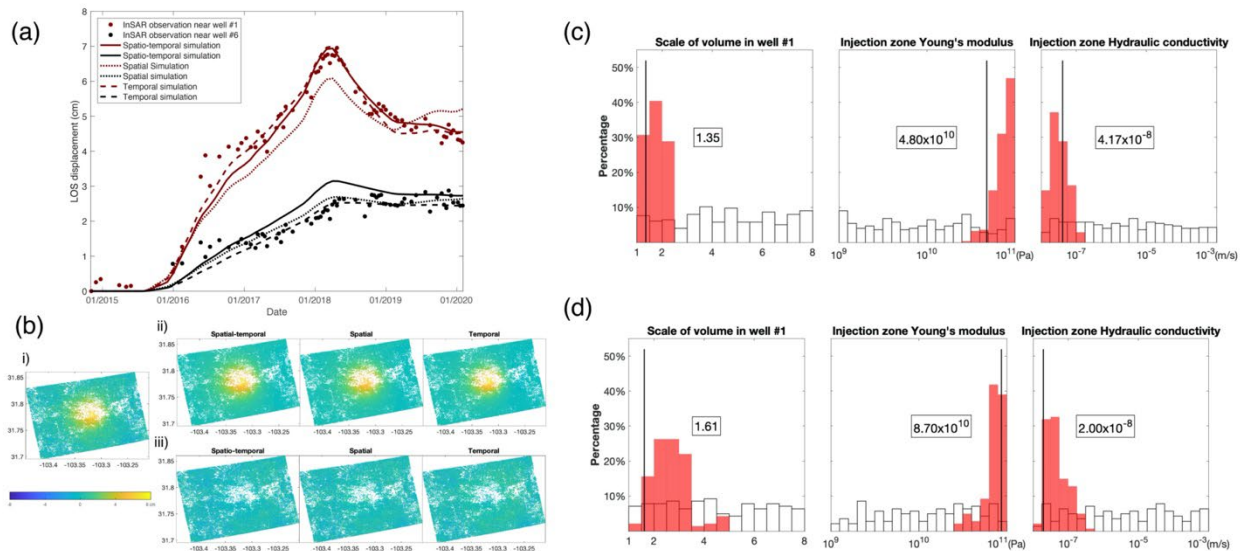


Figure 6.9 Comparison of the methods using constraints as the whole spatio-temporal constraints, one cumulative spatial deformation map (spatial constraints), and temporal evolution

of the deformation center (temporal constraints). **(a)** Temporal displacement near well #1 and #6 of the three constraints. **(b)** Maximum deformation at 2018/05. i) Observation; ii) Simulation; iii) Residuals. **(c)** Posterior distributions and MAP estimates of the three main model parameters using spatial constraints. **(d)** Posterior distributions and MAP estimates of the three main model parameters using temporal constraints.

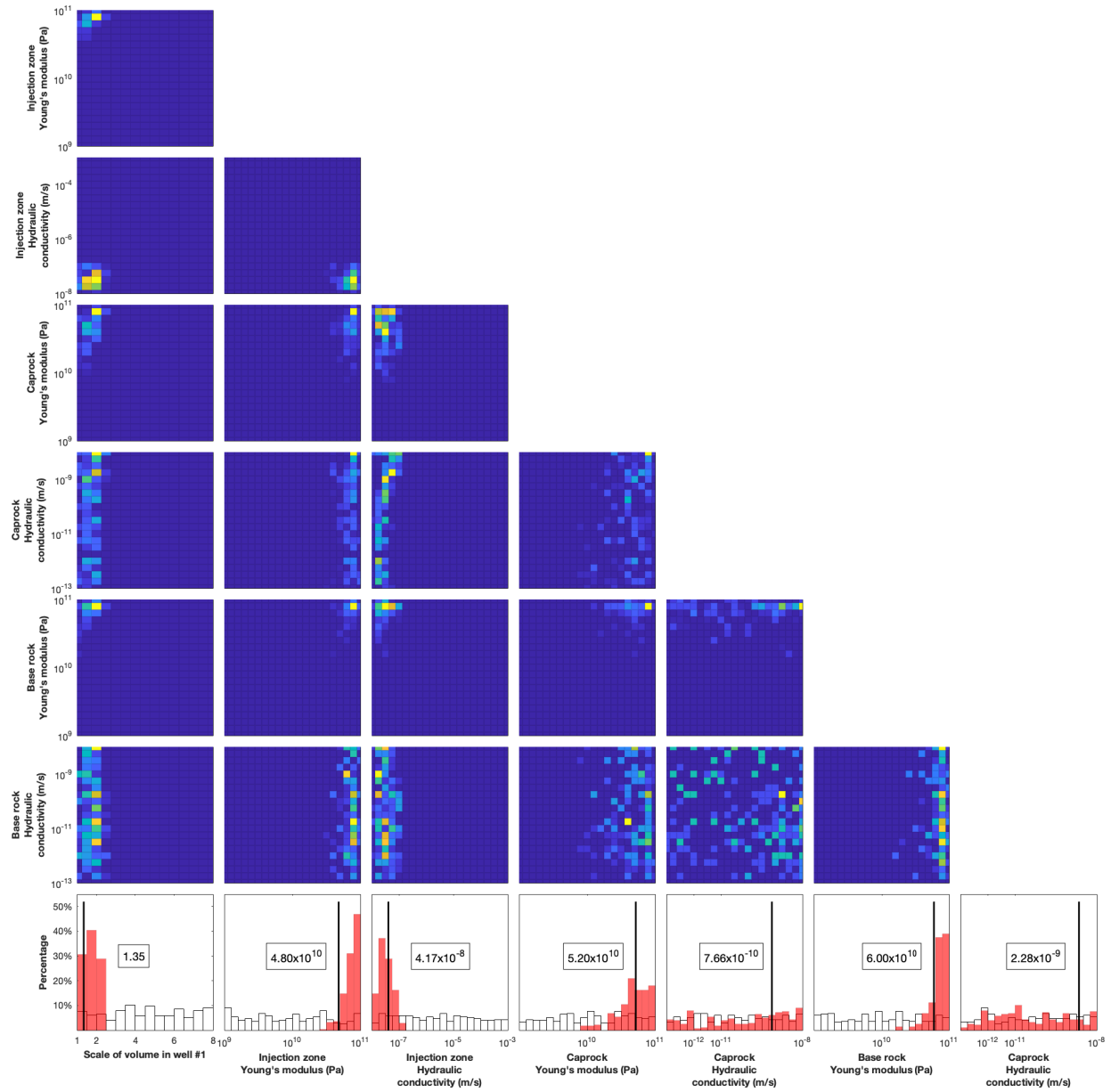
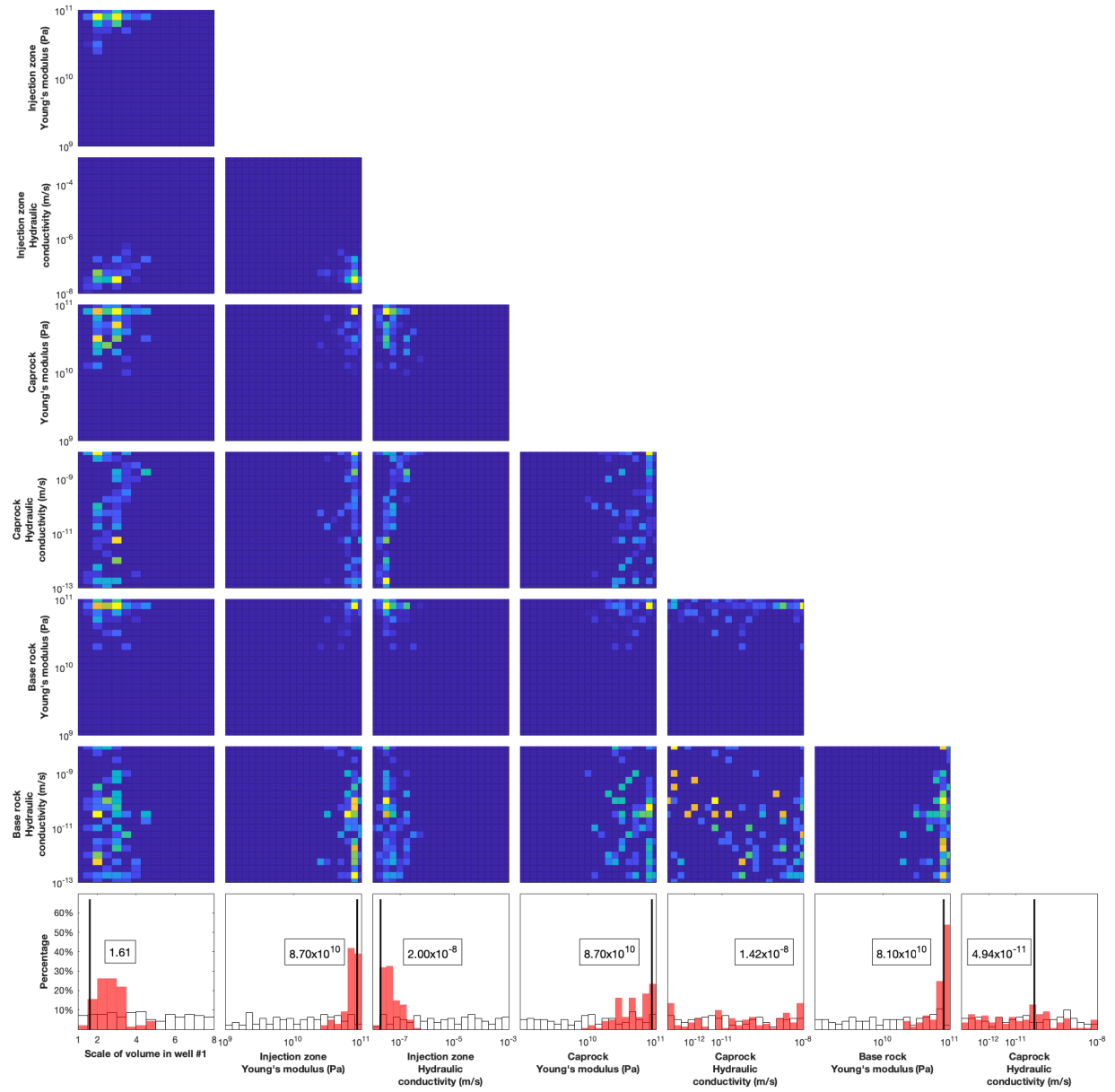


Figure 6.10 Marginal distributions **(a)**. Marginal distributions using spatial constraints.



(b). Marginal distributions using temporal constraints.

6.5 Conclusion

In this study, InSAR has been applied to measure the spatio-temporal localized surface displacement related to fluid injection. The surface uplift and recovery afterward at the site in Winkler county, west Texas, is mainly dominated by the wastewater disposal in well #1. The Bayesian Monte Carlo approach with a forward poroelastic finite element modeling performs well to solve the uplift induced by wastewater injection. The best-fit simulation matches well with the InSAR observation data. The posterior distribution provides reasonable MAP estimates and uncertainties of Young's modulus and hydraulic conductivity. The effective volumes needed to make the results make sense in dominant well #1 are found to be ~ 2.6 times than the reported volumes. Compared to other constraints, the Bayesian Monte Carlo approach with a forward poroelastic finite element modeling of InSAR-derived spatio-temporal data as constraint shows its advantages in solving poroelastic problems related to wastewater disposal. Our analysis provides a new technique to estimate local hydrogeologic properties which can serve as a reference for adjacent oil fields. Furthermore, our study provides a scientific basis for wastewater disposal management and regulation.

Reference

- Alghamdi, A., Hesse, M. A., Chen, J., & Ghattas, O. (2020). Bayesian poroelastic aquifer characterization from InSAR surface deformation data. Part I: Maximum a posteriori estimate. *Water Resources Research*, 56(10), e2020WR027391.
- Ali, S. T. (2014). Defmod-Parallel multiphysics finite element code for modeling crustal deformation during the earthquake/rifting cycle, *arXiv preprint arXiv:1402.0429*.
- Ali, S. T., Reinsch, E. C., Moore, J., Plummer, M., Warren, I., Davatzes, N. C., & Feigl, K. L. (2018). Geodetic measurements and numerical models of transient deformation at Raft River geothermal field, Idaho, USA, *Geothermics*, 74, 106-111.
- Bagnardi, M. & Hooper, A. (2018). Inversion of surface deformation data for rapid estimates of source parameters and uncertainties: A Bayesian approach. *Geochemistry, Geophysics, Geosystems*, 19(7), 2194-2211.
- Beauheim, R. L., & Holt, R. M. (1990). Hydrogeology of the WIPP Site. *Geological and hydrological studies of evaporites in the northern Delaware Basin for the Waste Isolation Pilot Plant (WIPP), New Mexico: Geological Society of America (available from Dallas Geological Society), Field Trip, 14*, 131-179.
- Biot, M. A. (1941). General theory of three-dimensional consolidation. *Journal of applied physics*, 12(2), 155-164.
- Bishop, C.M., (2006). Pattern recognition and machine learning, 738 pages, Springer, ISBN-10: 0-387-31073-8.
- Chazot, J.D., Zhang, E. & Antoni, J. (2012). Acoustical and mechanical characterization of poroelastic materials using a Bayesian approach. *The Journal of the Acoustical Society of America*, 131(6), 4584-4595.
- Deng, F., Dixon, T. H., & Xie, S. (2020). Surface deformation and induced seismicity due to fluid injection and oil and gas extraction in western Texas. *Journal of Geophysical Research: Solid Earth*, 125(5), e2019JB018962.
- Denlinger, R.P. and O'Connell, D.R.H. (2020), Evolution of stress and tectonic faulting induced by deep fluid injection, Paradox Basin, Colorado, *Bull. Seism. Soc. America*, 110 (5), 2308–2327.
- Dutton, S. P., Flanders, W. A., & Barton, M. D. (2003). Reservoir characterization of a Permian deep-water sandstone, East Ford field, Delaware basin, Texas. *AAPG bulletin*, 87(4), 609-627.
- Freeze, R. A., & Cherry, J.A. (1979). Groundwater. Prentice-Hall, Inc.

- Gaswirth, S. B., French, K. L., Pitman, J. K., Marra, K. R., Mercier, T. J., Leathers-Miller, H. M., ... & Le, P. A. (2018). Assessment of undiscovered continuous oil and gas resources in the Wolfcamp Shale and Bone Spring Formation of the Delaware Basin, Permian Basin Province, New Mexico and Texas, 2018 (No. 2018-3073). US Geological Survey.
- Hooper, A., Zebker, H., Segall, B., & Kampes, B. (2004). A new method for measuring deformation on volcanoes and other natural terrains using InSAR persistent scatterers, *Geophysical Research Letters*, 31, L23611.
- Hooper, A., Segall, P., & Zebker, H. (2007). Persistent scatterer interferometric synthetic aperture radar for crustal deformation analysis, with application to Volcán Alcedo, Galápagos. *Journal of Geophysical Research*, 112, B07407.
- Hooper, A. (2008). A multi-temporal InSAR method incorporating both persistent scatterer and small baseline approaches. *Geophysical Research Letters*, 35, L16302.
- Idier, J. (Ed.). (2013). *Bayesian approach to inverse problems*. John Wiley & Sons.
- Johnston, J. E., Werder, E., & Sebastian, D. (2016). Wastewater disposal wells, fracking, and environmental injustice in southern Texas. *American Journal of Public Health*, 106(3), 550-556.
- Kim, J. G., & Deo, M. D. (2000). Finite element, discrete-fracture model for multiphase flow in porous media. *AIChE Journal*, 46(6), 1120-1130.
- Kim, J. W., & Lu, Z. (2018). Association between localized geohazards in West Texas and human activities, recognized by Sentinel-1A/B satellite radar imagery. *Scientific reports*, 8(1), 1-13.
- Lewis, R. W. and Schrefler, B.A. (1998) *The Finite Element Method in the Static and Dynamic Deformation and Consolidation of Porous Media*. John Wiley & Sons.
- Loesch, E., & Sagan, V. (2018). SBAS analysis of induced ground surface deformation from wastewater injection in East Central Oklahoma, USA. *Remote Sensing*, 10(2), 283.
- Mercer, J.W. (1983). *Geohydrology of the Proposed Waste Isolation Pilot Plant Site, Los Medanos Area, Southeastern New Mexico*. US Department of the Interior, Geological Survey.
- Nance, H.S. (2009). Middle Permian Basinal siliciclastic deposition in the Delaware Basin: The Delaware Mountain Group (Guadalupian). *Bureau Econ. Geol., The University of Texas at Austin*, 180.
- Newell, P., Yoon, H., Martinez, M. J., Bishop, J. E., & Bryant, S. L. (2017). Investigation of the influence of geomechanical and hydrogeological properties on surface uplift at In Salah. *Journal of Petroleum Science and Engineering*, 155, 34-45.

- Richey, S. F., Wells, J. G., & Stephens, K. T. (1985). *Geohydrology of the Delaware Basin and vicinity, Texas and New Mexico* (No. 84-4077). Open-File Services Section, Branch of Distribution.
- Sambridge, M., & Mosegaard, K. (2002). Monte Carlo methods in geophysical inverse problems. *Reviews of Geophysics*, 40(3), 3-1.
- Samsonov, S., Czarnogorska, M., & White, D. (2015). Satellite interferometry for high-precision detection of ground deformation at a carbon dioxide storage site. *International Journal of Greenhouse Gas Control*, 42, 188-199.
- Shen, W., Ritzwoller, M. H., Schulte-Pelkum, V., & Lin, F. C. (2013). Joint inversion of surface wave dispersion and receiver functions: a Bayesian Monte-Carlo approach. *Geophysical Journal International*, 192(2), 807-836.
- Shirzaei, M., Manga, M., & Zhai, G. (2019). Hydraulic properties of injection formations constrained by surface deformation. *Earth and Planetary Science Letters*, 515, 125-134.
- Staniewicz, S., Chen, J., Lee, H., Olson, J., Savvaidis, A., Reedy, R., Breton, C., Rathje, E., & Hennings, P. (2020). InSAR Reveals Complex Surface Deformation Patterns Over an 80,000 km² Oil-Producing Region in the Permian Basin. *Geophysical Research Letters*, 47(21), e2020GL090151.
- Tung, S., Zhai, G., & Shirzaei, M. (2021). Potential link between 2020 Mentone, West Texas M5 earthquake and nearby wastewater injection: Implications for aquifer mechanical properties. *Geophysical Research Letters*, 48(3), e2020GL090551.
- Yang, Q., Zhao, W., Dixon, T. H., Amelung, F., Han, W. S., & Li, P. (2015). InSAR monitoring of ground deformation due to CO₂ injection at an enhanced oil recovery site, West Texas. *International Journal of Greenhouse Gas Control*, 41, 20-28.
- Yin, S., Dusseault, M. B., & Rothenburg, L. (2011). Coupled THMC modeling of CO₂ injection by finite element methods. *Journal of Petroleum Science and Engineering*, 80(1), 53-60.
- Zapivalov, N. P. (2015). Improved oil recovery vs. enhanced oil recovery. *Enhanced Oil Recovery: Methods, Economic Benefits and Impacts on the Environment*, 81-94.
- Zheng, W., Kim, J. W., Ali, S. T., & Lu, Z. (2019). Wastewater leakage in West Texas revealed by satellite radar imagery and numerical modeling. *Scientific reports*, 9(1), 1-11.
- Zienkiewicz, O. and Taylor, R. (2000). *The Finite Element Method: The Basis*. Butterworth-Heinemann.

CHAPTER 7

A case study of aseismic slip induced by fluid injection

7.1 Introduction

The natural fault systems can exhibit both fast slip as conventional earthquakes in a few seconds or minutes and slow aseismic slip with durations from days to years. The slow slip events seem harmless but play an important role during the earthquake cycle because they can change the stress field aseismically and pose potential risks to future earthquakes. Hydrocarbon industry operations including wastewater injection and hydraulic fracturing can increase the pore pressure, which decreases the effective normal stress on adjacent faults, enhances the chances of fault slip. While the research awareness of fluid injection and induced seismicity has been growing (Healy et al., 1968; Hennings et al., 2019), the mechanism of aseismic slip induced by fluid injection should be investigated. Eyre et al. (2022) observed paired uplift and subsidence ground deformation during hydraulic fracturing and defined it to be a slow slip event. Aseismic motions induced by fluid injection have been identified both through direct observations and through their indirect effects (Cornet, 2016).

Our study examines a case of aseismic slip in the northern part of the Midland Basin. The research region is in a normal faulting stress state and the direction of maximum horizontal compression (S_{Hmax}) in this area is NW-SE (Lund Snee & Zoback, 2018). Although most of the newly mapped shallow normal faults strike sub-parallel to the local direction of S_{Hmax} as

Coulomb faulting theory predicts (Dvory and Zoback, 2021), the respective orientation of the basement-rooted faults in the Midland Basin can be various (Horne et al., 2022).

7.2 Method

7.2.1 Research Area

The study site (Fig. 7.1) is located in the northernmost Midland Basin, a hydrocarbon-rich sedimentary basin inside of the Permian Basin. 27 injection wells and 47 production wells are located in this region (Fig. 7.2a). The target formation of them is almost the Glorieta formation while some are Clear Fork formation. Local stratigraphy is listed in Table 7.1. With information including well logs and reports from oil companies, the contour of the target formation, Glorieta formation, is plotted in Fig. 7.2b, which shapes like a valley. Among all the hydrocarbon wells, the injection well with API#21935700 is the dominant well for the ground uplift considering the matching of the injection period and the spatial proximity (Fig. 7.3).

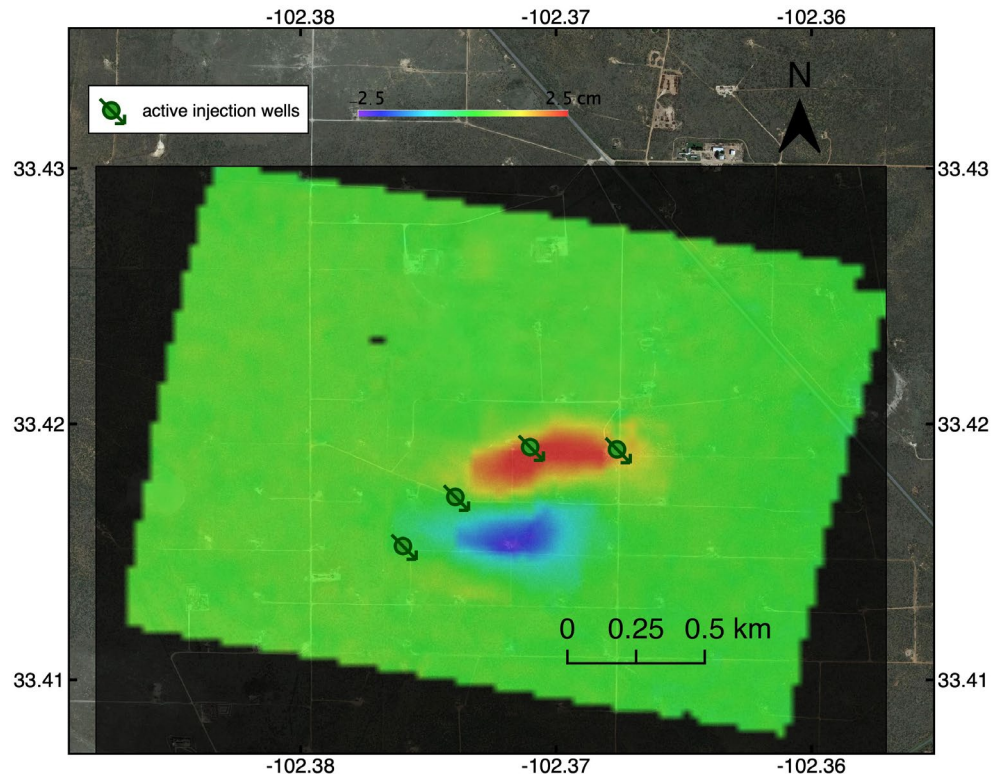


Figure 7.1 Research Area. The base map is the LOS deformation from 2020/01/01 to 2020/01/25.

Formation	Depth (m)
Red bed santa rosa	339
Yates	909
San Andres (active CO2 flooding)	1,571
San Andres sand	1,719
Glorieta	1,824
Clearfork	2,048
ABO	2,310
Wichita Albany	2,433
Wolfcamp	2,864
Canyon	2,957
Cisco	2,988
Strawn	3,049

Table 7.1 Geologic Stratigraphy.

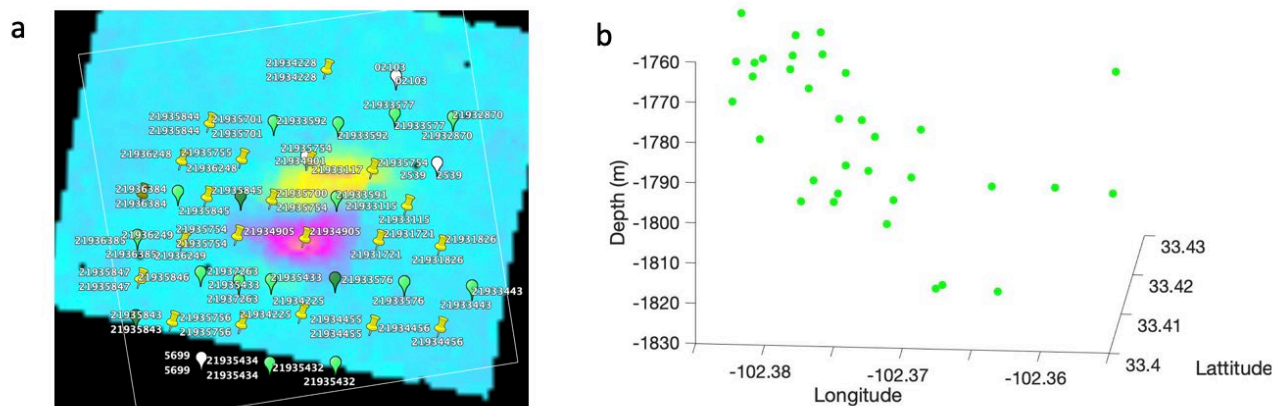


Figure 7.2 Hydrocarbon industry wells and the injection formation contour.

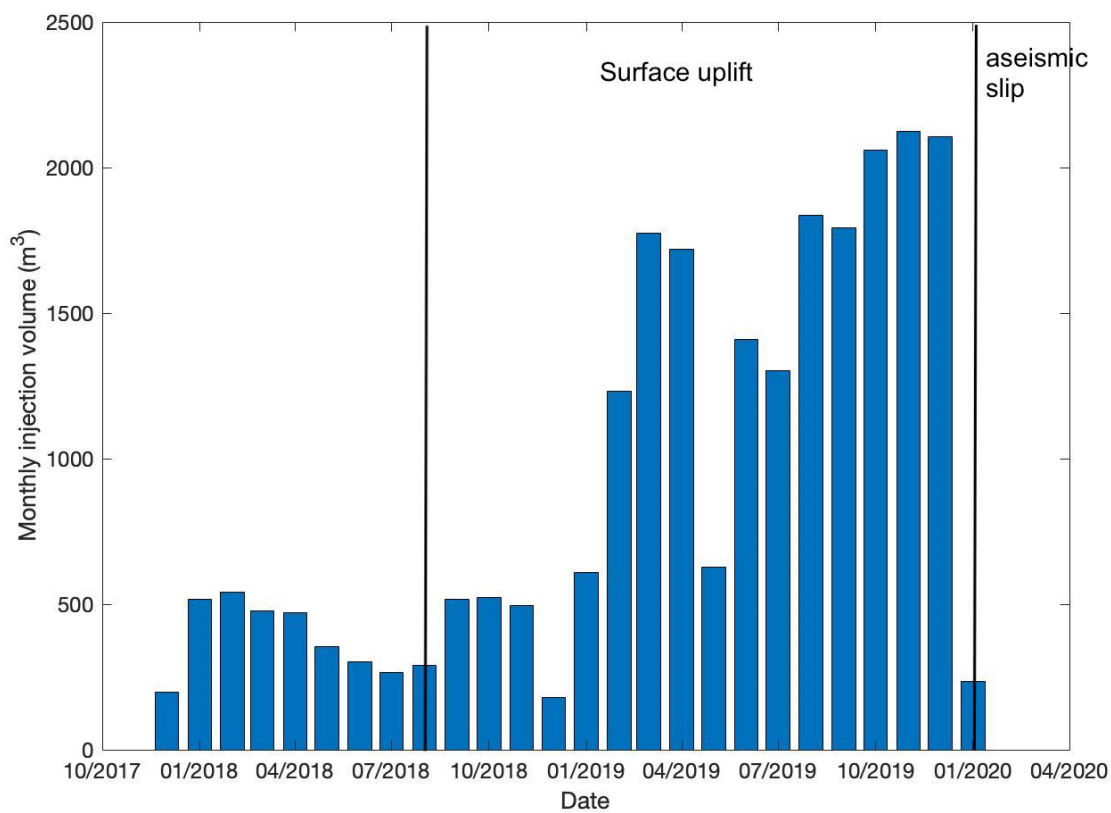


Figure 7.3 Monthly injection volumes of well #21935700.

7.2.2 InSAR processing

SAR images from November 2014 to date acquired from ascending track P78 and descending track P85 of Sentinel 1A/B are processed to measure the surface deformation. The C-band data (wavelength of 5.55 cm) are sensitive to detect small magnitude deformation and the short time interval (6 or 12 days) allows temporally dense observations. Ground uplift is detected from August 2018 to January 2020, then the deformation patterns change to paired lobes of uplift and subsidence from January 2020 to March 2020. The time series processing is implemented separately for the two time periods. As SAR images are available from both ascending and descending tracks, Multidimensional Small Baseline Subset (MSBAS) is applied by combining the two tracks to retrieve two-dimensional deformation: in vertical and east-west directions (Samsonov and d'Oreye, 2017).

7.2.3 Modeling

We use the Okada dislocation model (Okada, 1985) to simulate the aseismic slip detected by InSAR. To solve for the fault parameters, we use Bayesian inversion via Geodetic Bayesian Inversion Software (GBIS) (Battaglia et al., 2013). With the monthly injection volume from well #21935700 and the local stratigraphy, we apply poroelastic finite element models to simulate the ground uplift before the aseismic slip and calculate the pore pressure distribution on the fault plane via Defmod (Ali, 2014).

7.3 Results

As plotted in Fig. 7.4, the vertical deformation for the ground uplift cumulates to ~ 8 cm while the horizontal movement is ~ 3 cm mainly to the west, which suggests horizontal heterogeneity that a barrier exists at the east of the deformation pattern. The paired lobe of uplift

and subsidence has a maximum vertical displacement up to 1 cm with comparatively small east-west movement. The east boundary of this pattern aligns with that of the previous ground uplift, convincing for the horizontal heterogeneity hypothesis.

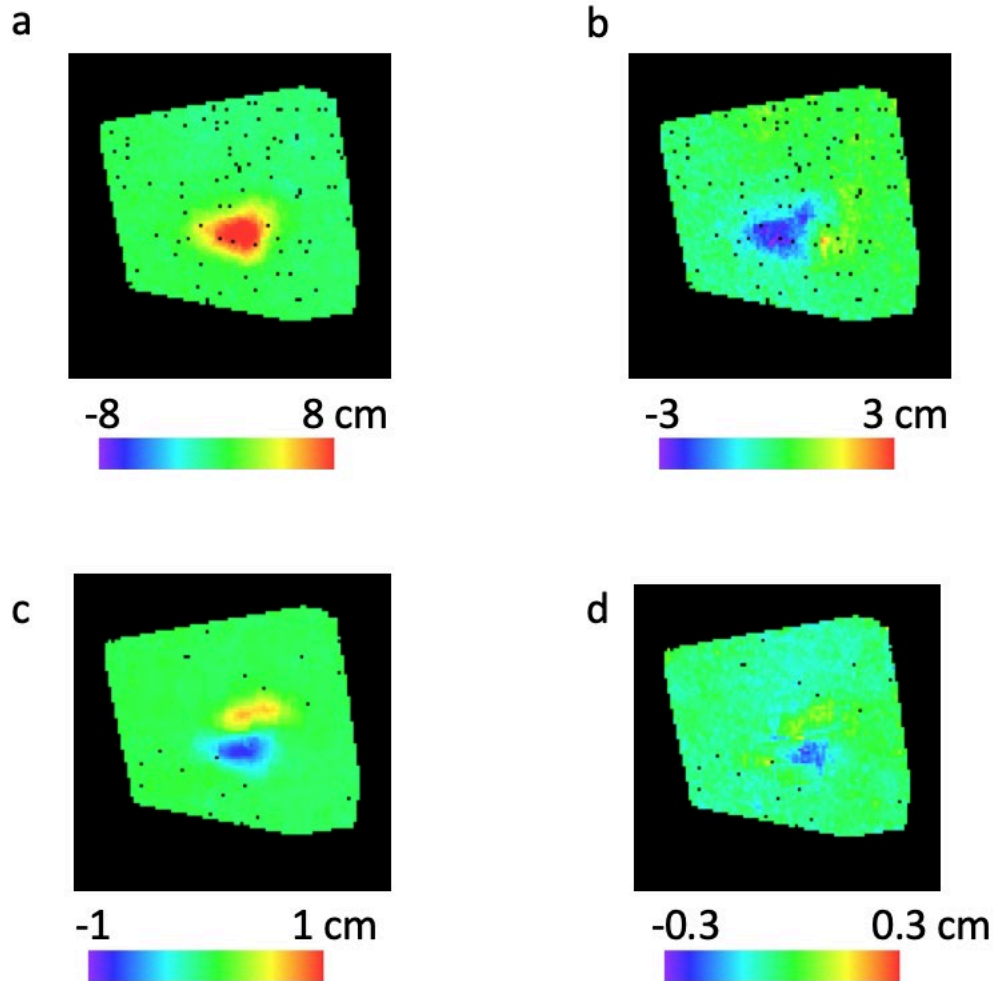


Figure 7.4 Cumulative ground deformation before and after the aseismic slip. (a) Vertical deformation from August 2018 to January 2020. (b) East-west deformation from August 2018 to January 2020. (c) Vertical deformation from January 2020 to March 2020. (d) East-west deformation from January 2020 to March 2020.

The best interferograms (coherent and containing most deformation information) in the descending and ascending tracks are jointly inverted for the fault parameters. The best-fit parameters are listed in Table 7.2.

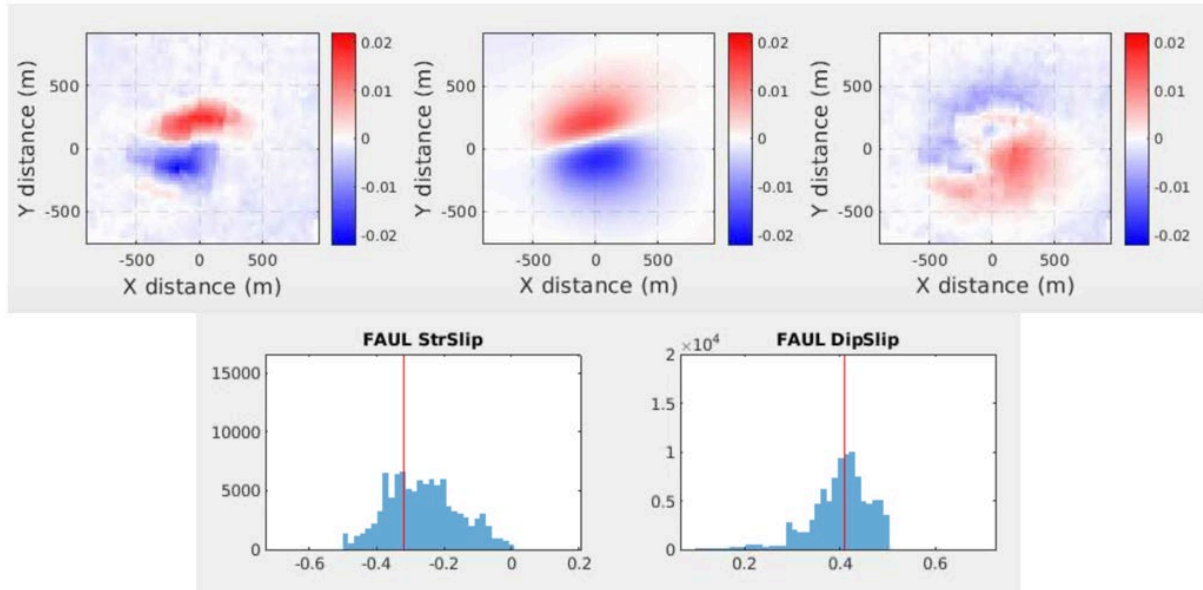


Figure 7.5 Bayesian inversion of the aseismic slip for descending track. Top: InSAR observation, simulation and the residual. Bottom: Posterior distribution of the strike and dip angle.

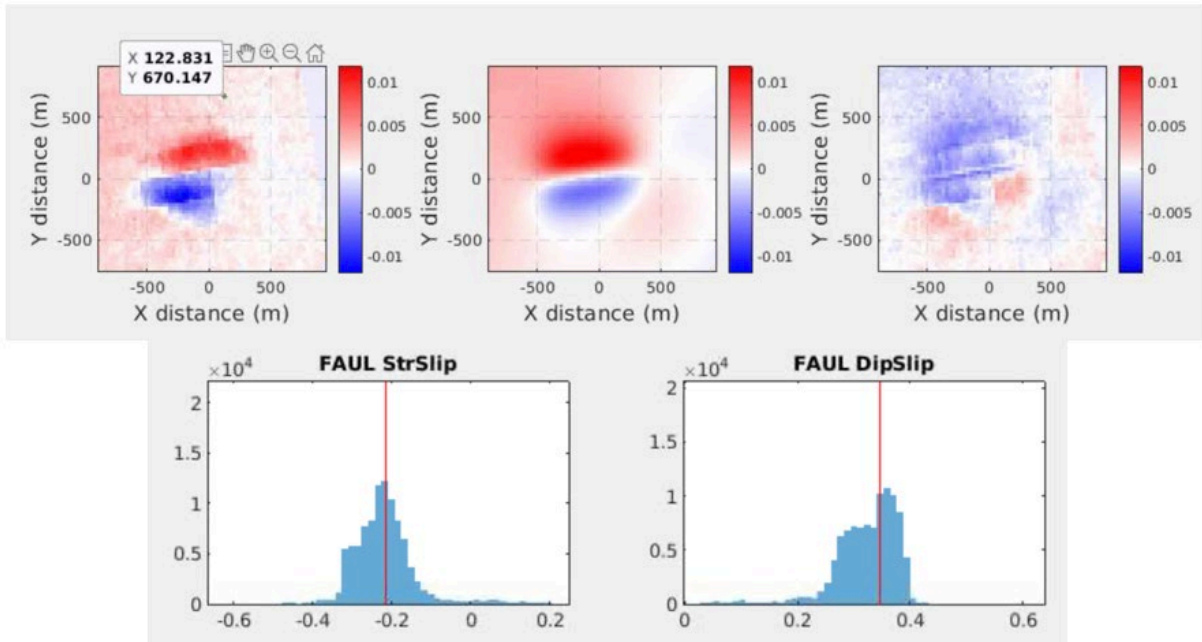


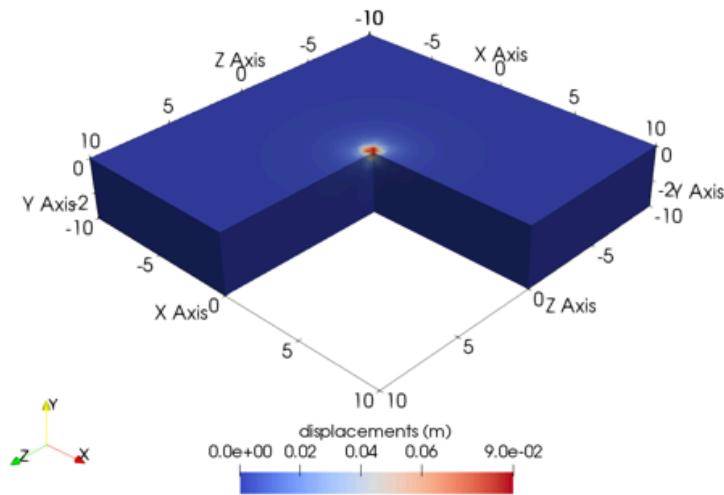
Figure 7.6 Bayesian inversion of the aseismic slip for ascending track. Top: InSAR observation, simulation and the residual. Bottom: Posterior distribution of the strike and dip angle.

Length (m)	639
Width (m)	63
Depth (m)	312
Strike (°)	260
Dip (°)	88

Table 7.2 Inferred fault parameters.

The simulation of ground deformation induced by wastewater injection in well #21935700 is plotted in Fig. 7.7. With the monthly injection volume data, to maintain the measured spatially localized deformation (diameter < 1 km), the injection depth should be adjusted to ~ 200 m, which suggests possible wastewater leakage. When the maximum vertical ground deformation reaches 8 cm (Fig. 7.7a), the corresponding pore pressure near the fault plane reaches 20 MPa, way larger than the reference criteria ~ 6 MPa (Dvory et al., 2022), initiating the aseismic slip.

a



b

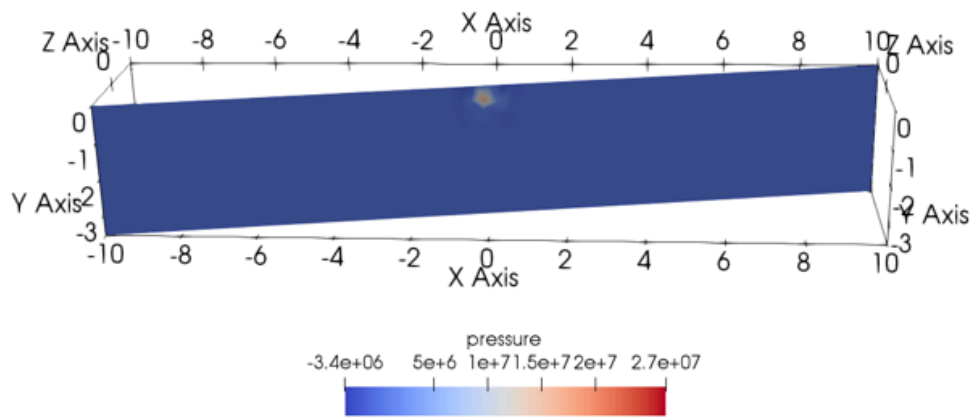


Figure 7.7 Simulation of deformation before the aseismic slip and the corresponding pore pressure distribution on the inferred fault plane.

The nearly vertical fault solved from the slip inversion and the large cumulative pore pressure suggest the crack could be induced by the injection. However, before the fault movement, the surface uplift only occurs in the southern side of the fault, which indicates the

fault is pre-existing and serves as a flow barrier during this period. Fluids injected under pressure initiate pore pressure diffusion, causing pore pressure to increase from the injection point outwards. As injection continues, the region influenced by elevated pore pressure expands through time. When the stress reaches the Coulomb failure criterion, the pre-existing fault reactivates and the aseismic slip starts. Another possible mechanism is that the pore pressure changes influence the nearby stress field and alter the fault-loading conditions. The aseismic slip is believed to be velocity-strengthening friction. After the completion of the injection, the aseismic slip lasts for a total of three months. Future work is to investigate the velocity-strengthening friction with rate-state friction law.

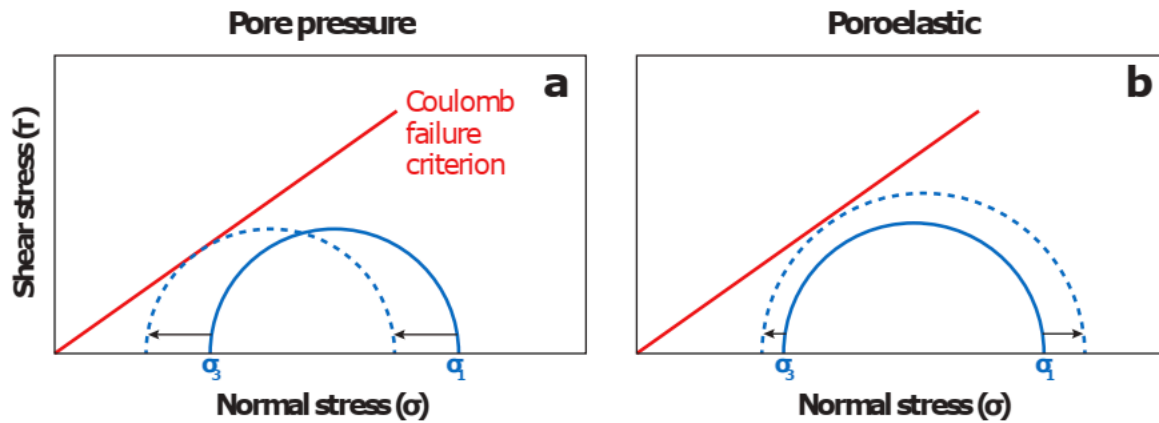


Figure 7.8 Conceptual illustrations of the possible mechanism (pore pressure increases and solid matrix stress changes).

Reference

- Ali, S. T., 2014, Defmod - Parallel multiphysics finite element code for modeling crustal deformation during the earthquake/rifting cycle. Preprint at <http://arxiv.org/abs/1402.0429>.
- Battaglia, M., Cervelli, P. F., & Murray, J. R., 2013. dMODELS: A MATLAB software package for modeling crustal deformation near active faults and volcanic centers. *Journal of Volcanology and Geothermal Research*, 254, 1-4.
- Cornet, F.H., 2016. Seismic and aseismic motions generated by fluid injections. *Geomechanics for Energy and the Environment*, 5, pp.42-54.
- Dvory, N. Z., & Zoback, M. D., 2021. Prior oil and gas production limits the occurrence of injection-induced seismicity in the Delaware Basin of West Texas and southeastern New Mexico. *Geology*, 49(10), 1198–1203.
- Dvory, N.Z., Yang, Y. and Dunham, E.M., 2022. Models of Injection-Induced Aseismic Slip on Height-Bounded Faults in the Delaware Basin Constrain Fault-Zone Pore Pressure Changes and Permeability. *Geophysical Research Letters*, 49(11), p.e2021GL097330.
- Eyre, T.S., Samsonov, S., Feng, W., Kao, H. and Eaton, D.W., 2022. InSAR data reveal that the largest hydraulic fracturing-induced earthquake in Canada, to date, is a slow-slip event. *Scientific reports*, 12(1), p.2043.
- Healy, J.H., Rubey, W.W., Griggs, D.T. and Raleigh, C.B., 1968. The denver earthquakes. *Science*, 161(3848), pp.1301-1310.
- Hennings, P.H., Snee, J.E.L., Osmond, J.L., DeShon, H.R., Dommissive, R., Horne, E., Lemons, C. and Zoback, M.D., 2019. Injection-induced seismicity and fault-slip potential in the Fort Worth Basin, Texas. *Bulletin of the Seismological Society of America*, 109(5), pp.1615-1634.
- Horne, E., Hennings, P., Smye, K., Calle, A., Huang, D. and Savvaidis, A., 2022, November. Structural characterization and rupture hazard assessment of faults in the Midland Basin, west Texas. In *SEG/AAPG International Meeting for Applied Geoscience & Energy. OnePetro*.
- Keranen, K.M. and Weingarten, M., 2018. Induced seismicity. *Annual Review of Earth and Planetary Sciences*, 46, pp.149-174.
- Lund Snee, J. E., & Zoback, M. D., 2018. State of stress in the Permian basin, Texas and New Mexico: Implications for induced seismicity. *The Leading Edge*, 37(2), 127–134.
- Okada, Y. Surface deformation due to shear and tensile faults in a half-space. *Bull. Seismol. Soc. Am.* 75, 1135–1154 (1985).

Samsonov, S. and d'Oreye, N., 2012, Multidimensional time-series analysis of ground deformation from multiple InSAR data sets applied to Virunga volcanic province, *Geophys. J. Int.*, 191, 1095–1108.

Yeo, I.W., Brown, M.R.M., Ge, S. and Lee, K.K., 2020. Causal mechanism of injection-induced earthquakes through the Mw 5.5 Pohang earthquake case study. *Nature communications*, 11(1), p.2614.

CHAPTER 8

Conclusion

Oil and gas industry related geohazards including surface deformation and induced seismicity pose risks to humanity and the stability of public facilities and result in financial loss and potential life loss. Besides, wastewater leakage during oil and gas activities can risk human health and freshwater aquifer system. The Permian Basin has been intensively developed for boosting hydrocarbon production. Wells and rigs for hydrocarbon production, oil/gas pipelines, and roads for transporting hydrocarbons have been built. The geohazards occurring in the prolific basin, unfortunately, have not been well known, although surface deformation can threaten the infrastructures and oil facilities.

In our study, InSAR has shown the capability to measure a localized surface displacement related to fluid injection/extraction. Comparison between the time-series InSAR deformation and information about the nearby injection or production records (e.g., well log, production/injection depth, injection volume rate) from state regulatory agencies is essential to evaluate whether the geohazards are oil and gas industry related or not. For the case in Reeves county, the surface uplift detected by InSAR near is induced by the wastewater disposal. The inverse elastic Mogi model performs well to roughly estimate the effective injection depth and volume from the measured InSAR deformation. The combination of InSAR results and poroelastic models gives a clue about the hydrologic properties of the strata. Results from both elastic and poroelastic models indicate that the effective injection depth is much shallower than

reported. The most reasonable explanation is that the well was experiencing leakage due to casing failures and/or sealing problem(s). The results suggest salinity change in the Rustler Aquifer during the injection active period though local groundwater quality measurement is not available. For the case in Winkler county, surface uplift and the follow-on recovery detected by InSAR from 2015 to 2020 can be attributed to nearby wastewater disposal. The Bayesian Monte Carlo approach with a forward poroelastic finite element modeling performs well to solve the ground deformation induced by fluid injection/extraction. The posterior distribution provides reasonable MAP estimates and uncertainties of hydro-geomechanical parameters and also reveals under-reported volumes in the well near the deformation center. Compared to other constraints, the Bayesian Monte Carlo approach with a forward poroelastic finite element modeling of InSAR-derived spatio-temporal data as constraint shows its advantages in solving poroelastic problems related to wastewater disposal. Finally, we have also investigated a case of aseismic slip related to oil and gas activities. The InSAR observation and poroelastic models provide estimates of fault parameters, slip information, and pore pressure field, which shed light on the possible mechanisms of the aseismic slip.

The three cases of this study prove that the combination of InSAR observation and poroelastic finite element models can gauge the effective depth and volume of wastewater injection and infer induced aseismic slip caused by oil and gas activity. Our analysis provides an indirect leakage monitoring technique to supplement current infrequent leakage detection methods, and a new tool to estimate local hydrogeologic properties which can serve as a reference for adjacent oil fields. Furthermore, our study provides a scientific basis for assisting wastewater disposal management and regulation.